MANIPULATION OF NANOCOMPOSITES INTERFACE FOR POLYMER PROPERTY ENHANCEMENTS

A Dissertation

by

CONG LIU

Submitted to the Office of Graduate and Professional Studies of
Texas A&M University
in partial fulfillment of the requirements for the degree of

DOCTOR OF PHILOSOPHY

Chair of Committee,	Hung-Jue Sue
Committee Members,	Hongcai Zhou
	Lei Fang
	Iman Borazjani
Head of Department,	Ibrahim Karaman

August 2020

Major Subject: Materials Science and Engineering

ABSTRACT

Nanoscale fillers blended with polymers ("nanocomposites") offer the real possibility of creating materials with properties that are not realizable with traditional, micron-scale fillers. In order to improve the performance of polymer nanocomposites, attempts have been undertaken to enhance the properties of both fillers and the polymer matrix. However, an important but hidden factor for developing high performance polymer nanocomposites is understanding and controlling the filler/matrix interfacial region. The overall objective of my dissertation is to develop new approaches to manipulate the interface of the nanocomposites, study the role of the interface in influencing mechanical behavior of polymer nanocomposites, and fabricate high performance and multi-functional polymer nanocomposites.

Our study first focuses on studying the role of the interfacial region on the fracture behavior of the polymer nanocomposites. A set of model systems based on polymethylmethacrylate (PMMA) matrix containing polymer brushes grafted on metal-organic-framework (MOF) nanoparticles were synthesized and investigated. By systematically adjusting the polymer brush length and graft density on MOF nanoparticles, the fracture behavior of PMMA/MOF nanocomposite is found to change from forming a few big crazes to massing crazing, and to significant shear banding, which results in significant improvement in fracture toughness. The implication of the present finding for the design of high performance, multi-functional polymer nanocomposites is discussed.

The nanoscale particles typically aggregate, which negates any benefits associated with the nanoscopic dimension. There is a critical need for establishing processing techniques that are effective on the nanoscale yet are applicable to macroscopic processing. A new strategy to prepare self-curing epoxy nanocomposites has been proposed. Epoxy can be cured by the nanoparticles without the addition of curing agents, by taking the advantages of the surface chemistry of the nanoparticles. Three types of self-curing epoxy nanocomposites containing MOF, MOF decorated carbon nanotubes, and zirconium phosphate are prepared to achieve multi-functional polymer nanocomposites. The simple process can be easily scaled up to produce nanocomposites.

DEDICATION

To my husband and parents

ACKNOWLEDGEMENTS

First and foremost, I would like to thank my advisor, Professor Hung-Jue Sue for the continuous support of my Ph.D study and research, for his patience, motivation, enthusiasm, and immense knowledge. Without him, this dissertation would not have been possible to complete. I would also like to thank my committee members, Dr. Hongcai Zhou, Dr. Lei Fang, and Dr. Iman Borazjani, for their time, interest, and helpful comments.

I truly appreciate my current and previous colleagues, Zewen Zhu, Qihui Chen, Fangqing Xia, Dr. Farhad Daneshvar, Dr. Tan Zhang, Dr. Spencer Hawkins, Dr. Fan Lei, Dr. Tatsuya Hirata and other workers for the precious discussion and the friendship.

Special thanks to Dr. Michael Mullins for his scientific advice and knowledge and many insightful discussions and suggestions.

Many thanks to Eddy Garcia-Meitin (The Dow Chemical Company) and Dr. Harold Ross Payne (College of Veterinary Medicine & Biomedical Sciences) for their delicate help in microtome sample preparation.

Thanks also go to all the staff for making my time at Texas A&M University a great experience. I want to thank Mr. Richard Littleton and Dr. Hansoo Kim at the Microscopy and Imaging Center (MIC) who helped me a great deal in TEM training. Thanks also go to Dr. Yordanos Bisrat for her help with SEM. I also want to thank Dr. Wilson Serem for his assistance on AFM and nanoindentation.

Finally, thanks to my mother and father for their encouragement and to my husband for his patience and love.

CONTRIBUTORS AND FUNDING SOURCES

Contributors

This work was supervised by a dissertation committee consisting of Professor Hung-Jue Sue [advisor and committee chair] of the Department of Materials Science and Engineering and Professor Hongcai Zhou and Professor Lei Fang of the Department of Chemistry and Professor Iman Borazjani of the Department of Mechanical Engineering.

The measurement of fracture toughness was conducted by Qihui Chen. All other work conducted for the dissertation was completed by the student independently.

Funding Sources

This work was partially supported by the research funding from KANEKA Corporation.

NOMENCLATURE

CNT	Carbon Nanotube
CSR	Core-shell Rubber
CTE	Coefficient of Thermal Expansion
DLS	Dynamic Light Scattering
DMA	Dynamic Mechanical Analysis
DETDA	Diethyl Toluene Diamine
DGEBA	Diglycidyl Ether of Bisphenol A
DGEBF	Diglycidyl Ether of Bisphenol F
DSC	Differential Scanning Calorimetry
DN-4PB	Double-Notch Four-Point-Bend
GD	Grafting Density
MOF	Metal-Organic Framework
MWCNT	Multi-walled Carbon Nanotube
OM	Optical Microscopy
PMMA	Poly(methyl methacrylate)
QA	Quaternary Ammonium
SEM	Scanning Electron Microscopy
SENT	Single Edge Notched Tension
TBA	Tetra-n-butylammonium
TEM	Transmission Electron Microscopy

TGA	Thermogravimetric Analysis
XRD	X-ray Diffraction
ZIF	Zeolitic Imidazolate Framework
ZrP	Zirconium Phosphate

TABLE OF CONTENTS

Page

LIST OF FIGURES

Page

LIST OF TABLES

Page

1. INTRODUCTION

1.1. Overview

Nanoscale fillers blended with polymers ("nanocomposites") provide significant promise in the development of advanced materials for various applications (Figure 1-1).[1] Polymer nanocomposites enable the design of materials with properties that cannot be realized with conventional fillers.[2] The nanofillers can have unusual properties from micron-scale fillers and act as small mechanical,[3] optical,[4] and electrical defects.[5] Another key factor for the unusual properties of polymer nanocomposites is that nanofillers produce a substantial quantity of interfacial polymer with distinctive characteristics from the bulk, providing an opportunity for multifunctionality(e.g., conductive fillers, toughening agents, transparent polymers).[6]

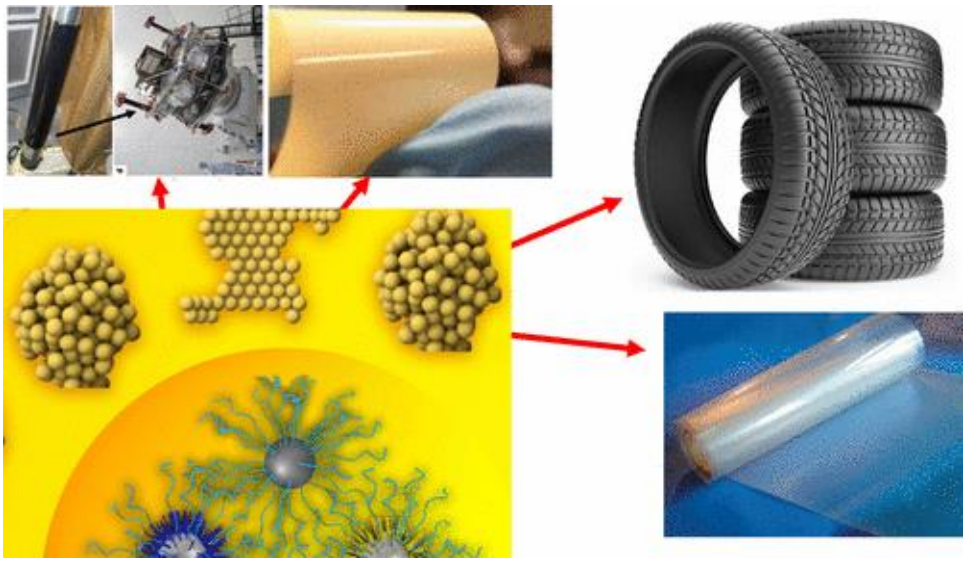

Figure 1-1. Various applications of polymer nanocomposites. Reprinted with permission from ref 2.

Understanding the 2D nanofiller/matrix interface and the resulting 3D interfacial volume that develops is the key point to controlling and optimizing the properties of polymer nanocomposites (Figure 1-2).[7] The 2D interactions are critical because the nanofiller/matrix interfacial interactions as the filler/matrix interactions determine the dispersion state of the filler particles and the amount of the interfacial volume.

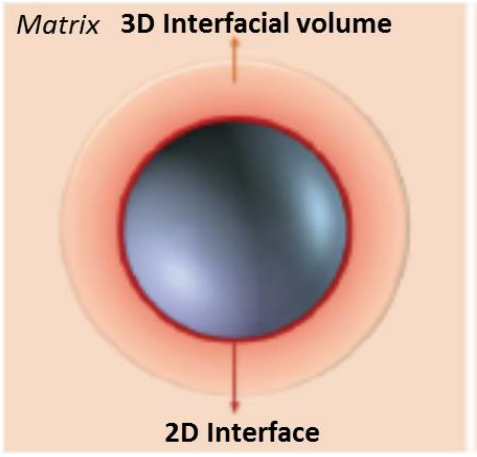

Figure 1-2. An illustration of a 2D nanofiller/matrix interface and the resulting 3D interfacial region. Reprinted with permission from ref 7.

The 3D interfacial region is a region with properties different from the bulk. Due to the large volume of the interfacial volume, this component may constitute a significant portion of the bulk. For instance (Figure 1-3), in a composite system containing 5 vol% 10 nm spherical nanoparticles, when the thickness of the interfacial volume is set to be 5 nm, the volume fraction of this interfacial volume can be as high as 35 vol%. With the increase of nanofiller loading, the interfacial region becomes an even more significant volume fraction of the polymer nanocomposite.

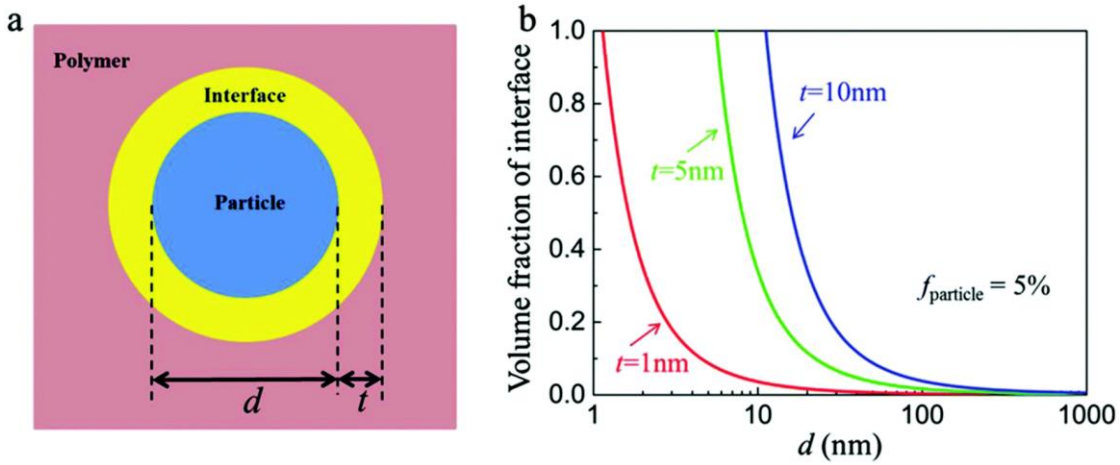

Figure 1-3. (a) Schematic illustration of the filler–polymer interface structure in nanocomposite consisting of a spherical nanoparticle. (b) Calculated variation of interface volume fraction with the diameter of nanoparticles possessing different interface thicknesses, the volume fraction of nanoparticles is fixed at 5%. Reprinted with permission from ref 8.

The 3D volume influences the overall properties of polymer nanocomposites mainly in two ways. First, the different chemistry or structure in the region can significantly alter the structure of the bulk, such as the crosslinking density, crystalline structure, or morphology of the bulk. Second, the increased or reduced mobility of the molecules in the interfacial region can dramatically affect the properties of the bulk, especially the mechanical and dielectric properties. Therefore, to develop high-performance polymer nanocomposites, it is essential to consider the interfacial region induced by the nanofillers. However, we haven't fully understood how to control the structure and properties of the interfacial volume, which impedes the development of polymer nanocomposites in high-end applications. Besides the absence of understanding the structure-property relationships, the lack of cost-effective techniques for regulating the

dispersion of the nanoparticles in polymer matrices is one of the greatest challenges of the large-scale processing and commercialization of nanocomposites. The nanoparticles usually aggregate, negating all advantages correlated with their nanoscopic size.[9] Therefore, the suitable interfacial design is needed to control the dispersity of the fillers and modulate the interface between the fillers and the polymer matrix.

Metal–organic framework (MOF) particles are a relatively new family of nanoporous materials[10], composed by metal ion or metal clusters and organic linkers, exhibiting an ordered, well-defined porous structure (Figure 1-4).[11,12] Due to the high porosity, tunability, and attractive properties of MOFs, polymer nanocomposites containing MOFs have attracted great attention. MOFs generally have excellent compatibility with organic polymer matrix compared to other nanofillers, such as silica, alumina, and carbon black, as the organic linkers can interact with polymers through molecular design. Besides, the controllable and versatile chemistry of MOF can help to manipulate the interface of polymer nanocomposites. Due to the well-defined crystalline structure and chemical tunability, polymer/MOF nanocomposites are good candidates as model systems to study structure-property relationships. Traditional applications of polymer/MOF composite materials are focused on gas storage and separation, which take advantage of the inherent porosity and high surface area of MOF and flexibility of polymer materials. Among possible applications, my doctoral research also pay attention to their potential as low-k dielectrics.

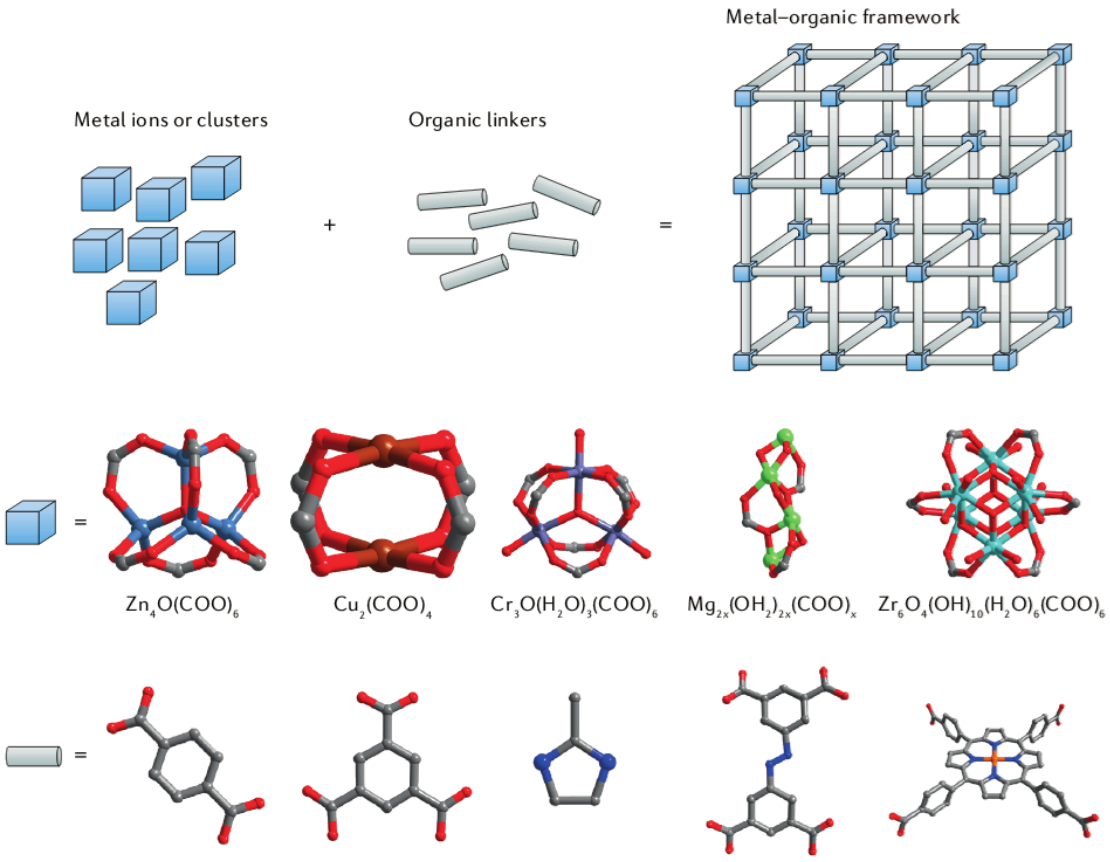

Figure 1-4. Composition of MOFs materials. Reprinted with permission from ref 12.

Overall, it is imperative to have a fundamental understanding of structure-property–function relationships in polymer nanocomposites and to design materials with optimal properties by manipulating the interface between the nanofillers and the polymer matrix. The objective of this dissertation is to fundamentally investigate the structure-property relationship of polymer nanocomposites through manipulating the interfaces.

The goals of the research are as follows: (1) Gain a fundamental understanding of the role of the interface in modifying the mechanical properties of the polymer nanocomposites. Because this area of research is extremely broad, the dissertation is

focused on the case of fracture behavior of polymer nanocomposites. In order to systematically study the interface effects, a set of model systems by manipulating the nanoparticle surface characteristics is designed; (2) Develop new strategies in preparation of multi-functional polymer nanocomposites. In order to achieve the optimal properties, the dispersion of the nanofillers are well controlled by modify the nanoparticle functionalities. The mechanical and dielectric properties of these polymer nanocomposites are studied.

1.2. Organization of the dissertation

A comprehensive literature review on the recent progress of the interfacial design of polymer nanocomposites will be given as Section 2. Detailed information regarding the polymer brushes modification and interface properties is described. It also provides a brief review of the effect of the interface on the mechanical and dielectric properties.

Section 3 describes a fundamental study of the interface effects on the fracture behavior of the polymer nanocomposites. A set of model systems based on polymethylmethacrylate matrix containing polymer brushes grafted on MOF nanoparticles are synthesized. It is found that different polymer brush characteristics may lead to distinctly different toughening mechanisms from a few big crazes to massive crazing, and to nanoparticle voiding and matrix shear banding.

A facile way to fabricate multi-functionalized epoxy nanocomposites containing exfoliated α-zirconium phosphate (α-ZrP) is covered by Section 4. The multi-functionalities of the modified α-ZrP as reinforcing agent and curing agent are discussed. The incorporation of the modified α-ZrP nanoplatelets can greatly improve the Young's

modulus due to the strong covalent bonding between the nanoplatelets and the epoxy matrix. The usefulness of the present study for preparation of high-performance thermosetting polymer is discussed.

In Section 5, MOF is utilized as a modifier to lower dielectric constant and improve the mechanical properties of an epoxy matrix. The implication of the present study for utilization of MOF to improve the physical and mechanical properties of polymeric matrices is discussed.

A new strategy using MOF as a modifier to decorate multi-walled carbon nanotubes (MWCNTs) to achieve high-k polymer nanocomposite is introduced in Section 6. The MOF decorated MWCNTs serve both as a curing agent and as a nanofiller to enhance dielectric, thermal, and mechanical properties of epoxy. It is found that the dielectric and mechanical properties of epoxy/MWCNT-ZIF-8 can be altered by changing their morphology at the interface.

Lastly, the concluding remarks to summarize the findings of this dissertation and the future research plans are drawn in Section 7.

2. LITERATURE REVIEW

2.1. Polymer nanocomposites interfaces/interphases

In order to maximize the volume fraction of the interfacial area, the dispersity of the nanoparticles needs to be well controlled.[13,14] However, It has been well known that even in the case of no attraction or repulsion exists between the polymer matrix and nanoparticles, the entropically driven depletion forces may encourage the agglomeration or aggregation of nanoparticles.[15] Attaching surface ligands to the nanoparticles is an effective strategy to alter the interfacial interactions.[16-18] Generally, the surface ligands can be classified into short molecules or polymer brushes. Short molecules mainly influence the enthalpic interactions with the matrix[6] and therefore improve the compatibility.[19] For instance, short ligands can repel, attract, or bond with matrix chains, and modify matrix chain mobility.[20] Polymer brush ligands complicate the thermodynamic interaction between the filler and matrix through introducing a large entropic component. Besides controlling the dispersity of the nanoparticles, the long polymer brushes also influence the mobility of the polymer chains in the vicinity of nanoparticle surface as well as the stress transfer ability from the matrix to the nanoparticle. Moreover, the introduction of polar molecules can manipulate the dielectric properties of the polymer nanocomposites.[21-23] General methods for the interfacial design of polymer dielectric nanocomposites are illustrated in Figure 2-1.

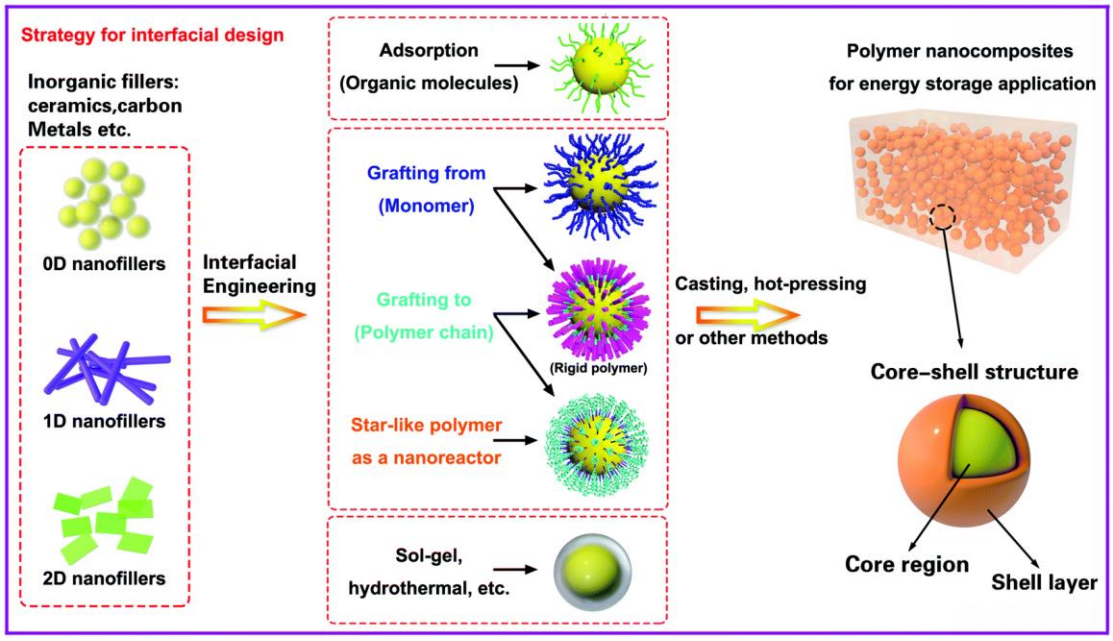

Figure 2-1. General methods associated with the design and control the interface of core–shell structured fillers for polymer nanocomposites. The left column shows the range of filler types, the central column indicates the core–shell interfacial control methods and the right column shows the final nanocomposite structure. Reprinted from ref 24.

2.2. Polymer brushes

A polymer brush can be attached to a nanoparticle through "grafting to" or "grafting from" strategies. The advantage of "grafting to" is that well-defined polymer brushes can be directly functionalized.[25,26] The synthesis procedure for this method is about attaching a functionalized polymer brushes through some suitable organic reactions (Figure 2-2).[27] However, the disadvantage of this method is the exitance of steric repulsion between the diffusing chain and already attached polymer chains may result in a low graft density.[28] On the other hand, the "grafting from" method provides much higher graft density. The surface of the nanoparticles is modified by suitable chain transfer agents or initiators, and then the polymer brushes are polymerized from the surface of nanoparticles

through surface-inititiated atom transfer radical polymerization (ATRP), nitroxide-mediated polymerization (NMP), or reversible-addition fragmentation chain transfer (RAFT). For instance, Hojjati and colleagues have modified the surface of titania (TiO_2) nanoparticles by carboxylic acid functionalized initiator agents.[29,30] Subsequently, poly(acrylic acid) (PAA) and poly(methyl methacrylate) (PMMA) were successfully grafted into the surface of the nanoparticles, obtaining well dispersed TiO_2 nanocomposites.

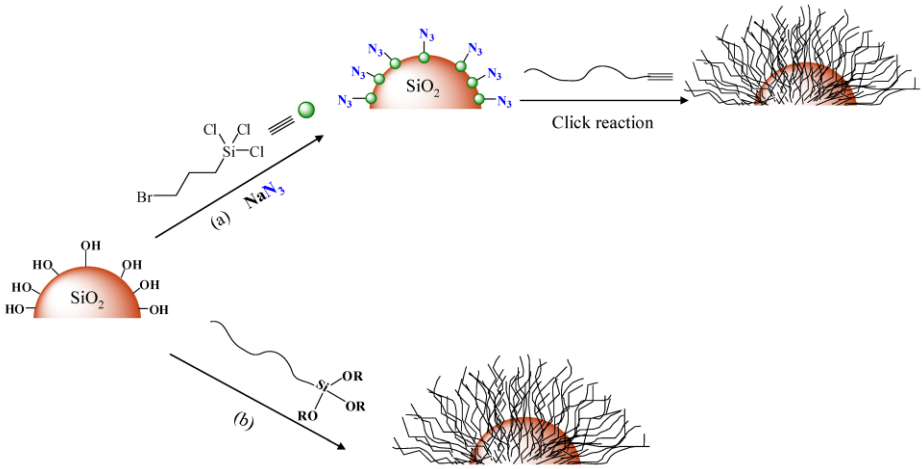

Figure 2-2. Schematic representation of the synthesis procedure for the grafting of polymer chains onto the surface of silica particles. Reprinted from ref 27.

2.3. Interface structure

The properties of the polymer nanocomposites are greatly influenced by the large amount of interfacial region. The segregation of molecules has a different impact on thermoplastics vs. thermosets systems. For instance, the crosslink density of thermosets can be affected by the existence of the nanoparticles.[31,32] It has been found that the

interfacial region induced by the nanoparticles may interrupt the crosslinked network, consequently reduces the crosslink density.[33] While in some cases, the nanofillers may act catalysts and increases the cross-link density and alter the curing kinetics of the thermosets.[34] Moreover, the cross-link density of polymer nanocomposites is heterogeneous. Numerous reports have established that the crosslinking density of interfacial volume is different from the bulk polymer matrix.[33,35]

For amorphous polymers containing polymer brush grafted nanoparticles, depending on brush length and the graft density, the structure of the interfacial region can be altered as the polymer matrix can be penetrated or repelled from the polymer brushes.[36] There is a general agreement that when the nanoparticle and polymer are enthalpically attracted to one another, the density of polymer around the nanoparticles is higher than the bulk. Both experimental and computational results have demonstrated a change in mobility near the surface of the spherical nanofillers.[37-40] The difference in the mobility of polymer chains was firstly observed in the ultra-thin films, where the glass transition temperature(T_g) are changed about 40K in the free and supported films. This phenomenon is contributed to the interactions between polymer chains and the substrate.[41] For the cases of nanocomposites, this is a disputed topic in the literature, especially when it relates to the changes in T_g.[42] However, it is generally accepted that due to the addition of nanofillers, there are changes in local polymer mobility under specific scenarios.

Torkelson and coworkers have found that the rate of structural relaxation of the interfacial polymer can be detectably altered for tens of nanometers away from the particle/substrate interface using a fluorescent technique to probe the changes in the

dynamics in small molecule and brush grafted nanoparticle composites and found.[39,43,44] Broadband dielectric spectroscopy and AFM have also been used to investigate the interface mobility.[45,46] For a composite system with nanoparticle/polymer attractive interactions, Sokolov has used broadband dielectric spectroscopy to exhibit a decrease of the relaxation times by 2 orders of magnitude in the interfacial region.[47] Scotti and coworkers have used AFM to demonstrate that in a rubber nanocomposite system containing silica particles, a rubber layer is immobilized at the particle surface.[46]

2.4. Functional properties arising from incorporation of nanoparticles

A list of functional properties of major interest to this dissertation is discussed in this section.

2.4.1. Thermomechanical properties

The mechanical response of polymers is strain rate dependent and shows viscoelastic behavior, which is determined by the chain mobility relaxations. Therefore, the characterization of the thermomechanical behavior of polymer nanocomposites provides an opportunity to study the effects of the interface on the mobility and relaxation dynamics. As the characteristic relaxation time of polymer molecules decreases with increasing temperature, the storage and loss modulus are also functions of temperature. Most polymer materials display a transition from glassy state to rubbery state. This transition takes place over a temperature range known as glass transition temperature (T_g). T_g is also signified by an abrupt change in thermal expansion coefficient (CTE) and heat capacity. Therefore, any technique that probes any of these parameters can be utilized to study the glass transition behavior and mobility of polymeric materials. For example,

dilatometry and differential scanning calorimetry (DSC) can be used to investigate the CTE and heat capacity. When measuring the T_g, we need to notice that the measured values may change from technique to technique, as well as even on the same instrument. Many factors need to paid attention to, such as heating and cooling rates.[48]

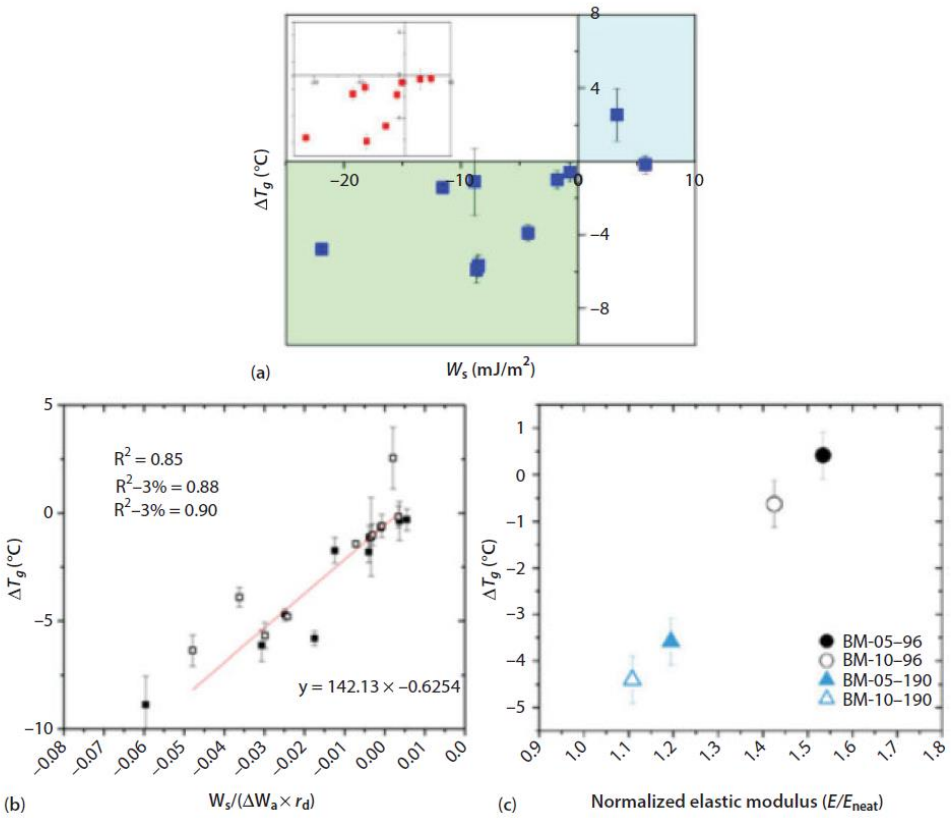

Figure 2-3. Plots correlating T_g changes with (a) the work of spreading (W_s) and (b) surface energetic parameter $Ws/(\Delta W_a \times r_d)$ and (c) bulk elastic modulus in silica filled polymer composites. The legend in (c) refers to various combinations of graft densities and matrix molecular weights used to realize the variations in T_g. In the legend BM refers to bimodal brushes, 05 and 10 refer to the long brush graft densities of 0.05 and 0.10 chains/nm^2, respectively and 96 and 190 refer to matrix molecular weights of 96 and 190 kg/mol. Reprinted with permission from ref 7.

For the cases of polymer nanocomposites, T_g may be greatly changed due to the presence of a large amount of interfacial region. The changes in the relaxation behavior of the interfacial region are determined by the polymer matrix and filler interactions. When polymer chains in the matrix strongly interact with the modified fillers through chemical interactions or entanglement, T_g tends to increase. In addition, it has been found that the entanglement of polymer brushes grafted on the fillers with the polymer host can reinforce the stress transfer from matrix to the fillers, leading to an increase in storage modulus. On the other hand, when this interaction is weak or unfavorable, a reduced glass transition may be observed as the interfacial region behaves as a plasticizer. Figure 2-3 reveals the influence of short-chain modification of fillers on the interaction energy (W_s) and T_g.

2.4.2. Fracture behavior of polymer nanocomposites

There has been considerable interest in using nanofillers to enhance the mechanical properties of various polymeric materials for decades.[3,32,49-60] A polymer nanocomposite consists of a polymer or copolymer having nanoparticles or nanofillers dispersed in the polymer matrix. The fillers can be categorized into isotropic and anisotropic nanomaterials. They may be of different shapes but at least have one dimension of less than 100 nm. Polymer nanocomposites offer significant potential in the development of advanced materials for many applications, such as in the automobile industry. The broad scientific community was galvanized by nanocomposites in the early 1990s, Toyota researchers revealed that adding mica to nylon produced a five-fold increase in the yield and tensile strength of the material.[61,62] Subsequent developments have further contributed to the surging interest in polymer nanocomposites. Rubber toughening is a well-known

strategy to improve the fracture toughness of brittle polymers.[54-58] In rubber-toughened epoxies, Yee and Pearson[63] showed that triaxial stresses could induce cavitation of rubber particles, which transforms the triaxial stress state to biaxial stress state around the rubber particles to promote shear banding in the polymer matrix. In high impact polystyrene, dispersed rubber particles can initiate, stabilize, and terminate crazes, leading to the massive formation of crazes to increase the fracture toughness of polystyrene.[64] However, the addition of rubber usually compromises the Young's modulus and thermal stability of the polymer nanocomposites.[59,60]

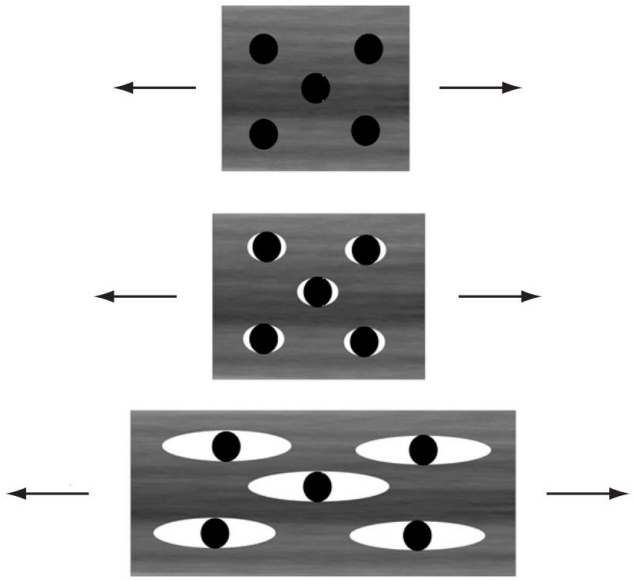

Figure 2-4. Toughening mechanism with rigid particles. Reprinted from ref 65.

Rigid reinforcing agents can effectively improve the stiffness of polymer matrix, but is often accompanied by a decrease of ductility.[66-68] However, it has also been shown

that an addition of a small amount of nanoparticle may lead to drastic improvements in the ductility of the host polymer, which challenges the existing theories.[69] The main mechanism of toughening polymers with the addition of inorganic fillers has been extensively discussed and involves stress concentration, debonding of the polymer/filler interface and the formation of shear bands (Figure 2-4).

Polymer brushes grafted nanoparticles have been found to show an extraordinary performance in improving the fracture toughness without compromising the stiffness of the materials.[70-72] Gao found a copolymer grafted SiO_2 nanoparticles enhanced the fracture toughness (maximum 300% improvement) of the epoxy matrix induced by void growth and shear banding.[70] However, the copolymer contains a functional group that can react with epoxy resins, which may affect the crosslinking network of the epoxy matrix. The fracture behavior is very sensitive to the structure of the polymer matrix, which strongly affects cracks initiation and propagation. Therefore, it is hard to elucidate the role of the interface on the fracture behavior based on their system. Giovino observed the toughness of PS-grafted SiO_2 toughened PS nanocomposites was twice as large as the neat polymer, due to particle debonding followed by plastic void growth.[73] A bimodal population of polymer brushes assures good dispersion of nanofillers while increasing the complexity of the interfacial region. Hence, it remains hard to conclude the effect of interface on the fracture behavior. Despite some good examples of using grafted nanoparticles as effective toughening agents, there is still a lack of systematic study about the effects of interface on the fracture behavior of polymer nanocomposites, especially based on thermoplastics.

2.4.3. Dielectric properties of polymer nanocomposites

The dielectric constant, *k*, is a physical feature related to the electric polarizability of a material.[74] The dielectric materials are categorized into high-*k* dielectrics ($k > 3.9$) and low-*k* dielectrics ($k < 3.9$), in comparison to the *k* value of silicon dioxide, which is 3.9. Besides *k*, *k* loss is also an important parameter, which is raised from the motion of bound charges in response to an applied electrical field. Recently, there is a fast-growing interest in both high-*k* and low-*k* dielectric materials due to their wide applications in the electronic and electrical industry. For example, high *k* dielectrics can serve as effective materials for cable insulation,[75] charge-storage capacitors,[76,77] electrocaloric cooling,[78,79] and artificial muscles.[80,81] While low-*k* materials are the key insulating components for isolating signal-carrying conductors from one another as well as reducing the signal propagation delay and dynamic power dissipation in the high-density and high-speed microelectronic packaging.[82]

Polymeric materials play a vital role in electronic packages as a result of their ease of processing, low cost, low dielectric constant, good adhesive properties, etc. The properties of polymers can be easily improved or altered by the incorporation of nanofillers into the polymer matrix. However, the biggest challenge in the fabrication of these nanocomposites is the low compatibility between the organic and inorganic components, which can result in agglomeration of nanofiller particles and a significant compromise in device performance.[9]

High dielectric constant (high-k) oxides and high-k polymer nanocomposites have been extensively studied and evaluated because of their promising applications in

electronics.[83-85] Some potential fields of application include organic field-effect transistor,[86,87] invertors,[88] electro-optics,[89] sensors,[90] and energy storage devices.[91,92] Dielectric polymer nanocomposites are generally composed of a dielectric polymer as the matrix and nanoscale inorganic/organic fillers for enhancement.[75,93] Polymers have been demonstrated to exhibit high breakdown strengths along with easy processing, while the nanofillers are usually composed of high-k ceramic or conductive nanoparticles.[94,95] The combination of both usually provide superior dielectric properties.[96]

Conventional high-k polymer nanocomposites use ceramic materials as fillers.[97] These ceramic-based materials possess excellent dielectric permittivity and low dielectric loss, as well as excellent thermal stability.[98] However, high loadings of the ceramic fillers would usually be needed to achieve permittivity greater than 30, making it difficult for processing and resulting in poor mechanical properties.[99] An alternative strategy is to incorporate conductive fillers to the polymer matrix to prepare percolative insulator/conductor polymer nanocomposites, which can have high permittivity when the content of the conductive filler is slightly below its percolation threshold.[100,101] For polymer composites containing conductive fillers, the polarization characteristics of the matrix molecule, conductive filler, and their interface collectively play a pivotal role in the dielectric properties.[102,103] According to the percolation theory[104] and the Maxwell−Wagner-Sillars (MWS) interfacial polarization effect,[96] the charge carriers in the composites would transport from the polymer matrix to the conductive fillers, resulting in the accumulation of space charge polarization at their interface. Among the conductive fillers, MWCNT is often used to prepare high-k polymer nanocomposites due to their

excellent electrical properties and high aspect ratio, which reduces the concentration needed to reach the desired percolation threshold.[105] The MWCNT-based polymers can possess a high dielectric constant at low MWCNT loadings.[106,107] However, the insulator/conductor pairs often lead to high dielectric loss as a result of high leakage currents due to possible direct contact between conductive fillers in the polymer matrix near the percolation threshold, which hinders their commercial applications.[108]

In order to address the aforementioned drawbacks, a core-shell structure (Figure 2-5) has been proposed and prepared by coating CNT with a layer of insulating polymer.[109,110] MWCNT coated with phosphaphenanthrene [111] or multi-branched polyaniline [112] has been utilized as fillers in high-k polymer nanocomposites. The nanocomposites with core−shell hybridized CNTs not only exhibit high-k but also maintain relatively low dielectric loss, suggesting such a strategy is a promising approach to prepare high-k nanocomposites.[113] However, surface modification of CNTs with low molecular weight surfactants or polymers usually leads to an adverse effect on glass transition temperature (T_g) and coefficient of thermal expansion (CTE) of the hosting polymer, making it undesirable for microelectronic applications.[101,114] To overcome the disadvantages of organic coatings on MWCNT, inorganic materials, such as SiO_2,[115] CuO,[116] and TiO_2,[117] were used to modify the MWCNT surfaces to maintain the physical and mechanical properties of the hosting matrix. However, the poor dispersion of the inorganic particle-coated CNTs in their polymer matrices limited their effectiveness for property improvement.

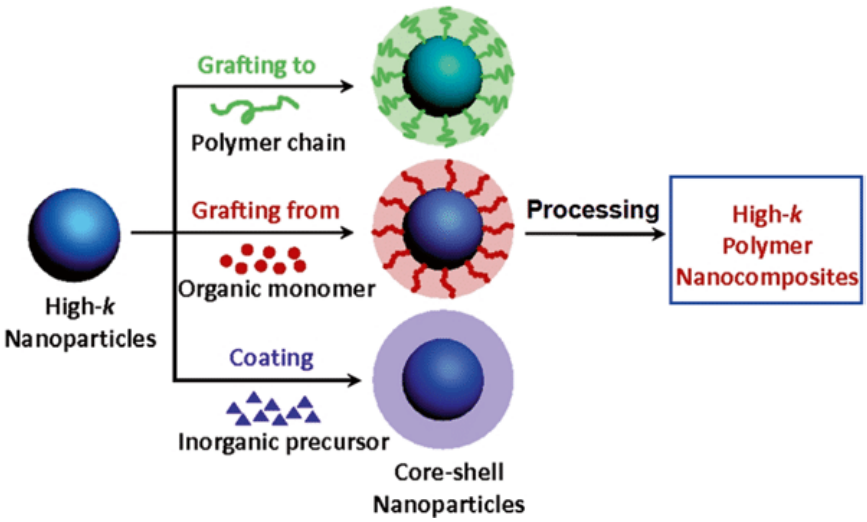

Figure 2-5. Approaches used to prepare core–shell nanoparticles for high-k polymer nanocomposites. Reprinted with permission from ref 75.

3. MANIPULATION OF FRACTURE BEHAVIOR OF POLYMETHYLMETHACRYLATE NANOCOMPOSITES BY INTERFACIAL DESIGN OF METAL-ORGANIC-FRAMEWORK NANOPARTICLES*

3.1. Introduction

Over the past few decades, there have been considerable efforts in improving the mechanical properties of polymeric materials for engineering applications.[3,32,49,50,52-57,59,60,118] Improvement of fracture toughness without causing a reduction in modulus and glass transition temperature (T_g) is among the most sought after goals. Rubber toughening is a well-known strategy to improve the fracture toughness of brittle polymers.[54-57] In rubber-toughened epoxies, Yee and Pearson show that triaxial stresses can induce cavitation of rubber particles, which transforms the triaxial stress state to biaxial stress state around the rubber particles to promote shear banding in the polymer matrix. In high impact polystyrene, dispersed rubber particles can initiate, stabilize, and terminate crazes, leading to massive formation of crazes to increase the fracture toughness of polystyrene.[64] Pearson and Yee also noted an increase in the fracture toughness of rubber-modified epoxies with decreasing rubber particle size,[63] indicating the effectiveness of small particle sizes in improving fracture toughness. However, the addition of rubber usually reduces the Young's modulus and thermal stability of the polymer matrix.[59,60]

* Adapted with permission from "Manipulation of Fracture Behavior of Polymethylmethacrylate Nanocomposites by Interfacial Design of Metal-Organic-Framework Nanoparticle Toughener" by Liu, C., Feng, S., Chen, Q., Zhu, Z., Noh, K., Kotaki, M., & Sue, H. J., submitted for publication. Unpublished work copyright by 2020 American Chemical Society.

Rigid reinforcing agents can effectively improve the stiffness of polymer matrix, but is often accompanied by a decrease of ductility.[66-68] However, it has also been shown that an addition of a small amount of nanoparticle may lead to drastic improvements in strength and stiffness, and without compromising ductility of the hosting polymer.[3,119,120] Some of the mechanical properties improvement in polymer nanocomposites reported in literature challenges the existing theories,[69] which may partially be due to an inadequate knowledge about the influences of the vast interfacial region between the nanoparticles and polymer matrix on mechanical behavior. The polymer chain dynamics near the nanoparticle interfacial region may be greatly altered due to their intimate contact with the nanoparticles, resulting in either restricted or enhanced mobility.[121-123] The delicate tailoring of the polymer−nanoparticle interface may enable the possibility of altering the properties of the entire polymer matrix. Experimental and modeling efforts have demonstrated that the tensile properties of polymer nanocomposites can be optimized by tailoring the interfacial characteristics at the polymer−nanoparticle interface.[70,73]

Another critical parameter in controlling the mechanical properties of polymer nanocomposites is the dispersion of nanoparticles because agglomerates of the nanoparticles may act as defects to initiate cracks to cause premature brittle failure. Since these high surface area nanoparticles are difficult to disperse well in polymer matrices, they are usually modified with surfactants to lower their surface energy and achieve good dispersion.[124-126] Other methods to alter the surface properties of the nanoparticles include radiation grafting, chemical vapor deposition, and a host of complicated synthesis procedures.[127-129]

Surface functionalization on nanoparticles may not only improve their dispersion but also alter the interfacial characteristics between the nanoparticles and polymer matrix, especially when polymer brushes are introduced on the nanoparticle surface.[130] Maillard showed that ductility could be substantially increased in glassy nanocomposite films composed of spherical silica nanoparticles grafted with polystyrene (PS) chains in PS matrix, while maintaining gains in elastic modulus and tensile strength.[72] The influence of the interfacial adhesion on rubber toughening has been studied by Liu et al. using rubber-modified PVA. They investigated three types of blends having three different levels of interfacial adhesion. The blends exhibiting a weaker interfacial adhesion showed debonding at the interface upon impact, which then induces shear yielding of the matrix. However, the blend with a stronger interface showed no microvoid formation, thereby shear yielding was suppressed. Similar phenomena have also been observed in Al_2O_3 toughened PMMA systems, where a "weak" interface leads to debonding, followed by void growth and plastic deformation. On the other hand, in some cases, a strong adhesive interaction can also achieve fracture toughness improvements.[131-133] Crosby and co-workers[132] found in polystyrene (PS)–grafted CdSe nanoparticle reinforced PS could achieve 100% increase in ductility. Gao found that copolymer-grafted SiO_2 nanoparticles enhanced the fracture toughness by 300% by void growth and shear banding mechanisms.[70] Giovino observed that the fracture toughness of a PS-grafted SiO_2 in PS was twice that of the neat PS due to particle debonding followed by plastic void growth.[73] Despite good examples of using polymer-grafted nanoparticles as effective toughening agents shown in literature, there is still a lack of systematic study on how the grafting

characteristics of polymer brushes on nanoparticles influences the fracture behavior of polymer nanocomposites.

The present study focuses on investigating how the fracture behavior of polymethylmethacrylate (PMMA) may be manipulated by incorporation of metal-organic-framework (MOF) nanoparticles, which were systematically surface-modified by polymer brushes having different brush lengths and graft densities to achieve different levels of adhesion and interaction with the PMMA matrix. Zeolitic imidazolate framework-8(ZIF-8) MOF nanoparticles, which possesses a nearly uniform particle size of 50 nm, were chosen as the model system because of the versatility in controlling its structure and surface chemistry through its organic linkers.[10,11] The double notch-four-point bend (DN-4PB)[134,135] method was employed to generate a sub-critically crack growth for fracture mechanisms investigation. The role of nanoparticle grafted polymer brush length and graft density on fracture behavior of PMMA is determined. Significance of the present study on manipulation of polymer nanocomposite fracture behavior through interfacial design is discussed.

3.2. Experimental section

3.2.1. Materials

Zinc nitrate hexahydrate ($Zn(NO3)_2 \cdot 6H_2O$), 1,2-dimethylimidazole, and octyl/decyl glycidyl ether were purchased from Sigma Aldrich. 2-methylimidazole was purchased from Alfa Aesar. Polymethyl methacrylate was kindly provided by Arkema Inc. Methanol (MeOH), 1-butanol (BuOH), and *N*,*N*-dimethylformamide (DMF) were purchased from VWR Chemicals and used as received.

3.2.2. Synthesis of ZIF-8

The ZIF-8 nanocrystals were synthesized following our previous work.[136] A solution of 3 g (10 mmol) of $Zn(NO_3)_2 \cdot 6H_2O$ in 100 mL of methanol and another solution of 6.6 g (80 mmol) of 2-methylimidazole in 100 mL of methanol were mixed and stirred for 1 h at room temperature. The resulting ZIF-8 nanocrystals were separated by centrifugation, followed by washing with methanol three times and finally redispersed as colloids in fresh methanol for further modification.

3.2.3. Synthesis of ZIF-8-DMI

ZIF-8 (2.28 g, 10 mmol) was dispersed in 40 mL of 1-BuOH via the solvent exchange of ZIF-8 solution from MeOH to 1-BuOH. The ZIF-8 solution and the 1,2-dimethylimidazole (DMI) mixture (1.92 g, 20 mmol) were added to a 100 mL round bottom flask. The combined suspension was sonicated for 5 min in an ultrasonic bath, then stirred at100 °C for 4 h. After cooling to room temperature, the particles were collected by centrifugation (fixed-angle rotor, 9000 rpm, 10 min), washed with 3×40 mL portions of MeOH, and soaked in MeOH for 24 h. The degree of ligand exchange was verified by NMR to be about 60%. The ZIF-8-DMI nanoparticles were chosen to prepare low graft density polymer brushes on ZIF-8.

3.2.4. Synthesis of polymer brushes grafted ZIF-8 nanoparticles

The ZIF-8 nanohybrids consisting of ZIF-8 core and polymer brushes were prepared *via* a one-step process. ZIF-8 (100 mg) suspension (20 mg/ml in MeOH) was mixed with 3.6 mL of an unknown mixture of octyl- and decyl-glycidyl-ether (polyalkylglycidylether) in a 25 mL round bottom flask, followed by ultrasonication for 30 min. Then, methanol

was removed using a rotary evaporator at 40 °C. The flask was then sealed with a rubber plug and degassed by N_2 purging. Afterward, the reaction was kept at 140 °C for various time periods. The nanoparticles were collected by centrifugation. The obtained polyalkylglycidylether grafted ZIF-8 core-shell nanohybrids are designated as ZIF-8-short chain-high graft density (ZIF-8-SC-HGD) and ZIF-8-long chain-high grafting density (ZIF-8-LC-HGD), depending on the reaction time chosen. ZIF-8-long chain low-graft-density (ZIF-8-LC-LGD) was synthesized by using ZIF-8-DMI nanoparticles as the core. The synthesis details of the core-shell ZIF-8 nanohybrids are summarized in Table 3-1.

Table 3-1. Synthesis of core-shell ZIF-8 nanohybrids.

Samples	Core	Reaction time
ZIF-8-SC-HGD	ZIF-8	3 h
ZIF-8-LC-LGD	ZIF-8-DMI	18 h
ZIF-8-LC-HGD	ZIF-8	18 h

3.2.5. Preparation of PMMA/grafted ZIF-8 nanocomposites

PMMA (molecular weight = 120,000 g/mol; Arkema) was dissolved in dimethylformamide (DMF) to yield a 15 wt% polymer solution. The polymer brushes grafted ZIF-8 nanoparticles were collected by centrifugation and redispersed in DMF. The nanoparticles suspension was then added drop-wisely to the polymer solution and stirred for 1 h. The mixture was further homogenized by sonication for 0.5 h. The suspension was

dripped into a 10-fold volume excess of deionized water in a blender. After filtration and drying in vacuum at 100 °C for 12 h, the PMMA nanocomposites were obtained. Afterward, the samples were hot-pressed for 15 mins at 170 °C to obtain the test specimens for mechanical testing. The ZIF-8 core content in all the polymer nanocomposites was kept at 3 wt%.

3.2.6. Characterization

X-ray diffraction (XRD) patterns were obtained using a Bruker D8 diffractometer with Bragg−Brentano θ−2θ geometry (40 kV and 40 mA), using a graphite monochromator with Cu Kα radiation. Optical microscopy (OM) was conducted using an Olympus optical microscope (BX60) under both bright field and crossed-polarization settings. Scanning electron microscopy (SEM) images were acquired using a JEOL JSM-7500F Field Emission-SEM (FE-SEM). Transmission electron microscopy (TEM) was performed using a JEOL 1200EX. A Leica microtome was utilized to prepare thin sections with 70−100 nm in thickness for TEM imaging. Thermogravimetric analysis (TGA) analyses were carried out on a TA Instruments Q500 thermogravimetric analyzer. The temperature was increased from 30 °C to 800 °C at 10 °C/min under a 20 mL/min air flow.

3.2.7. DMA and mechanical property characterization

Tensile tests and dynamic mechanical analysis were conducted using an RSA-G2 (TA Instruments) with a tensile fixture. Tensile tests were performed at 25 °C on rectangular samples (3 mm × 0.01 mm cross-section and 30 mm in length) with a crosshead speed of 2 mm/min. Dynamic mechanical analysis (DMA) was conducted in

tensile mode at a strain amplitude of 0.05%, frequency of 1 Hz and a heating rate of 3 °C /min from room temperature to 180 °C.

3.2.8. Fracture toughness and toughening mechanism investigation

The double-notch 4-point-bend (DN-4PB) test[137,138] has been shown to be a powerful and efficient method for obtaining both fracture toughness values and investigation of their corresponding toughening mechanisms, especially when the available material for study is limited. To minimize the exhaustive synthesis required for preparing the model PMMA nanocomposite systems in this work, the DN-4PB test was adopted to investigate their fracture behavior. The DN-4PB specimens were cut into dimensions of 8.4 cm×1.25 cm×0.31 cm. The bars were then notched with a milling tool, followed by tapping with a liquid nitrogen chilled razor blade to wedge open a sharp crack. The ratio between the final crack length (a) and the specimen width (W) was held in the range between 0.3 and 0.7. A screwed-driven mechanical machine (Instron 5567) was used to conduct the DN-4PB experiments at a loading rate of 0.5 mm/min. The K_{IC} value of the samples were obtained using:

$$K_{IC} = \frac{P_Q}{BW^{\frac{1}{2}}} f(a/W) \tag{3-1}$$

where P_Q is the peak load, B is specimen thickness, W is specimen width, and $f(a/W)$ is the geometric correction factor.[138]

The double-notched 4-point-bend (DN-4PB) technique[138] was also adopted to generate a sub-critical crack tip damage. OM and TEM were employed to investigate the fracture mechanisms in the nanocomposites. The crack tip damage zone from the DN-4PB

test was embedded in an epoxy mount and stained with osmium tetroxide (OsO_4) crystals for 12 h to generate sufficient phase contrast for the modified ZIF-8 in PMMA to be observed in TEM. Thin sections of 70-100 nm in thickness were microtomed for TEM observation. The details have been reported previously.[139]

3.3. Results and discussion

3.3.1. Structure characterization

Polyalkylglycidylether grafted ZIF-8 were prepared *via* a one-step process as shown in Figure 3-1. Our previous work has shown that the imidazole group on the surface of ZIF-8 is able to initiate anionic polymerization of epoxy resin without adding catalyst.[60] The chain length of the polyalkylglycidylether brushes can be tuned by controlling the reaction time. The grafting density was adjusted by deactivating 60% of the imidazole group on ZIF-8 with a DMI capping agent (See Appendix A). In this study, three model polyalkylglycidylether grafted ZIF-8 nanoparticles were synthesized to achieve two different brush chain lengths and two different brush grafting densities (Table 3-1).

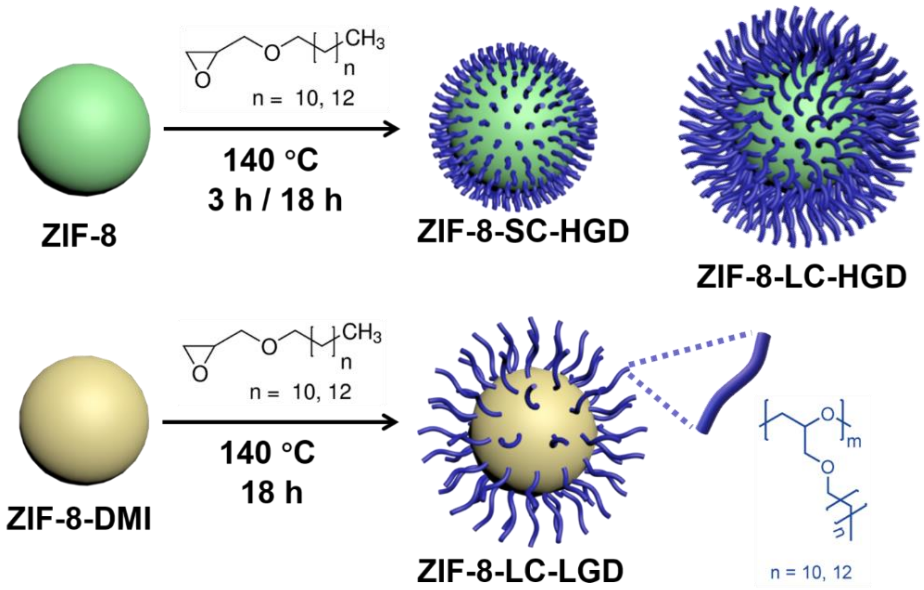

Figure 3-1. Schematic showing preparation of polyalkylglycidylether-grafted ZIF-8 core-shell nanohybrids.

The crystalline structures of ZIF-8, ZIF-8-DMI and polyalkylglycidylether-grafted ZIF-8 were investigated by XRD (Figure 3-2a). All the detected XRD patterns of the modified nanoparticles are in good agreement with pure ZIF-8, suggesting that the crystal structure of ZIF-8 is maintained throughout ligand exchange and grafting reactions. Hence, the grafting reaction only occurs on the ZIF-8 surface as expected and does not damage the MOF structure. The successful grafting of polyalkylglycidylether on ZIF-8 nanoparticles is also evidenced by FTIR spectroscopy (Figure 3-2b). A new peak at 1732 cm^{-1} corresponds to the C–H stretching vibration of the alkyl group of glycidyl ether. The new peaks appearing at ~2924 cm^{-1} and 1470 cm^{-1} correspond to the stretching of $–CH_2–$, indicating the presence of polyalkylglycidylether grafting on the ZIF-8 nanoparticles.

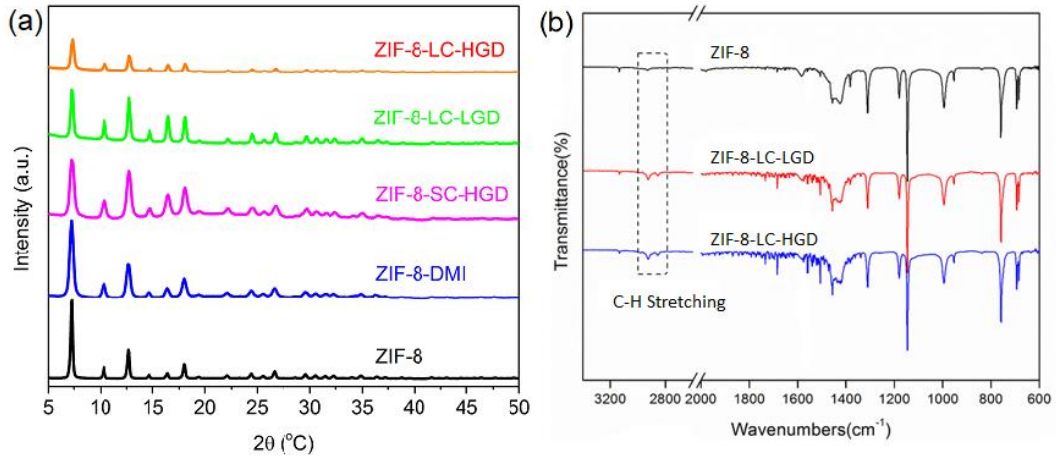

Figure 3-2. (a) XRD patterns and (b) FTIR spectra of ZIF-8 and modified ZIF-8.

The content of the polyalkylglycidylether on the grafted ZIF-8 is determined by TGA (Figure 3-3a). The additional weight loss in modified ZIF-8 can be attributed to the degradation of the polyalkylglycidylether moiety. Moreover, the polyalkylglycidylether content increases with increasing chain length and graft density. The quantitative assessment of the graft density and chain length using TGA is described in the Supporting Information. Since the entanglement molecular weight (M_e) of PMMA is in the range of 9000–13000 g/mol,[140,141] the molecular weights of the model grafted polyalkylglycidylether brushes on ZIF-8 were controlled to be either much lower (i.e., ZIF-8-SC-HGD) or much higher (i.e., ZIF-8-LC-LGD and ZIF-8-LC-HGD) than the M_e of PMMA (Table 3-2).

After the surface modification, polyalkylglycidylether-grafted ZIF-8 in DMF becomes transparent, suggesting their good dispersion. The hydrodynamic radius (R_H) of the nanoparticles were measured by DLS (Figure 3-3b and Table 3-2). ZIF-8 possesses a

R_H of 57 nm with a narrow size distribution. All the grafted ZIF-8 exhibit a larger R_H and the R_H increases with increasing chain length and higher grafting density. Moreover, the distribution of R_H becomes broader for ZIF-8 with a longer brush length and a higher graft density.

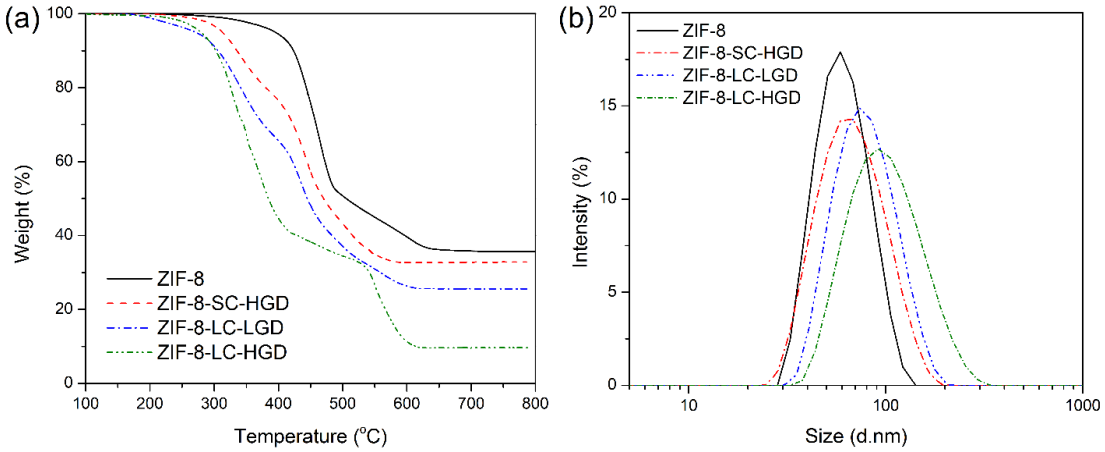

Figure 3-3. (a) TGA curves and (b) DLS curves of ZIF-8 and modified ZIF-8.

Table 3-2. The detailed composition of core-shell ZIF-8.

Samples	Content of polymer brushes (wt%)	Size (nm)	Molecular weight (g/mol)	Graft density (chain/nm^2)
ZIF-8	0	57±5	-	-
ZIF-8-SC-HGD	30	64±8	5,700	0.35
ZIF-8-LC-LGD	48	75±10	34,000	0.14
ZIF-8-LC-HGD	75	95±10	40,000	0.35

The above model core-shell ZIF-8 nanoparticles at 3 wt% were incorporated into PMMA matrix by solution mixing and coagulation. This strategy has been reported to achieve good dispersion of nanoparticles in the preparation of PMMA nanocomposites.[142] The polyalkylglycidylether-grafted chains on the ZIF-8 nanoparticles appear to exhibit sufficient affinity to the PMMA chains to avoid aggregation in PMMA. The morphologies of the model PMMA nanocomposites were characterized using TEM. As shown in Figure 3-4, all the model ZIF-8 nanoparticles are well dispersed in the PMMA matrix; no nanoparticle aggregation was observed.

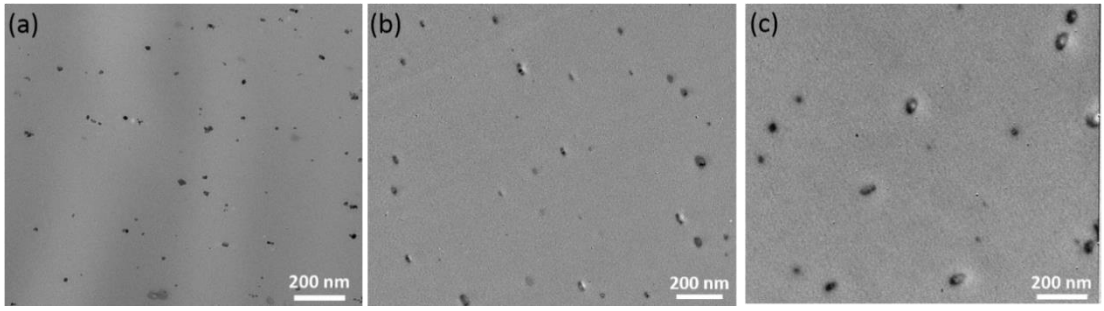

Figure 3-4. TEM images showing good dispersion of ZIF-8 nanoparticles at 3 wt% in PMMA: (a) ZIF-8-SC-HGD; (b) ZIF-8-LC-LGD; (c) ZIF-8-LC-HGD.

3.3.2. DMA study and tensile properties

DMA was performed in tensile geometry to determine the dynamic mechanical behavior of the model PMMA nanocomposites (Figure 3-5). The storage modulus at 25 °C and T_g values are summarized in Table 3-3. The entire DMA curve of PMMA/ZIF-8-SC-HGD almost overlaps with that of the neat PMMA, indicating that the short-chain brushes in ZIF-8-SC-HGD are too short to influence the dynamic mechanical behavior of

the PMMA matrix. A slight T_g drop against that of the neat PMMA are observed in both PMMA/ZIF-8-LC-HGD and PMMA/ZIF-8-LC-LGD systems. As the polyalkylglycidylether brush length increases above the entanglement molecular weight of PMMA, their long brushes will likely entangle with the surrounding PMMA chains and influences the dynamic mechanical behavior of the entire PMMA matrix. Consequently, the damping behavior of the PMMA/ZIF-8-LC-HGD and PMMA/ZIF-8-LC-LGD systems possess a lower and broader T_g and higher damping characteristics at low temperatures, which signify their increased molecular mobility due to the presence of long polyalkylglycidylether brushes on the ZIF-8 nanoparticles.

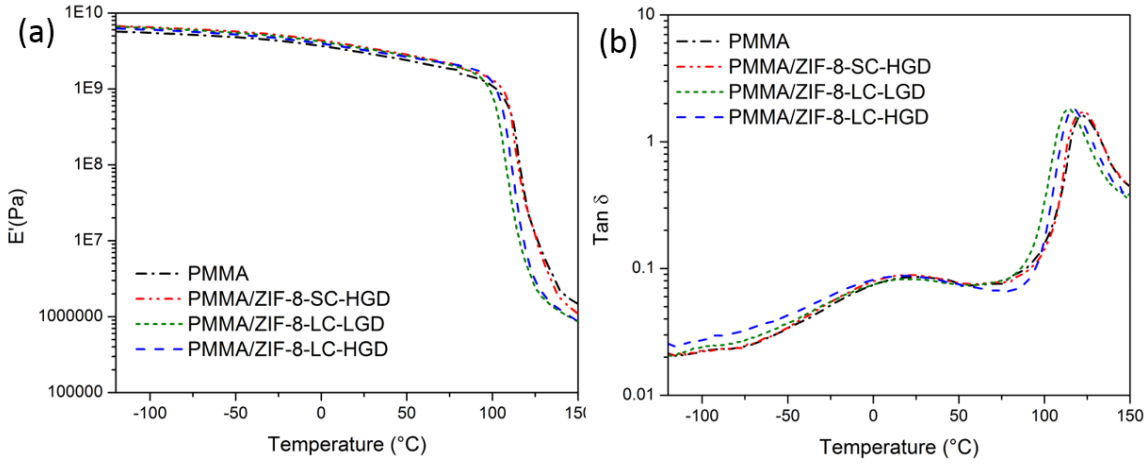

Figure 3-5. DMA plots of neat PMMA and PMMA nanocomposites: (a) Storage modulus *vs.* temperature and (b) Tan δ *vs.* temperature.

Table 3-3. Storage modulus and T_g of PMMA and the model nanocomposites.

Samples	Storage modulus (GPa) at 25 °C	T_g (°C)
PMMA	2.86	122
PMMA/ZIF-8-SC-HGD	3.38	122
PMMA/ZIF-8-LC-LGD	3.10	114
PMMA/ZIF-8-LC-HGD	3.26	116

The engineering stress−strain curves of neat PMMA and the model PMMA/ZIF-8 systems are plotted in Figure 3-6 and key tensile properties are summarized in Table 3-4. It is clearly shown that the addition of grafted ZIF-8 can achieve a slight increase in Young's modulus at room temperature. As expected, the PMMA/ZIF-8-SC-HGD shows a brittle behavior similar to that of neat PMMA. However, with long polyalkylglycidylether brushes grafting on the surface of ZIF-8, the elongation at break against neat PMMA are significantly enhanced by 70% and 150% for PMMA/ZIF-8-LC-HGD and PMMA/ZIF-8-LC-LGD, respectively. The tensile test results suggest that, with sufficient polyalkylglycidylether brush length on the 50 nm ZIF-8 nanoparticles, the ductility of the polymer matrix may be substantially increased while maintaining gains in elastic modulus and tensile strength. Similar phenomena were also observed by others.[72,143] Unlike rubber-toughened polymers, polymers reinforced by polymer brushes grafted rigid nanoparticles systems can exhibit improvement in elongation at break without compromising elastic modulus.[59,60]

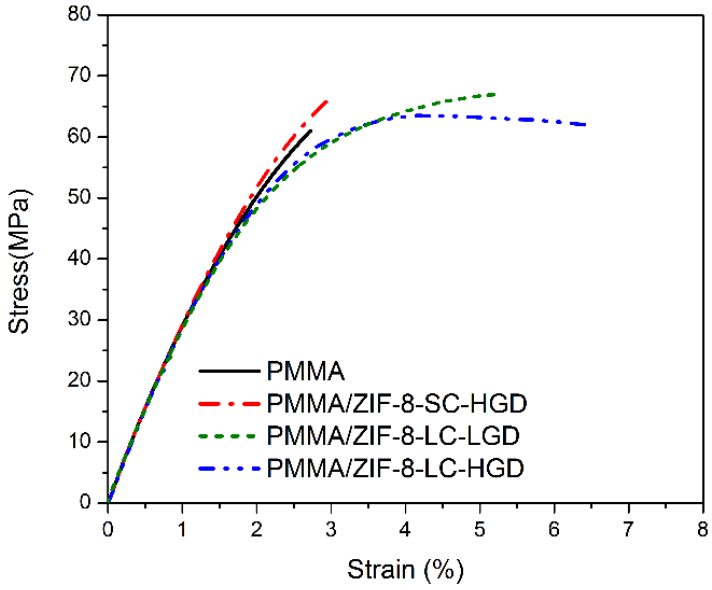

Figure 3-6. The engineering stress−strain curves of neat PMMA and model PMMA nanocomposites.

Table 3-4. Tensile properties and fracture toughness of PMMA and PMMA nanocomposites.

Samples	**Tensile strength (MPa)**	**Elongation (%)**	**Young's modulus (GPa)**	**K_{IC} (MPa $m^{1/2}$)**
PMMA	60±3	2.8±0.3	3.0±0.2	0.98±0.12
PMMA/ZIF-8-SC-HGD	65±5	3.0±0.4	3.2±0.3	1.09±0.11
PMMA/ZIF-8-LC-LGD	65±6	5.0±0.5	3.2±0.3	1.51±0.10
PMMA/ZIF-8-LC-HGD	63±5	6.6±0.8	3.3±0.5	1.81±0.06

3.3.3. Fracture toughness measurements

The fracture toughness values of neat PMMA and PMMA nanocomposite systems are summarized in Table 3-4. Compared with neat PMMA, only negligible improvement in fracture toughness is achieved for PMMA/ZIF-8-SC-HGD. However, the K_{IC} values of PMMA nanocomposites containing long-chain brushes on ZIF-8 nanoparticles show significantly higher fracture toughness than neat PMMA. These results clearly reveal that different brush characteristics grafted on the nanoparticles may lead to significantly different toughening effects. To unambiguously understand how these model polyalkylglycidylether grafted ZIF-8 nanoparticles on the fracture behavior of PMMA, their toughening mechanisms were investigated by observing the crack tip damage zones of the DN-4PB specimens using OM and TEM.[138]

3.3.4. Toughening mechanisms study

Figure 3-7 shows the OM images taken in the plane strain region of the DN-4PB damage zones of the model PMMA nanocomposites under bright field and cross-polarized light conditions. The arrows in the figures indicate the crack-tip locations. It can be seen that only a few large crazes were found at the crack tip of the PMMA/ZIF-8-SC-HGD system (Figure 3-7a), suggesting only minor improvement in fracture toughness, if any, is expected. On the other hand, much larger, but different crack tip damage zone features are observed in the two PMMA/ZIF-8-LC-HGD and PMMA/ZIF-8-LC-LGD systems. The PMMA/ZIF-8-LC-LGD system possesses a dark light scattering zone around the survived crack tip when observed from the bright field OM (Figure 3-7b). The dark zone that encompasses the crack tip and crack wake indicates a cavitation process due to debonding

or voiding between PMMA chains and the polyalkylglycidylether brushes has taken place. When viewed under cross-polarized light, a clear birefringent zone is observed within the cavitation zone (Figure 3-7e). This strongly indicates that shear banding has taken place in PMMA/ZIF-8-LC-LGD system, which accounts for the observed improvement in fracture toughness.[54,56] When the graft density is increased, a totally different massing crazing mechanism can be seen in the PMMA/ZIF-8-LC-HGD system (Figure 3-7c). Under polarized light, no detectable birefringent is observed. To further investigate the exact operative toughening mechanisms in the model PMMA nanocomposites, Careful TEM observation on the DN-4PB specimens was conducted and presented below.

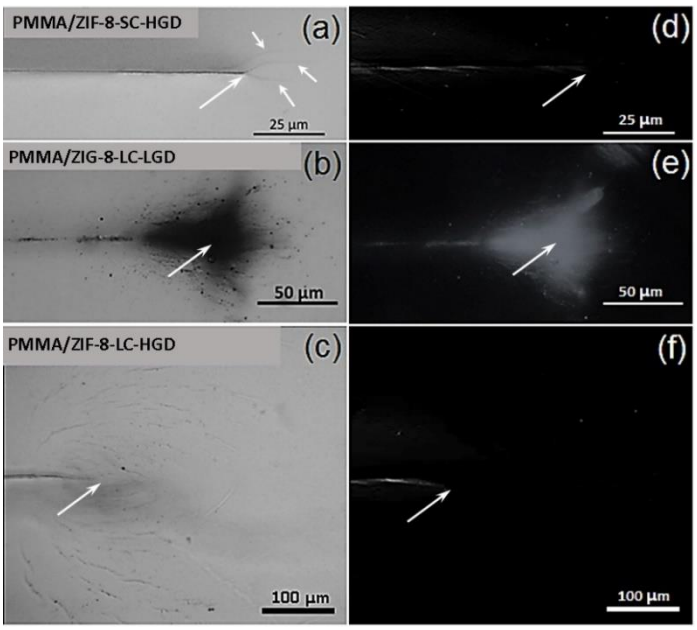

Figure 3-7. OM images of the crack tip damage zone of PMMA nanocomposites under bright field (left) and crossed-polars (right): (a)(d) PMMA/ZIF-8-SC-HGD; (b)(e) PMMA/ZIF-8-LC-LGD; (c)(f) PMMA/ZIF-8-LC-HGD. The long arrows indicate the crack-tip locations. The small arrows indicate the locations of crazes.

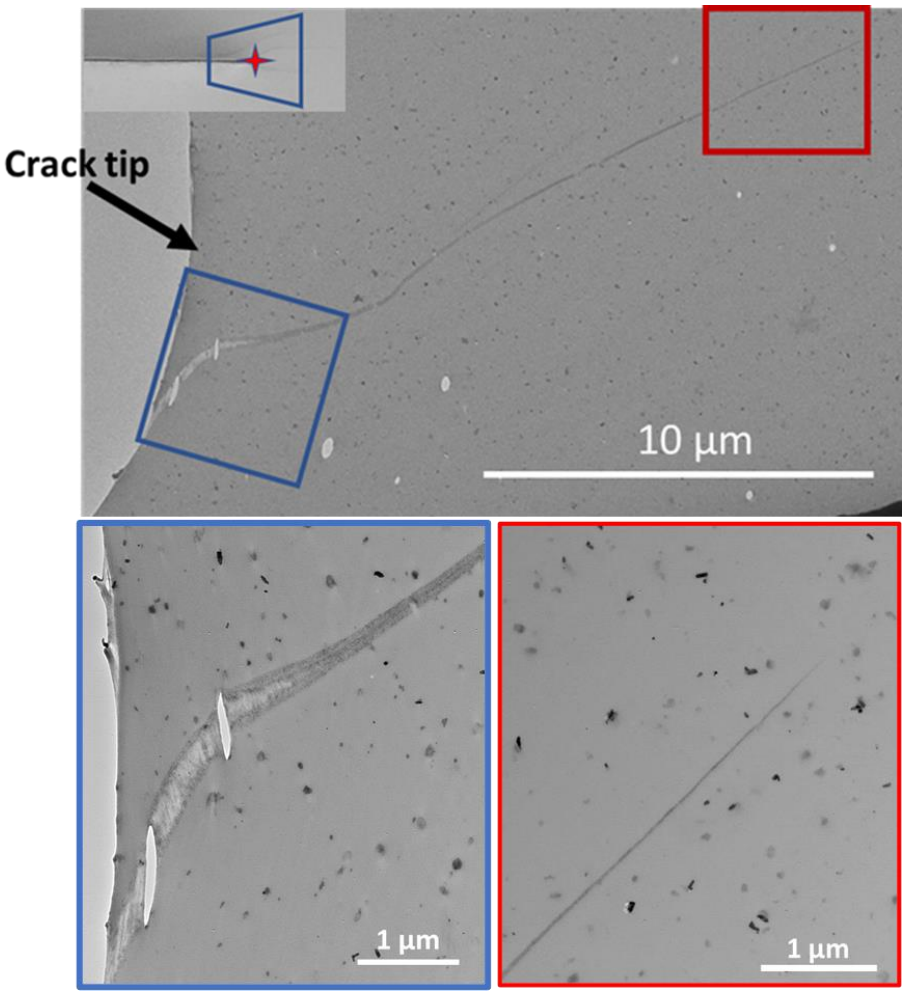

Figure 3-8. TEM micrographs showing the DN-4PB fracture mechanisms in PMMA/ZIF-8-SC-HGD.

TEM images of the sub-critically grown crack tip in PMMA/ZIF-8-SC-HGD are shown in Figure 3-8. It can be seen that ZIF-8/SC-HGD nanoparticles are well dispersed in the PMMA matrix, and one big craze grown at an angle from the main crack direction can be seen in the micrograph. This fracture behavior is similar to a typical neat PMMA.[144,145] No effective toughening mechanisms are observed. The ZIF-8-SC-HGD nanoparticles seem to be inactive in promoting any effective toughening mechanisms. No

evidence of debonding or initiation of crazes is found. Based on the above findings, it is likely that the low molecular weight and high graft density polyalkylglycidylether brushes on ZIF-8 nanoparticles can still achieve good bonding and good dispersion in PMMA, but unable to alter the viscoelastic and mechanical properties of the surrounding PMMA matrix to trigger massive crazing. Instead, the ZIF-8-SC-HGD nanoparticles behave like ineffective rigid nanoparticles with a size much smaller than the natural crack tip radius of PMMA, rendering their inability to promote crack deflection or other effective toughening mechanisms.[146]

For the PMMA/ZIF-8-LC-LGD system, weak bonding and voiding between the nanoparticles and PMMA matrix can be observed in front of the crack tip (Figure 3-7b and Figure 3-9). The debonding process is the separation of the PMMA/ZIF-8-LC-LGD nanoparticles from the PMMA matrix during deformation. For inherently ductile polymers, such as polyethylene, debonding is an important mechanism in enhancing fracture toughness of particulate-filled polymers because it allows for ductile voiding and ligament stretching.[147] For notch-sensitive and semi-ductile polymers, a cavitational process to transform the crack tip stress state from plane strain condition to a plane stress condition is required for matrix shear yielding to take place. If rigid toughening particles are chosen for toughening but unable to undergo internal cavitation like rubber particles, interfacial debonding becomes a required mechanism to promote shear banding in polymer matrix. According to the OM and TEM results, the toughening mechanisms observed here are ZIF-8 nanoparticle debonding followed by shear banding to achieve significant fracture toughness improvement. It appears that the ZIF-8-LC-LGD

nanoparticles are able to achieve good dispersion in PMMA matrix, but exhibiting a weaker interfacial strength to PMMA when compared against the ZIF-8-SC-HGD. This implies that insufficient polyalkylglycidylether coverage on ZIF-8 nanoparticle surface, even with long brushes, can lead to weaker bonding to the PMMA matrix. It is noted that the interfacial interaction between the polyalkylglycidylether long brushes and PMMA molecules is significant enough to lower the T_g of PMMA and causes the PMMA to exhibit a higher low temperature damping, thus a higher molecular mobility (Figure 3-5). This higher molecular mobility might contribute to the ability of PMMA to undergo massive shear banding to enhance fracture toughness. Future work may be needed to further elucidate this possible influence.

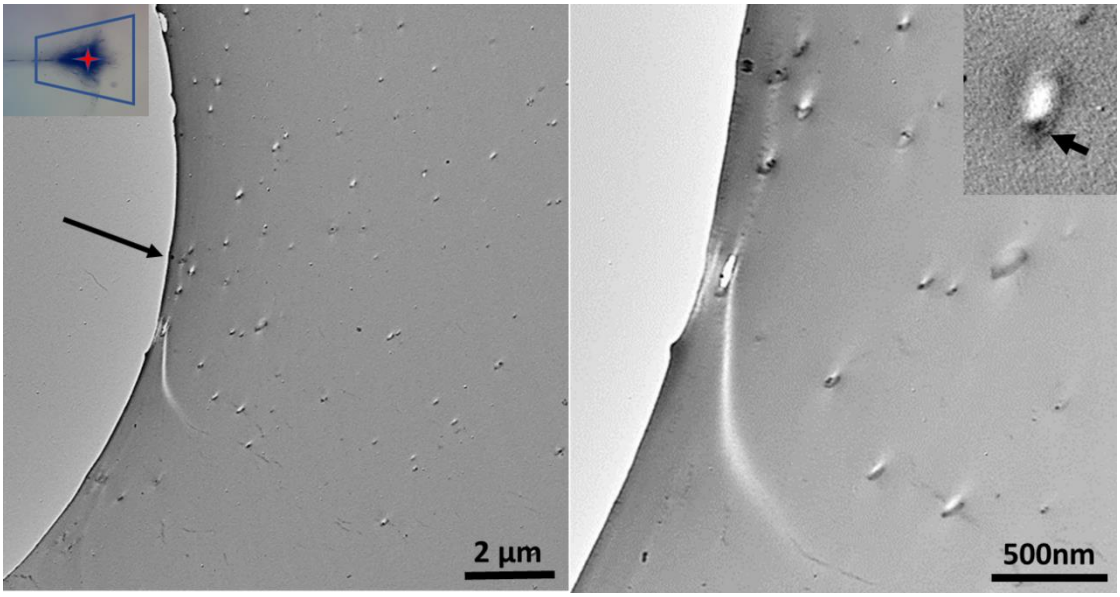

Figure 3-9. TEM micrographs showing the fracture mechanisms in PMMA/ZIF-8-LC-LGD. The arrows indicate the cavities caused by debonding and voiding of the ZIF-8 nanoparticles in PMMA.

In the case of the PMMA/ZIF-8-LC-HGD system, massive crazes can be observed in front of the DN-4PB crack tip (Figure 3-7c and Figure 3-10). A large number of micro-crazes are initiated by the nanoparticles and grow more or less along the crack propagation direction within the damage zone. As we mentioned earlier, the polyalkylglycidylether brush with a high average molecular weight of 40,000 g/mol and high graft density tend to entangle and strongly interact with the PMMA matrix, which may greatly influence PMMA molecular mobility as evidenced by the DMA behavior of this system. This leads to significant promotion of massive crazing in PMMA and greatly improves fracture toughness.

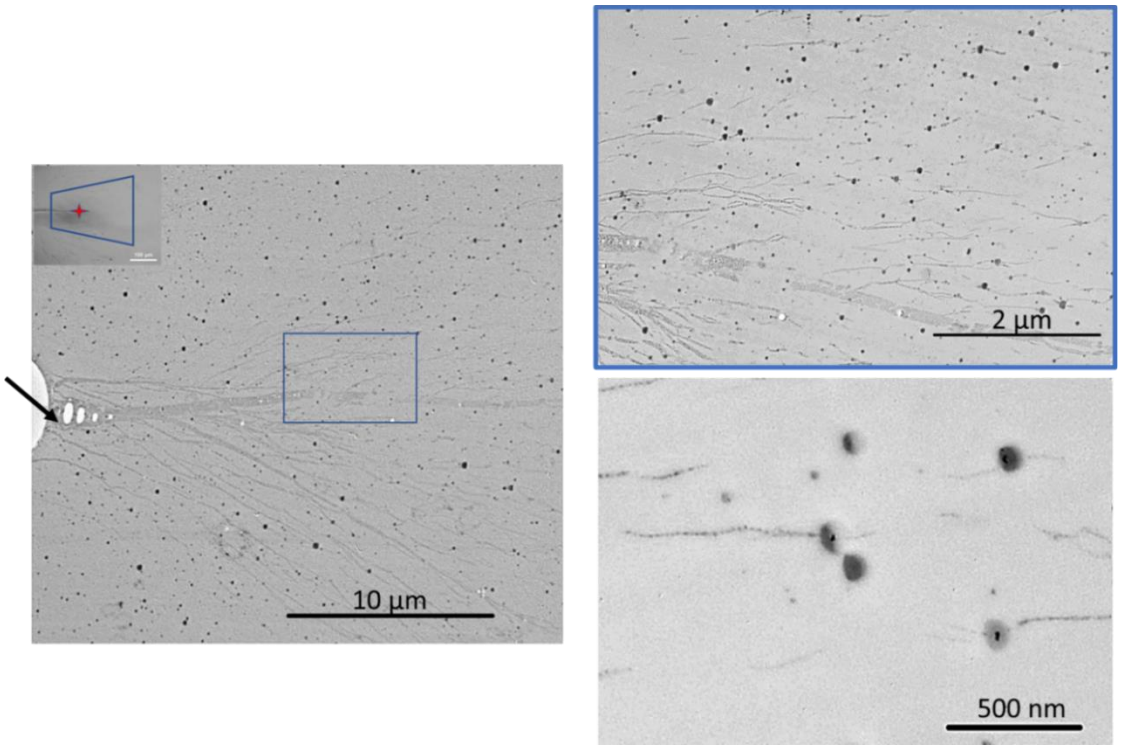

Figure 3-10. TEM micrographs showing the fracture mechanisms in PMMA/ZIF-8-LC-HGD.The arrow indicates the crack-tip location

Based on the above microscopy investigation and mechanical property study, a comprehensive understanding of the underlying fracture mechanisms of these nanocomposites is obtained. Upon fracture, only a few large crazes were formed in the PMMA/ZIF-8-SC-HGD system. In the two PMMA/ZIF-8-LC systems, effective crazing and shear banding toughening mechanisms were promoted, depending on their respective grafted polymer brush characteristics. Based on the above findings and available literature, it is evident that the molecular weight of the polymer brush needs to be higher than M_e of the host polymer matrix to achieve effective entanglements and influence the matrix mechanical and viscoelastic properties.[146]

Donald and Kramer[148] reported that the ease of craze initiation depends on the particles size and that crazes are rarely initiated by rubber particles smaller than 1 μm. Weon et al. found that massive crazes were initiated by rigid $CaCO_3$ nanoparticles with a 44 nm in diameter. The incorporation of $CaCO_3$ nanoparticles induces the formation of β-phase crystal around them, which triggers crazing formation and grow in the a-phase dominant PP matrix.[131] Liu et al. investigated nanorubber-toughened epoxy and found that rubber particles with 15 nm in size can significantly improve epoxy fracture toughness without compromising its Young's modulus.[149]

The above studies clearly suggest that the molecular scale mobility responsible for modulus, ductility, T_g, and toughenability improvements in polymers may not be the same and can be tailored. In the present study, the model PMMA nanocomposite systems were designed to have the MOF nanoparticle to exhibit a modulus comparable to the PMMA matrix to determine how the modulus of PMMA can be affected by the

polyalkylglycidylether brush length and grafting density. The grafted polyalkylglycidylether brushes on ZIF-8 were also controlled to be significantly below and significantly higher than the entanglement molecular weight of PMMA to investigate how they would influence the ductility and toughenability of the PMMA matrix. With only 3 wt% addition of ZIF-8 in PMMA, the ability of the grafted polyalkylglycidylether brushes on the PMMA matrix ductility and toughenability is enormous. This leads to the observed significant improvements in PMMA ductility and toughenability. The present findings strongly indicate that it is highly possible to prepare high performance polymer nanocomposites with greatly improved mechanical properties without sacrificing other physical properties.

3.4. Conclusion

The fracture behavior based on a set of model PMMA nanocomposite systems containing polyalkylglycidylether grafted ZIF-8 nanoparticles were systematically investigated. The nanoparticle surface has been manipulated by grafting different length and grafting density of polyalkylglycidylether brushes. It is found that polymer brushes grafted ZIF-8 nanoparticles greatly enhances the fracture toughness of the PMMA matrix while maintaining the Young's modulus. Our results also reveal that the model systems toughened by nanoparticles with different polymer brush characteristics may lead to distinctly different toughening mechanisms from a few big crazes to massive crazing, and to nanoparticle voiding and matrix shear banding. High performance multifunctional polymer nanocomposites with high fracture toughness can be successfully designed and prepared.

4. MECHANICAL BEHAVIOR OF SELF-CURING EPOXY NANOCOMPOSITES[†]

4.1. Introduction

The reinforcement of polymers with nanoclay has been investigated for several decades. Exfoliation of nanoclay in a polymer matrix has the potential to greatly improve polymer properties, such as gas barrier, coefficient of thermal expansion, modulus, flame retardation, and other properties. Although theory predicts that dramatic improvements of these properties can be achieved, the actual known improvements in properties are found to be modest.[150]. The reason for this disappointment is primarily due to the lack of nanoclay exfoliation and dispersion in polymer matrix in practice. This results in agglomerated or non-exfoliated particles that have low aspect ratios and low surface area to exert effective reinforcement.[151-155] It has been shown that synthetic α-zirconium phosphate ($Zr(O_3POH)_2 \cdot H_2O$, α-ZrP) nanoclay, which was first prepared by Clearfield and Stynes in 1964,[156] possesses many advantages over the natural clay, such as well-defined chemical structure, high purity, large ion-exchange capacity, ease of intercalation/exfoliation, and controllable surface functionality.[56,157-159]

Exfoliation of α-ZrP nanoplatelets in epoxy has been shown to be rather straightforward using surfactants such as quaternary ammonium hydroxide and long-chain amines,[159,160] such as the Jeffamine M series, having polyols terminated on one end by an amine.[56,161,162] The Young's modulus and yield stress of these nanocomposites were

[†] Reprinted with permission from "Mechanical behavior of self-curing epoxy nanocomposites" by Liu, C., Zhu, Z., Molero, G., Chen, Q., Kotaki, M., Mullins, M., & Sue, H. J., **2019**. Polymer, 179, 121631, Copyright 2019 by Elsevier Ltd.

greatly improved due to the high stiffness of α-ZrP, high surface area of exfoliated nanoplatelets, and free from particle agglomeration.[161] However, the toughness of the epoxy matrix was reduced drastically due to the rigid α-ZrP nanofillers, which suppresses the neighboring epoxy molecular mobility and causes embrittlement of the matrix.

Rubber toughening is a well-known strategy to improve the fracture toughness of brittle polymers.[54,55] With the addition of core-shell rubber (CSR), the fracture toughness of the polymer matrix can be significantly improved, sometimes by an order of magnitude.[56,57] The use of CSR to toughen epoxy/α-ZrP (2 vol%) nanocomposites has also been shown to be effective.[57] However, this epoxy nanocomposite utilized a monoamine surfactant for the exfoliation of α-ZrP, which causes a significant reduction in crosslinking density and a drop in T_g of the epoxy matrix. Reduction in the amount of surfactant is one strategy to decrease their negative impact on crosslink density and T_g, but the degree of nanoplatelet exfoliation will be compromised.[56]

Imidazoles are known to be highly active for curing epoxy resins.[163] For example, a liquid mixture consisting of imidazoles and epoxy resins can gel quickly at room temperature. This makes it difficult as an industrial process to fabricate electronic and structural components.[164] Shimomura et al.[165,166] have shown that imidazole and amine-intercalated α-ZrP hybrids are latent initiators of glycidyl phenyl ether (GPE) and hexahydro-4-methylphthalic anhydride (MHHPA). The hybrids have been shown to be ideal as latent catalysts. The intercalated imidazole and alkylamine act as initiators while the α-ZrP serves as a reinforcing agent. However, the imidazole and alkylamine cannot exfoliate α-ZrP, rendering it ineffective.

In this report, we describe the preparation of self-curing epoxy/α-ZrP nanocomposites that possess high T_g and high modulus. Tetrabutylammonium hydroxide (TBA) was chosen both as a surfactant and a catalytic curing agent. TBA is effective in exfoliating α-ZrP into individual nanoplatelets in an epoxy suspension.[159] It is noted that no additional curing agent is needed in this case since the phosphonate anions on the α-ZrP surface act as catalytic initiators for epoxy ring-opening, forming quaternary ammonium cation (TBA) as a catalyst.[167,168] The α-ZrP therefore becomes covalently bonded to the epoxy matrix, which may help to greatly improve the Young's modulus. Furthermore, to learn whether or not the epoxy/α-ZrP-TBA can be toughened by nano-sized core-shell rubber (CSR) particles for possible structural applications, CSR having a uniform particle size of 100 nm was chosen to toughen epoxy/α-ZrP-TBA. The usefulness of the present study on the preparation of high-performance epoxy nanocomposites and the fundamental knowledge related to the toughening of epoxy nanocomposites is pursued and discussed.

4.2. Experimental section

4.2.1. Synthesis and exfoliation of α-ZrP

The α-ZrP nanocrystals were synthesized following the previous literature.[160] First, 20.0 g of zirconyl chloride octahydrate and 200 mL of 3.0 M H_3PO_4 were added to a 500 mL round-bottomed flask and stirred for 30 min at room temperature. Next, the reaction mixture was refluxed for 24 h. After the reaction, α-ZrP was washed with 100 mL of deionized (DI) water for three times.

The exfoliation of α-ZrP by TBA (Aldrich) was carried out in an aqueous dispersion according to the literature.[159] α-ZrP in an amount of 0.3 g was dispersed in 200 mL water by sonication for 1 h. The concentration of α-ZrP is 5×10^{-3} mol/L. Then, 0.65 g of TBA stirring solution (40 wt% in H_2O, 259.5 g/mol) was added dropwise to the α-ZrP dispersion. The molar ratio between α-ZrP and TBAOH is 1:1. The mixture was stirred overnight, then sonicated for about 30 min until the solution became transparent. The exfoliated α-ZrP nanoplatelets in aqueous dispersion were then exchanged into acetone using dialysis tubes (Ward's science, 10,000 M_w cut-off) to remove excess surfactants. The concentration of α-ZrP was controlled at 5×10^{-3} mol/L to maintain a good dispersion in acetone.

4.2.2. Preparation of epoxy nanocomposites

The epoxy monomer used in this study is a diglycidyl ether of bisphenol F (DGEBF) epoxy resin (D.E.R. 354 epoxy resin, The Dow Chemical Company), which has an epoxy equivalent weight of 165−168 g/mol. The volume percent shown throughout this work refers only to the α-ZrP component in the epoxy system.

The α-ZrP-TBA nanoplatelets in acetone were mixed with the epoxy monomer to achieve an α-ZrP loading of 4 vol% in the final nanocomposite. After moderate stirring and sonication to achieve a homogeneous dispersion, acetone was removed with a rotary evaporator in a water bath at 60 °C for 1 h. The mixture was precured at 80 °C for 0.5 h in a vacuum oven to increase the viscosity and remove the trapped solvent. The B-staged epoxy compound was poured into a preheated glass mold which was treated with PTFE

release agent. The sample was then cured at 100 °C for 2 h and 140 °C for 4 h in hot press to form an epoxy/α-ZrP-TBA nanocomposite thin film with a thickness of 80-100 μm.

To prepare CSR toughened epoxy nanocomposites, a pre-dispersed epoxy/CSR resin with a concentration of 25 wt% CSR (Kaneka Corporation) was added into the mixture of α-ZrP-TBA and epoxy, the final concentration of α-ZrP-TBA and CSR in epoxy is 4 vol% and 3 vol%, respectively. Neat epoxy was also prepared as a reference using 2-methyl imidazole (2MI) as the curing agent. The mass fraction of 2MI is 1.7 wt%, which is the same as the molar concentration of TBA in the epoxy/α-ZrP-TBA nanocomposites. Epoxy/α-ZrP-TBA/CSR and neat epoxy were prepared following the curing process as mentioned above.

Epoxy/α-ZrP-TBA/CSR nanocomposite bulk samples were also prepared to determine fracture toughness and investigate their corresponding toughening mechanisms. After degassing, epoxy/α-ZrP-TBA/CSR was poured into a preheated glass mold to make a plaque with dimensions of 200 mm × 200 mm × 3 mm. The resin was cured in an oven with a curing schedule of 60 °C for 24 h and 120 °C for 2 h, followed by 4 h at 140 °C.

4.2.3. Characterization

X-ray diffraction (XRD) patterns were obtained using a Bruker D8 diffractometer with Bragg−Brentano θ−2θ geometry (40 kV and 40 mA), using a graphite monochromator with Cu Kα radiation. Optical microscopy (OM) was conducted using an Olympus optical microscope (BX60) under both bright field and crossed-polarizers. Scanning electron microscopy (SEM) images were acquired using a Zeiss Leo 1530 VP Field Emission-SEM (FE-SEM). Transmission electron microscopy (TEM) was

performed using a JEOL 1200EX. A Leica microtome was utilized to prepare thin sections with 70−100 nm in thickness for TEM imaging.

Thermogravimetric analysis (TGA) analyses were carried out on a TA Instruments Q500 thermogravimetric analyzer. Temperature was increased from 30 °C to 800 °C at 10 °C/min under a 20 mL/min O_2 flow. Differential scanning calorimetry (DSC) was carried out at various heating rates using TA Instruments Q20.

The Kissinger method was used to calculate the activation energy and the pre-exponential factor of the cure of epoxy resin examined in this study.[169] The equation for the Kissinger method can be defined as:

$$ln\left(\frac{\beta}{T_p^2}\right) = \ln\left(\frac{AR}{E_a}\right) - \frac{E_a}{RT_p} \tag{4-1}$$

where R is the universal gas constant, β is the heating rate, T_p is the peak temperature. By plotting $ln(\beta/T_p^2)$ *versus* $1/T_p$, the values of activation energy, E_a, and pre-exponential factor, A, can be determined by calculating the slope of the linear fit and the y-axis intercept. It can be assumed that the maximum reaction rate, $d\alpha/dt$ (α represents conversion rate), occurs at the peak temperature, at which point $d^2\alpha/dt^2$ is equal to zero.

4.2.4. DMA and mechanical property characterization

Tensile tests and dynamic mechanical analysis were conducted using an RSA-G2 (TA Instruments) with a tensile fixture. Tensile tests were performed at 25 °C on rectangular samples (3 mm × 0.01 mm cross section and 5 mm in length) with a crosshead speed of 10 mm/min. Dynamic mechanical analysis (DMA) was conducted in tensile

mode at a strain amplitude of 0.05%, frequency of 1 Hz and a heating rate of 3 °C /min from room temperature to 180 °C.

4.2.5. Fracture toughness measurements

Both the single-edge notch tension (SENT) test and the double-notch 4-point-bend (DN-4PB) test were performed to determine the fracture toughness.[137,138] The dimensions of specimen for SENT are given in ASTM D1708-13. A razor blade chilled by liquid nitrogen was used to produce a sharp, straight initial crack. The ratio of crack length to the sample width was controlled to around 1/3. The samples were tested in uniaxial tension on an RSA-G2 at a loading rate of 0.5 mm/min. The K_{IC} value of the samples were calculated using:

$$K_{IC}=f(a/W)\cdot\sigma\sqrt{a} \tag{4-2}$$

where $f(a/W)$ is the geometric correction factor (for SENT specimens, $f(a/W) = 1.12\sqrt{\pi}$, σ is the tensile strength and a is the initial crack length. In all cases, the samples failed in a brittle fashion. Dimensions of DN-4PB specimens are 8.4cm×1.25cm×0.31cm. The bars were notched with a milling tool, followed by tapping with a liquid nitrogen chilled razor blade to wedge open a sharp crack. The ratio between the final crack length (a) and the specimen width (W) was held in the range between 0.3 and 0.7. A screwed-driven mechanical machine (Instron 5567) was used to conduct the DN-4PB experiments at a loading rate of 0.5 mm/min. The K_{IC} value of the samples were obtained using:

$$K_{IC}=\frac{P_Q}{BW^{\frac{1}{2}}}f(a/W) \tag{4-3}$$

where P_Q is the peak load, B is specimen thickness, W is specimen width, and $f(a/W)$ is the geometric correction factor.[138]

The double-notched 4-point-bend (DN-4PB) technique[138] was adopted to generate a sub-critical crack tip damage. OM and TEM were employed to investigate the fracture mechanisms in CSR-modified epoxy/α-ZrP-TBA nanocomposites. The crack tip damage zone from the DN-4PB test was embedded in an epoxy mount and stained with osmium tetroxide (OsO_4) crystals for 12 h to harden the rubber phase in epoxy. Thin sections of 70-100 nm in thickness were prepared for TEM observation. The details have been reported previously.[139]

4.3. Results and discussion

4.3.1. Morphological characterization

As shown in Figure 4-1a, the structure and d-spacing of α-ZrP and α-ZrP-TBA were confirmed by XRD analysis. The average size of the α-ZrP is about 100 nm (Figure 4-1b). After exfoliation, the peak of α-ZrP shifted from 11.7° (7.6 Å) to 5.0° (17.5 Å), suggesting the layered structure has been completely intercalated with TBA. The composition of α-ZrP-TBA was determined by TGA analysis (Figure B-1) and the amount of grafted TBA is found to be about 30 wt%.

The morphology of epoxy nanocomposites was characterized using XRD and TEM. No characteristic α-ZrP peak is observed in the XRD patterns of nanocomposites (shown in Figure B-2), indicating the α-ZrP nanoplatelets are fully exfoliated. Further, the α-ZrP-TBA exfoliation is confirmed by TEM. As shown in Figure 4-2, α-ZrP nanoplatelets are loosely dispersed in epoxy and no aggregation or tactoids are found.

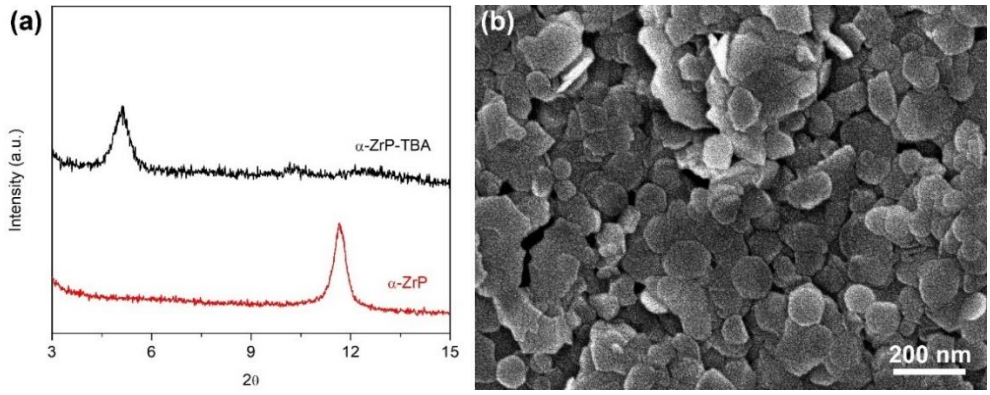

Figure 4-1. (a) XRD patterns of α-ZrP and exfoliated α-ZrP-TBA. (b) SEM image of α-ZrP.

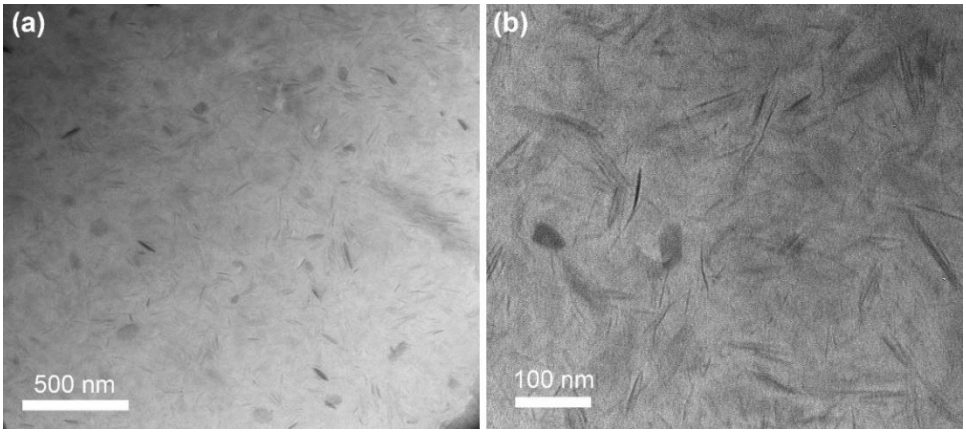

Figure 4-2. TEM of epoxy/α-ZrP-TBA nanocomposite at (a) low and (b) high magnification.

4.3.2. Curing behavior

Quaternary onium salts have been widely reported to serve as initiators for ring opening reaction of epoxide.[167,168] In this work, we postulate that quaternary ammonium (QA) salt participates in the epoxy curing process as depicted in Figure 4-3. First, QA ion (1) binds to the oxygen atom of epoxide, affording a precursor complex (2) in a transitional

state, which then generates a ring-opened anion (3). Subsequently, the resulting QA ion pairs (3) will trigger the ring-opening of the remaining neighboring epoxides in the system by nucleophilic attack of oxygen atoms. This reaction route is considered as an anionic ring-opening polymerization initiated by QA salts on α-ZrP nanoplatelets.

It has been demonstrated that α-ZrP can be modified by multiple reactive groups [170] including epoxides.[171] In order to evaluate the reactivity and storage life of α-ZrP-TBA as a curing agent, 2-methyl imidazole was chosen as a reference.

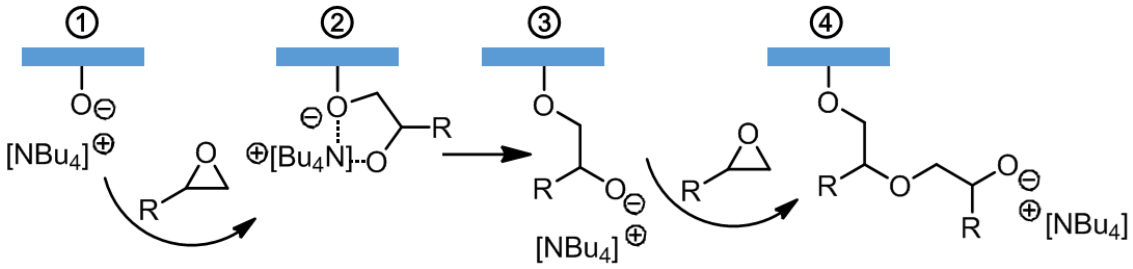

Figure 4-3. Mechanism of α-ZrP-TBA initiates ring opening reaction of epoxy.

Non-isothermal DSC was utilized to investigate the curing behaviors of epoxy/α-ZrP-TBA system as shown in Figure 4-4a. Epoxy/α-ZrP-TBA system shows an exothermic peak at 110 °C corresponding to epoxy resin curing reaction, which is similar to that of 2MI (120 °C), indicating that α-ZrP-TBA has comparable reactivity as 2MI.

The activation energy (E_a) is one important parameter to evaluate the curing kinetics. Based on the Kissinger method [169], the E_a values was calculated from the slope of the linear function $ln(\beta/T_p^2)$ *vs.* $1/T_p$ as plotted in Figure 4-4c. The E_a and curing peak are summarized in Table 4-1. The E_a of epoxy/α-ZrP-TBA is higher than that of

epoxy/2MI, suggesting a slower reaction rate. The storage stabilities of epoxy/α-ZrP-TBA and epoxy/2MI were evaluated by measuring the changes in their viscosity at room temperature (25 °C) as a function of time (Figure 4-4d). Epoxy resin compositions containing 2MI show a drastic increase in viscosity in a short period of time, resulting in solidification. In contrast, the epoxy resin with an equivalent molar amount of α-ZrP-TBA exhibits a much better storage stability, as shown in Figure 4-4d.

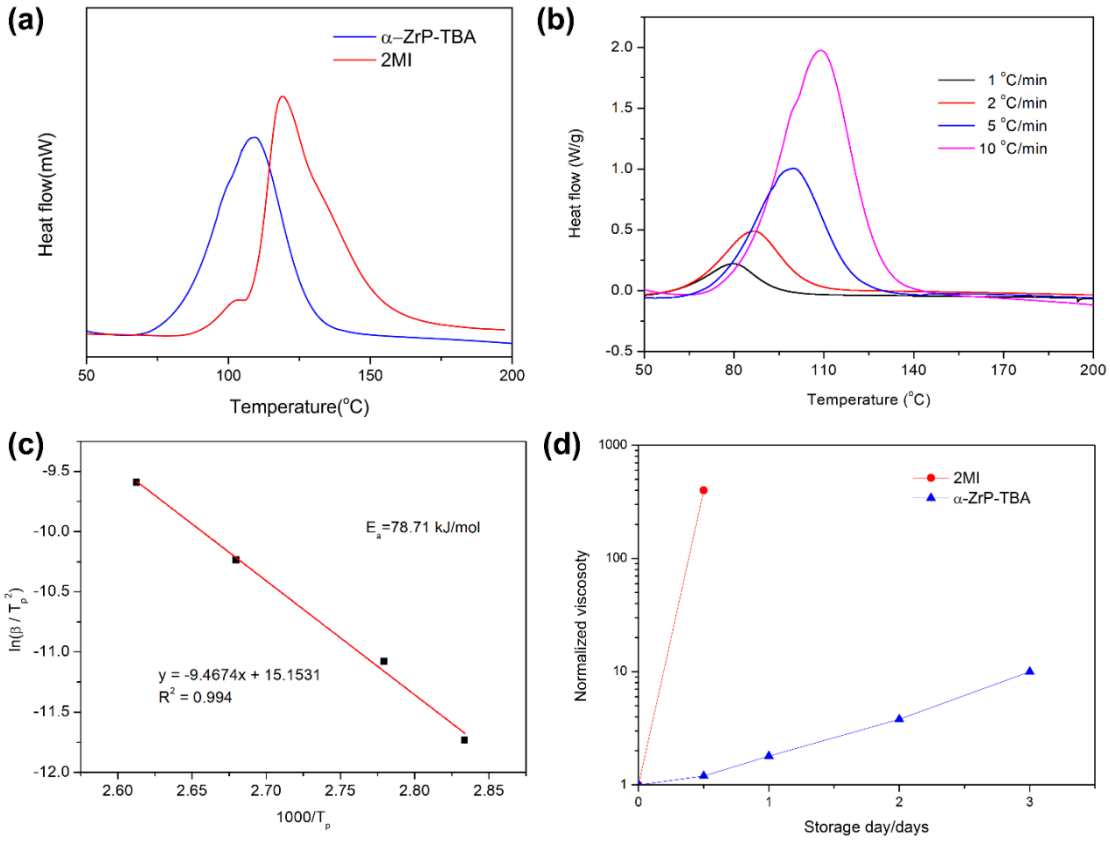

Figure 4-4. (a) DSC curves of epoxy/2MI and epoxy/α-ZrP-TBA at a heating rate of 10 ºC/min; (b) DSC curves of epoxy/α-ZrP-TBA at various heating rates; (c) Activation energy of epoxy/α-ZrP-TBA curing reaction; (d) Storage stability of epoxy/2MI and epoxy/α-ZrP-TBA.

Table 4-1. Curing peak temperature and E_a of epoxy/2MI and epoxy/α-ZrP-TBA.

Composition	Curing peak temperature (°C)	E_a (kJ/mol)
epoxy/2MI	120	60.26
epoxy/α-ZrP-TBA	110	78.71

As a catalytic curing agent, α-ZrP-TBA shows a similar reactivity at high temperature but better storage stability than 2MI at room temperature. It is postulated that the high loading of α-ZrP nanoplatelets in epoxy might suppress the mobility of epoxy resins and consequently slow down the reaction rate. Therefore, α-ZrP-TBA shows a much lower reactivity at room temperature, while at elevated temperature, the ring-opening reaction rate is accelerated and become comparable to that of epoxy/2MI system.

4.3.3. DMA and mechanical properties

DMA was performed in tensile film geometry to determine dynamic mechanical behavior of the epoxy nanocomposites. As shown in Figure 4-5a, compared with neat epoxy cured by 2MI (same molar amount as TBA in epoxy/α-ZrP-TBA), the storage modulus *E'* of epoxy/α-ZrP-TBA is increased by 80% with an addition of 4 vol% α-ZrP at room temperature. It should be noted that the storage modulus is increased much more significantly (~380%) at rubbery plateau. This same phenomenon has been observed in other polymer nanocomposite systems.[56,159,172,173] This significant increase in modulus could be attributed to the effective retardation of molecular motion in the presence of α-ZrP at temperature above T_g [174,175]. Based on the DMA analysis, epoxy/α-ZrP-TBA

exhibits about 20 °C lower T_g than neat epoxy cured by 2MI, and a broader tan δ peak is observed, suggesting that epoxy/α-ZrP-TBA might possess lower and inhomogeneous crosslinking density due to the concentrated distribution of TBA on and near the surface of α-ZrP-TBA.

Nonetheless, the amount of reduction in T_g of epoxy/α-ZrP-TBA is less than that of other epoxy nanocomposites containing monoamine as a surfactant with the same loading of nanoplatelets (Table B-1).[161] We surmise that the ZrP-TBA catalyzed epoxy crosslinking does not leave behind unreacted dangling chains caused by monoamine and give rise to a more complete epoxy curing. With an addition of 3 vol% CSR, as expected, the storage modulus is decreased by 10%, but T_g is increased slightly and the tan δ peak width becomes narrower probably due to the interaction between the glycidyl methacrylate functional group on the copolymer shell of the CSR particles with epoxy resins.[57]

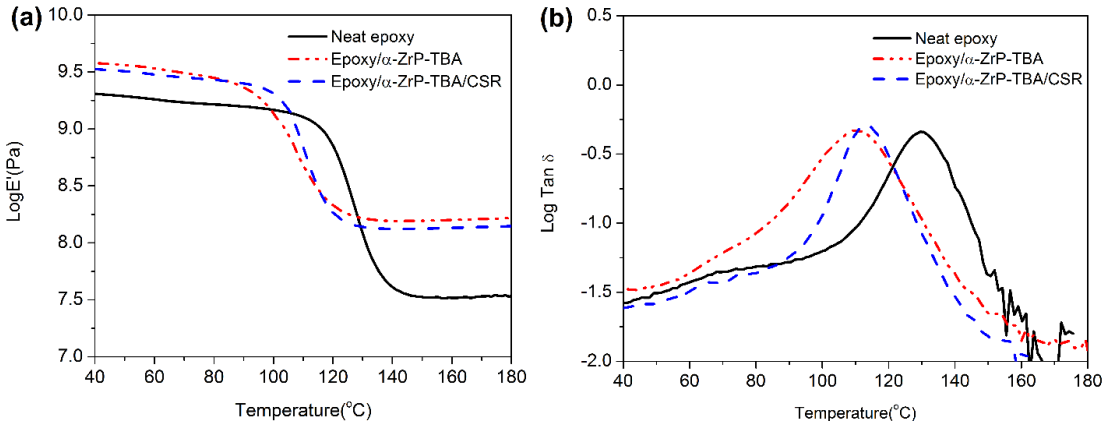

Figure 4-5. DMA plots of neat epoxy, epoxy/α-ZrP-TBA and epoxy/α-ZrP-TBA/CSR nanocomposites: (a) Storage modulus *vs.* temperature and (b) Tan δ *vs.* temperature.

The Young's moduli of the epoxy nanocomposites and neat epoxy are summarized in Table 4-2. With the addition of α-ZrP-TBA, the Young's modulus increases from 2.5 to 4.3 GPa, which is expected.[157,176-180] With the addition of CSR, the Young's modulus decreases by 10%, which is consistent with our previous study about CSR toughened epoxy nanocomposites.[57]

Table 4-2. Tensile properties and fracture toughness of epoxy and epoxy nanocomposites.

Samples	**Young's Modulus (GPa)**	**K_{IC} (MPa $m^{1/2}$) (plane stress)**	**K_{IC} (MPa $m^{1/2}$) (plane stain)**
Neat epoxy	2.5±0.1	0.76±0.24	-
Epoxy/α-ZrP-TBA	4.3±0.1	0.55±0.09	-
Epoxy/α-ZrP-TBA/CSR	3.9±0.2	1.21±0.14	1.55±0.07

4.3.4. Fracture toughness measurements and toughening mechanism investigation

Because of the large amount of α-ZrP needed for mechanical testing and the brittle nature of both neat epoxy and epoxy/α-ZrP-TBA, only the thin film SENT geometry was chosen for determining their K_{IC} values. It is noted that the effect of specimen thickness on fracture toughness values for brittle polymers is minimal.[137,181] However, upon toughening using CSR, the epoxy/α-ZrP-TBA/CSR may become much tougher and need a thicker specimen for obtaining valid fracture toughness values. To do so, specimen

thicknesses of both 100 μm and 3.12 mm were chosen to obtain K_{IC} values for both plane stress and plane strain conditions.

The fracture toughness values of neat epoxy and epoxy/α-ZrP-TBA nanocomposite systems with and without CSR can be found in Table 4-2. Compared with neat epoxy, a 20% drop of KIC for epoxy/α-ZrP-TBA is observed. This reduction in KIC is likely due to the drop on epoxy ductility caused by restricted molecular mobility of epoxy molecules around the α-ZrP nanoplatelets. Furthermore, the exfoliated nanoplatelet dimensions are too small to trigger effective toughening mechanisms, such as crack bridging, crack deflection, and crack blunting.[158] Consequently, deterioration in K_{IC} is detected in epoxy/α-ZrP-TBA nanocomposite. When CSR is introduced to toughen epoxy/α-ZrP-TBA, a significant increase in fracture toughness values, i.e., from 0.55 to 1.21 and 1.55 MPa $m^{1/2}$ for plane stress and plane strain conditions, respectively, are observed. The CSR particles are expected to serve as stress concentrators in the epoxy matrix to toughen epoxy/α-ZrP-TBA under plane stress condition, i.e., no CSR cavitation is needed.[182] In the case of the plane strain condition, the high magnitude of stress triaxiality in front of the crack tip needs to be relieved to allow for shear banding to take place in epoxy. To confirm the above conjecture, the toughening mechanisms in epoxy/α-ZrP-TBA/CSR were investigated by observing the crack tip damage zone of the DN-4PB specimens using OM and TEM.[138]

Figure 4-6 shows the OM images taken in the plane strain region of the DN-4PB damage zone under bright field and cross polarized light conditions. As shown, when CSR particles are added to the epoxy/α-ZrP-TBA system, a faint rubber particle cavitation zone

exists around the survived crack tip of the DN-4PB specimen from the bright field OM (Figure 4-6a). The dark zone that encompasses the crack tip and crack wake indicates a cavitation process has taken place. Around the crack wake and the crack tip, a clear birefringent zone under cross-polarized light is also observed (Figure 4-6b). This indicates that shear banding has taken place inside the damage zone.[54,56]

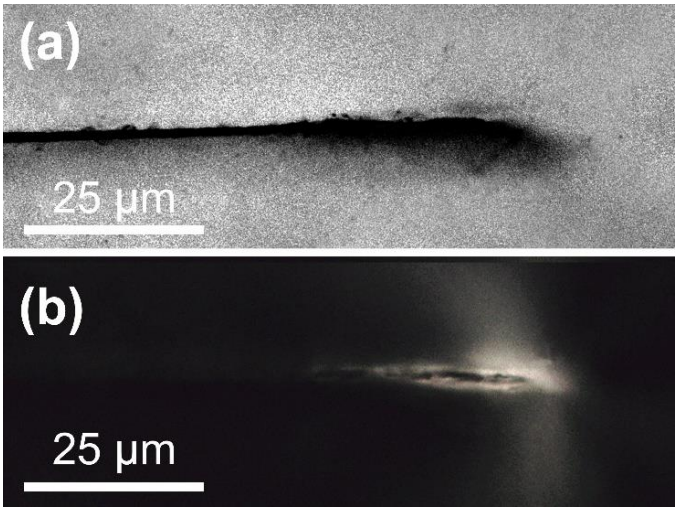

Figure 4-6. OM images of crack tip damage zone of epoxy/α-ZrP-TBA/CSR nanocomposite at (a) bright field and (b) crossed-polars.

In the region outside the cavitation zone (Figure 4-7a), intact and undeformed CSR particles are found. In the plane strain region of the DN-4PB crack tip, cavitation of CSR particles is evident (Figure 4-7b and c). Exfoliated α-ZrP layers are well dispersed in the matrix, which indicates that the addition of CSR does not affect the dispersion of α-ZrP. Under the plane stress condition, no sign of CSR particle cavitation is found (Figure 4-8). The toughening mechanisms observed here is consistent with the well-understood

toughening principle that, under the plane strain condition, the CSR cavitation helps relieve the triaxial stress state at the crack tip, subsequently facilitating matrix shear banding.

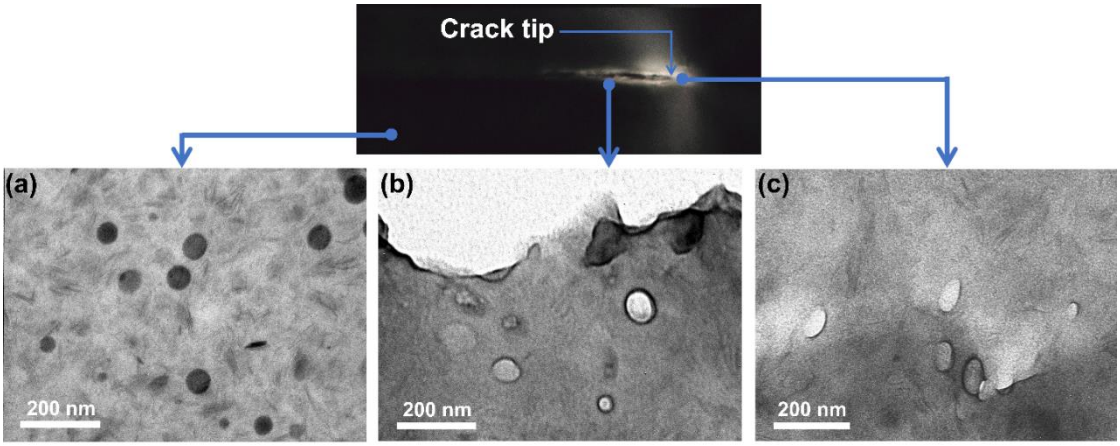

Figure 4-7. TEM of epoxy/α-ZrP-TBA/CSR nanocomposite in the plane strain region of the DN-4PB specimen.

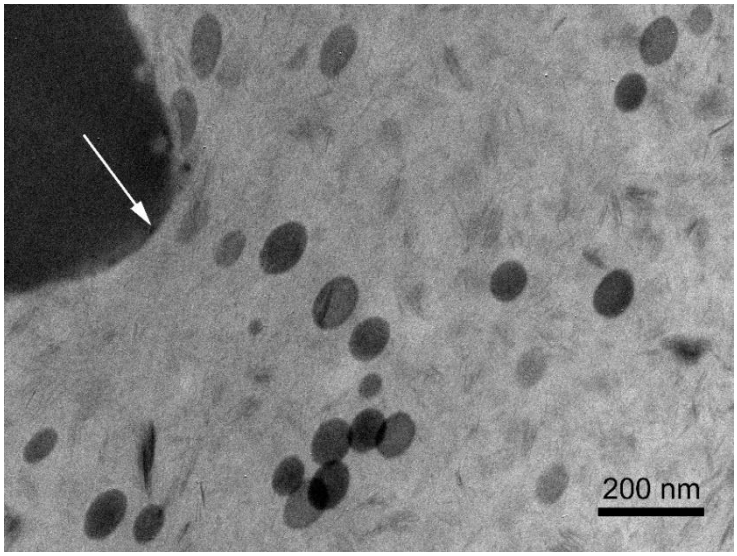

Figure 4-8. TEM of epoxy/α-ZrP-TBA/CSR nanocomposite in the plane stress region of the DN-4PB specimen. The arrow indicates the arrested crack tip.

It is generally agreed that not all epoxy resins can be toughened to by rubber modification.[183] Toughenability of epoxy resins is mostly related to the thermoset crosslinking density.[184] In the rubber-toughened epoxy systems, as the rubber cavitation mechanism has little effect in fracture energy dissipation, matrix shear banding is therefore the main energy dissipation process in the rubber-toughened epoxies.[149,185] Plastic deformation requires large-scale cooperative motions to form shear bands. Therefore, the mobility of polymer chains plays an important role in enhancing fracture toughness of rubber-toughened epoxy resins. Following this logic, toughening epoxy nanocomposites containing α-ZrP nanoplatelets should be more difficult as the presence of nanofiller will hinder the mobility of the surrounding molecules, thus limiting its ability to undergo plastic deformation. However, in the case of α-ZrP with monoamine as the surfactant, the crosslink density around the α-ZrP nanofiller is greatly reduced. The low crosslinking density network greatly improves the ductility and toughenability of the epoxy nanocomposites.[56] Unfortunately, a concurrent reduction in T_g occurs.

In the case of using α-ZrP-TBA as a catalytic curing agent, the relatively small size of TBA will not affect the epoxy crosslinking process as monoamine curing agent would. In addition, since the polymerization of epoxy monomers is initiated from the surface of α-ZrP, the strong covalent bonding of epoxy to α-ZrP may suppress molecular mobility and increases the T_g of the matrix. Consequently, the T_g of epoxy cured by α-ZrP-TBA is 30 °C higher than the epoxy nanocomposite with the same amount of α-ZrP addition but using a long chain monoamine as a surfactant.[56] As for the toughening of epoxy/α-ZrP-TBA, as stated earlier, it is surmised that the crosslink density in epoxy matrix would be

heterogeneous because of the concentrated TBA on α-ZrP surfaces. This postulation is supported by the fact that the tan δ peak at T_g for epoxy/α-ZrP-TBA is much broader than that of the neat epoxy. A self-curing epoxy nanocomposite containing 2 vol% of ZrP-TBA was also prepared. The DMA result is shown in Figure B-4. The T_g and rubbery plateau modulus of the epoxy/α-ZrP-TBA @ 2 vol% are much lower than the epoxy matrix containing 4 vol% of ZrP-TBA. This means that this epoxy is unlikely to be fully cured. Therefore, while ZrP-TBA can serve as a crosslinking agent for epoxy, its effectiveness only extends to the crosslinking of epoxy monomers in the vicinity of the nanoplatelets. This nonuniform crosslinking of epoxy network facilitates large-scale cooperative conformational arrangements of polymer backbones. Therefore, upon cavitation of CSR particles, the triaxial stress state at the crack tip is transformed into biaxial stress state to trigger large-scale matrix shear banding, which accounts for the substantial increase in fracture toughness. Additional work is still needed to further validate the above conjecture.

4.4. Conclusion

Novel epoxy nanocomposites based on TBA-exfoliated α-ZrP nanoplatelets as a catalytic curing agent have been prepared. TBA serves as a surfactant and curing catalyst by forming a phosphate anion pair on α-ZrP surface to initiate the polymerization of epoxy resins, and the α-ZrP nanoplatelets act as a reinforcement to improve the mechanical properties of epoxy. The incorporation of the α-ZrP-TBA nanoplatelets can greatly improve the Young's modulus due to the strong covalent bonding between the nanoplatelets and epoxy matrix. To overcome the brittleness nature of the epoxy/α-ZrP-TBA, CSR was introduced and found to be effective in improving the K_{IC} of the epoxy

nanocomposite. The main toughening mechanisms in epoxy/α-ZrP-TBA/CSR are rubber particle cavitation, followed by matrix shear banding. The hybrid epoxy/α-ZrP-TBA/CSR nanocomposites possess good potential as high-performance structural materials for aerospace and automotive applications.

5. EPOXY NANOCOMPOSITES CONTAINING ZEOLITIC IMIDAZOLATE FRAMEWORK-8[‡]

5.1. Introduction

Polymeric materials are commonly used in electronic packages because of their easy processability, low cost, good adhesive properties, low dielectric constant, etc. Nanofillers can be used to improve the properties of the polymer matrix. However, the biggest challenge in the fabrication of these nanocomposites is the low compatibility between the organic and inorganic components, which can result in agglomeration of nanofiller particles and significant compromise in device performance.[9]

Metal-organic framework (MOF) particles are a relatively new family of nanoporous materials[10] that have an ordered, well-defined porous structure and can be easily modified to become compatible with the hosting polymer matrix.[11] MOFs have been widely researched for applications in gas storage[186] and separation,[187] catalysis,[188] drug delivery,[189] sensors,[190] ion conductors,[191] etc. MOFs generally are more compatible with organic polymer matrices than other nanofillers such as silica, alumina, and carbon black, because the organic linkers can interact with polymers through molecular design.[192,193] MOFs prepared from imidazoles (zeolitic imidazolate frameworks or ZIFs) are a sub-family of MOFs,[194] exhibiting structures analogous to that of inorganic zeolites and possessing excellent chemical and thermal stability.[195] ZIF-8 is the most investigated

[‡] Reprinted with permission from "Epoxy Nanocomposites Containing Zeolitic Imidazolate Framework-8" by Liu, C., Mullins, M., Hawkins, S., Kotaki, M., & Sue, H. J., **2018**. ACS applied materials & interfaces, 10(1), 1250-1257, Copyright 2017 by American Chemical Society.

material in the ZIF family, prepared from zinc(II) salts and 2-methyl-1*H*-imidazole, with a sodalite topology(a pore aperture of 3.4 Å and a pore cavity of 11.6 Å).[196] ZIF-8 has been shown to be useful as a low-k material due to its low polarity and low density.[197] A promising application for ZIF materials is to use them as a modifier for polymer to reduce the dielectric constant and enhance mechanical properties.[198]

Herein, we demonstrate the use of ZIF-8 as a nanofiller with low dielectric constant[197] and excellent thermal and chemical stability to modify epoxy thermosets without compromising other properties.[199] Imidazoles are known to initiate epoxy curing.[200] Although the imidazole groups on the ZIF-8 surface are bound to zinc cations, it is anticipated that sufficient nucleophilicity would remain to cure epoxy resins. Prior work describes the dispersion of MOFs that are not capable of forming covalent bonds directly with the matrix. For example, MOF-5 has been used to toughening epoxy,[201] and to improve corrosion resistant property of epoxy coating.[202] the advantage of our approach would be that covalent bonding between ZIF-8 and epoxy matrix in our case would ensure good dispersion and prevent aggregation. Furthermore, the use of a hardener can be avoided, although this depends on the concentration of MOF desired.

The present work describes the utilization of ZIF-8 to initiate crosslinking of epoxy resins and its use as a modifier to prepare polymer nanocomposites for low-k dielectrics applications. It will be shown that the epoxy/ZIF-8 nanocomposite thin films possess a dielectric constant much lower than that of neat epoxy, excellent tensile properties, and low moisture absorption. The present study offers a new perspective on the design of

MOFs as polymer modifiers and the fabrication of high performance multifunctional inorganic-organic nanocomposites for wide arrays of engineering applications.

5.2. Experimental section

5.2.1. Materials

Zinc nitrate hexahydrate (Sigma-Aldrich) and 2-methyl-1H-imidazole (2MI) (Alfa Aesar) were used for the synthesis of ZIF-8 (Figure 5-1). Commercially available bisphenol A diglycidyl ether (D.E.R.TM 383) was kindly donated by Olin Corporation. Methyl ethyl ketone (MEK) was purchased from Fisher Scientific.

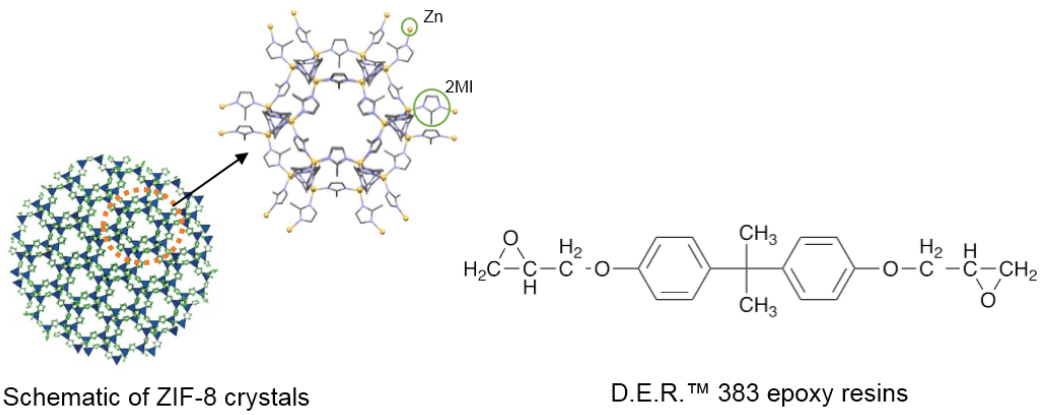

Figure 5-1. Chemical structure of the ZIF-8 nanocrystal and DGEBA epoxy resins.

5.2.2. Synthesis of ZIF-8 nanocrystals

The ZIF-8 particles were synthesized according to the literature report.[136] 10 mmol (3 g) of $Zn(NO_3)_2 \cdot 6H_2O$ was added into 100 mL of methanol to form solution A. 80 mmol (6.6 g) of 2-methyl-1*H*-imidazole was added into 100 mL of methanol to form solution B. The two kinds of solution were mixed and stirred for 1 h at room temperature. The

resulting ZIF-8 particles were collected by centrifugation, subsequently washed with methanol twice and with MEK once. The obtained ZIF-8 was re-dispersed as colloids in MEK for further preparation of epoxy nanocomposites.

5.2.3. Preparation of epoxy/ZIF-8 nanocomposites

The as-synthesized ZIF-8 solution in MEK was sonicated for 0.5 h to prevent particle aggregation, and then mixed with epoxy resins in predetermined weight ratios and mechanically stirred for 1 h. Subsequently, MEK solvent was removed from the mixture by rotary evaporation. The resulting epoxy/ZIF-8 mixtures containing ZIF-8 at 6, 13, and 25 vol%, respectively, were put in a vacuum oven overnight (ca. 8 h) at room temperature, followed by heating at 100 °C for 1 h. Then, they were cured in a hot press at 200 °C for 3 h. The corresponding molar ratios of 2-methyl imidazole to epoxy resin in the epoxy/ZIF-8 nanocomposites containing 6, 13, and 25 vol% of ZIF-8 are 8%, 16%, and 32%, respectively. Neat epoxy cured with 2-methyl imidazole as a curing agent was also prepared using the same procedure as a control. The molar ratio of 2-methyl imidazole to epoxy resin was chosen at 16%.

5.2.4. Characterization

Scanning electron microscopy (SEM) was conducted on a JEOL JSM-7500F Field Emission-SEM. Wide angle X-ray diffraction (XRD) was performed using a Bruker D8 X-ray diffractometer. Optical micrographs (OM) were performed with an Olympus BX60 optical microscope. The morphology was studied using transmission electron microscopy (TEM). A microtome (Ultracut E) and a Micro Star diamond knife were used to prepare ultrathin sections (ca. 100 nm in thickness) which were collected on carbon-coated copper

grids. Thermogravimetric analysis (TGA) was performed with a TA Instruments Q500 thermogravimetric analyzer. Samples were pre-conditioned for 60 min isotherm at 120 °C before increasing temperature to 800 °C at 10 °C/min under a 20 mL/min air flow. Differential scanning calorimetry (DSC) was performed using TA Q20 at a heating rate of 10 ^{o}C/min.

An RSA-G2 (TA Instruments) with a tensile fixture was used for tensile tests and dynamic mechanical analysis. The tests were performed at 25 °C on rectangular samples (3 mm × 0.01 mm cross section and about 5 mm length) with a crosshead speed of 10 mm/min. A strain amplitude of 0.05% and a frequency of 1 Hz was used for dynamic mechanical analyses (DMA). A heating rate of 3 °C/min from room temperature to 200 °C was used.

Water absorption of epoxy nanocomposites was measured according to ASTM D570. The specimens were removed from the water bath at regular intervals and weighed. The percentage gain (M_t) was determined by Equation:

$$M_t = \frac{W_{wet} - W_{dry}}{W_{dry}} \times 100\ (\%) \qquad (5\text{-}1)$$

5.3. Results and discussion

5.3.1. Characterization of ZIF-8 nanocrystals and the epoxy nanocomposites

The XRD patterns of the as-synthesized ZIF-8 nanocrystals are shown in Figure 5-2a, which are consistent with the simulated result from the literature.[199] The SEM image of Figure 5-2b shows that the nanocrystals exhibit a hexagonal faceted shape, which is commonly reported in the literature.[203,204] The average size of the nanocrystals is about 50 nm.

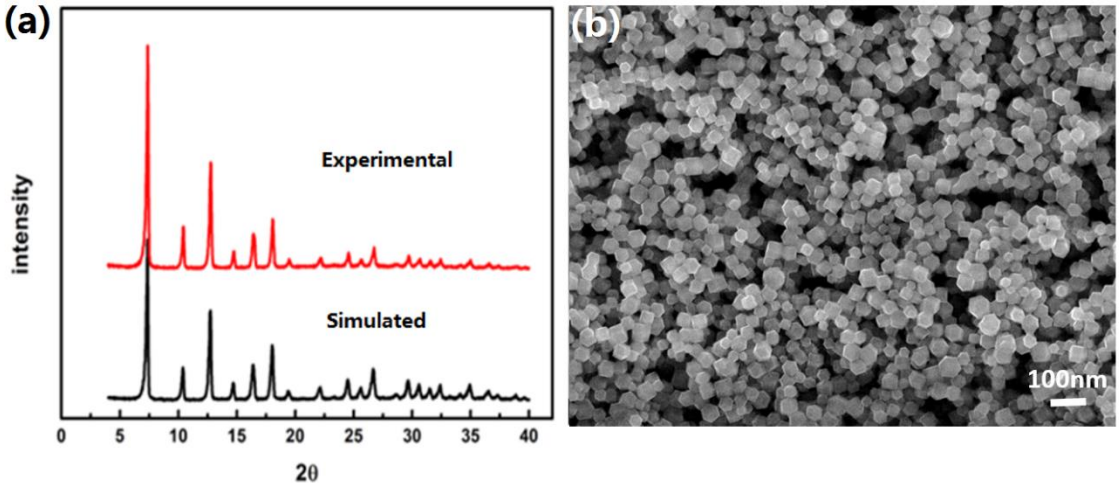

Figure 5-2. (a) XRD patterns of ZIF-8 nanocrystals. (b) SEM images of ZIF-8 nanocrystals.

Figure 5-3 shows the procedure for preparation of epoxy/ZIF-8 nanocomposites. The turbid suspension of the mixture of ZIF-8 and epoxy resins turned into a clear yellow gel after postcure, indicating the separation of the originally agglomerated ZIF-8 nanocrystals (Figure C-1). OM reveal this transition (Figure C-2). This phenomenon may be caused by the ring-opening reaction of the epoxy and the formation of covalent bonds that lead to exfoliation of the aggregated ZIF-8 nanocrystals. Figure C-3 show the XRD patterns of neat epoxy and epoxy/ZIF-8 nanocomposites with various loading. With the increasing loading of ZIF-8 nanoparticles, the relative intensity of the characteristic peaks of ZIF-8 gradually increases. The patterns of the nanocomposites show the characteristic peaks of ZIF-8 crystals, which indicates that the crystalline structure of ZIF-8 nanocrystals is retained in the nanocomposites

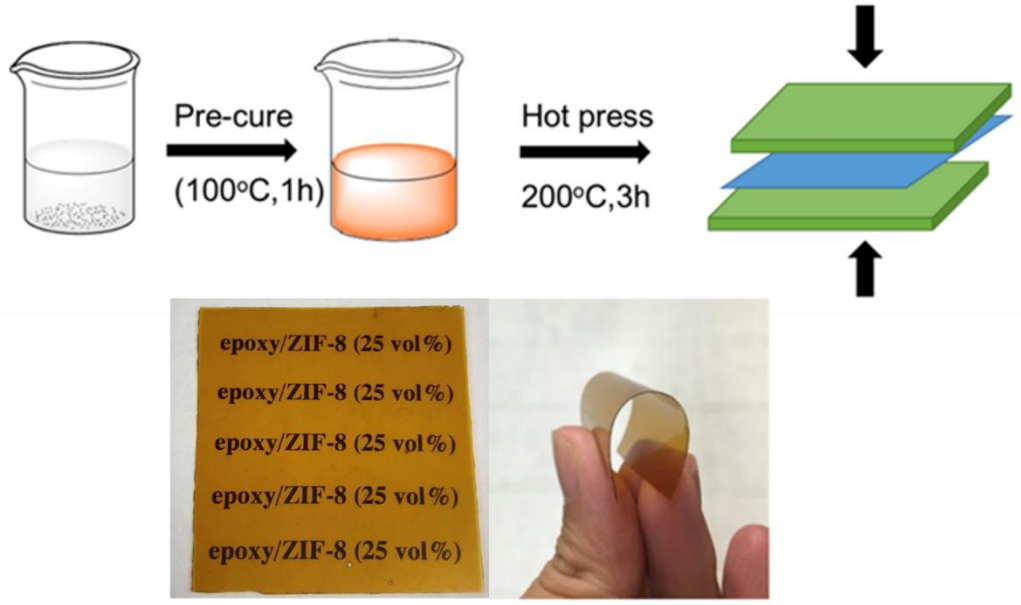

Figure 5-3. Procedure for preparation of Epoxy/ZIF-8 nanocomposites. An optical image of the nanocomposite containing 25 vol% of ZIF-8 is also shown.

5.3.2. Curing mechanism

The imidazole groups on the surface of ZIF-8 are likely to initiate epoxy ring-opening polymerization as shown in Figure 5-4. This mechanism is well-precedented for the reaction between epoxide and imidazole compounds.[163,205]

Figure 5-5 shows the curing reactions of epoxy with 2-methyl imidazole and ZIF-8 during non-isothermal DSC scan at 10 °C/min, respectively. The molar ratio of 2-methyl imidazole is both 16% in these two systems. The exothermic peak for the epoxy/ZIF-8 mixture appears at 215 °C, while the peak for the mixture of epoxy and 2-methyl imidazole is at 110 °C. The imidazoles in ZIF-8 are considerably less reactive, probably due to the reduced basicity of the imidazole nitrogen because of electron-withdrawing by the cationic zinc in ZIF-8.

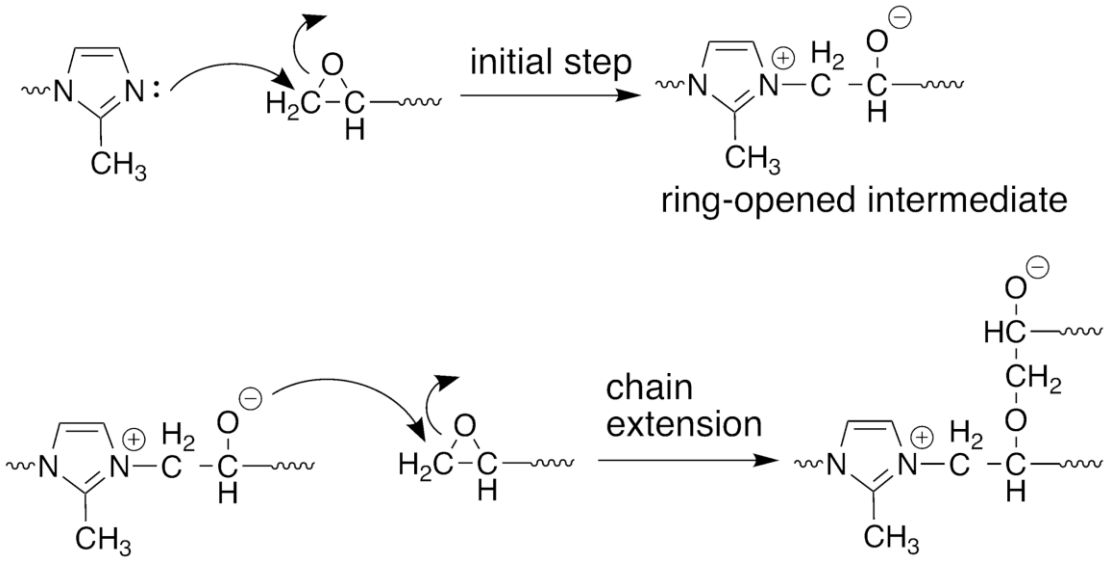

Figure 5-4. Schematic mechanisms of the reaction between ZIF-8 and epoxy resin.

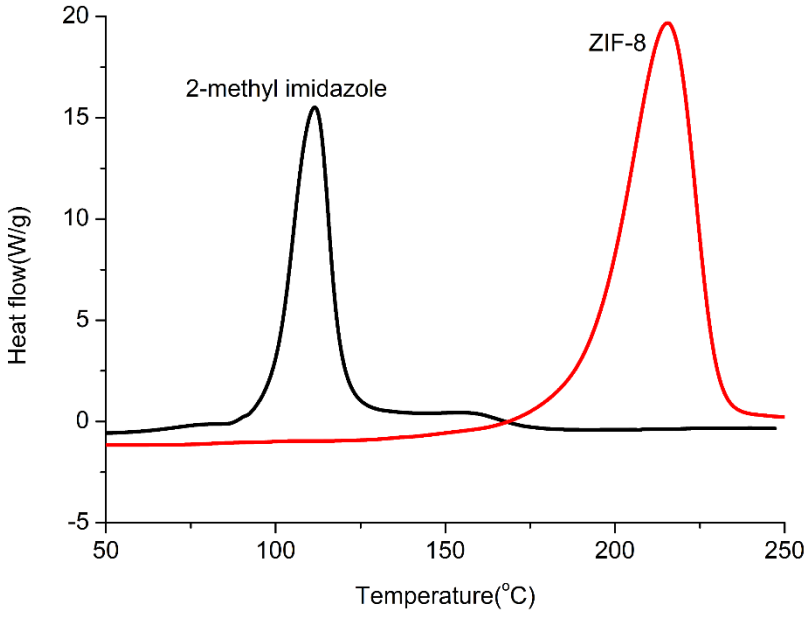

Figure 5-5. Non-isothermal (10 °C/min) DSC scans of epoxy cured by 2-methyl imidazole and ZIF-8 at the same molar ratio (16%) of 2-methyl imidazole, respectively.

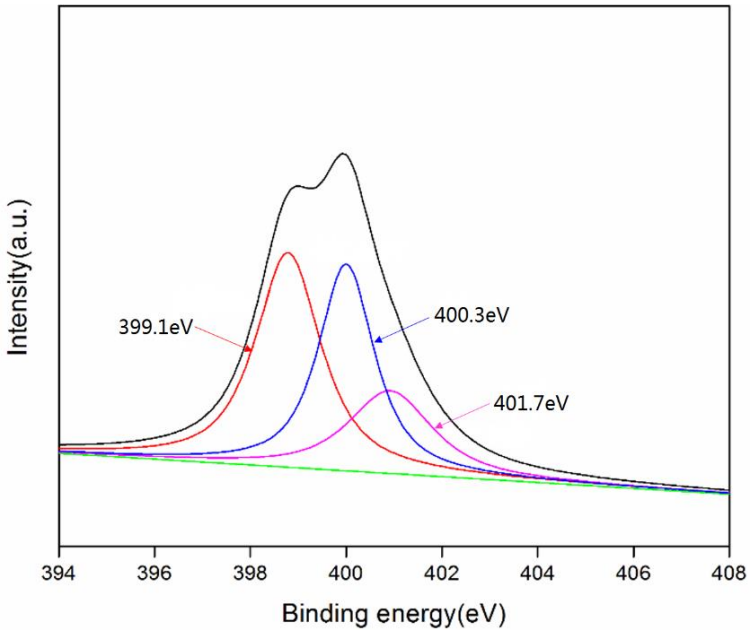

Figure 5-6. XPS survey spectra (N1s) of the epoxy/ZIF-8 (25 vol%).

In order to demonstrate that ZIF-8 and the epoxy resin are covalently bonded, the cured systems were studied using XPS and FTIR. Figure 5-6 shows the core level N 1s spectrum of epoxy/ZIF-8 (25 vol%) with three distinct peaks at 399.1 eV, 400.3 eV, and 401.7 eV. The two nitrogen atoms in the 2-methyl imidazole are distinct. The first two peaks arise from 2-methyl imidazole from ZIF-8 nanoparticles that do not react with the epoxide group.[206] The third peak at 401.7 eV is attributed to the reacted nitrogen through which the imidazole ring is attached to epoxide group. The results of FTIR are shown in Figure C-4 also provide evidence for covalent bonding. DSC measurement was used to confirm the complete curing of the epoxy/ZIF-8 nanocomposites (Figure C-5).

5.3.3. Thermal stability

Figure 5-7 reveals the TGA curves of the neat epoxy, ZIF-8 nanoparticles and epoxy/ZIF-8 nanocomposites. The decomposition profiles of neat epoxy and epoxy/ZIF-8 nanocomposites have similar decomposition profiles with degradation occurring in two stages. Some prior reports[207,208] suggest that the introduction of nanoparticles causes reduced thermal stability due to increases in free volume fractions in the polymer nanocomposites. The two onset decomposition temperatures (T_{d1} and T_{d2}), as well as the temperature at 5% weight loss ($T_{5\%}$) of the nanocomposites are similar to those of neat epoxy (Table C-2). It can be seen that the total weight loss of the first degradation process decreases with the increasing loading of ZIF-8 nanocrystals, which can be attributed to the high thermal stability of ZIF-8 nanocrystals and their covalent bonding to the epoxy matrix which hinders escape of decomposed low molecular species during TGA measurements.

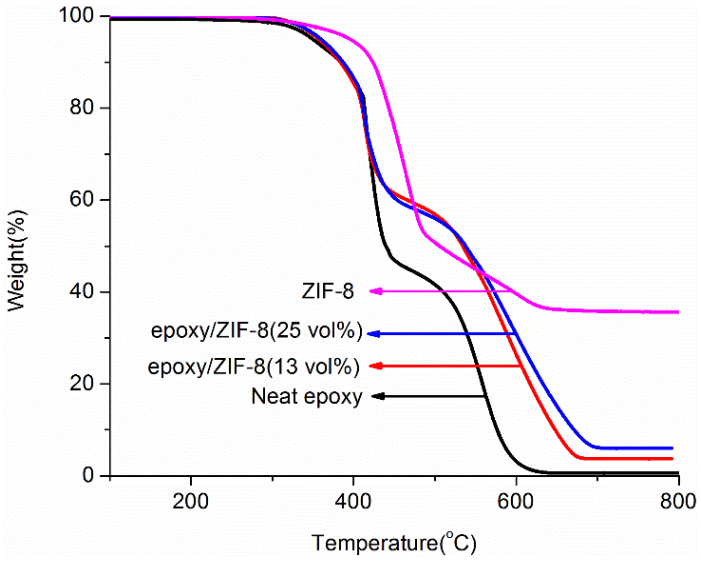

Figure 5-7. TGA curves of the neat epoxy, ZIF-8 nanocrystals and epoxy/ZIF-8 nanocomposites measured in air.

5.3.4. Morphology of epoxy/ZIF-8 nanocomposites

Transparent and flexible epoxy/ZIF-8 thin films were prepared by curing them in a hot press at 200 °C for 3 h (Figure 5-3). The morphology of the nanocomposite thin films was observed using TEM. Figure 5-8 shows the TEM images of the epoxy/ZIF-8 thin films. The ZIF-8 nanocrystals appear dark in the images while the light background is the epoxy matrix. The white circular rings were artifacts due to diamond knife cutting during the preparation of ultrathin sections. In addition, the electron beam also induces matrix/particle debonding. TEM micrographs reveal that the ZIF-8 is individually dispersed in the epoxy matrix. All nanoparticles are surrounded by epoxy matrix. Even with 25 vol% loading, there is likely no direct particle-to-particle contact observed. It appears that the covalent bonding of imidazole to epoxy resins prevents aggregation of ZIF-8 nanoparticles.

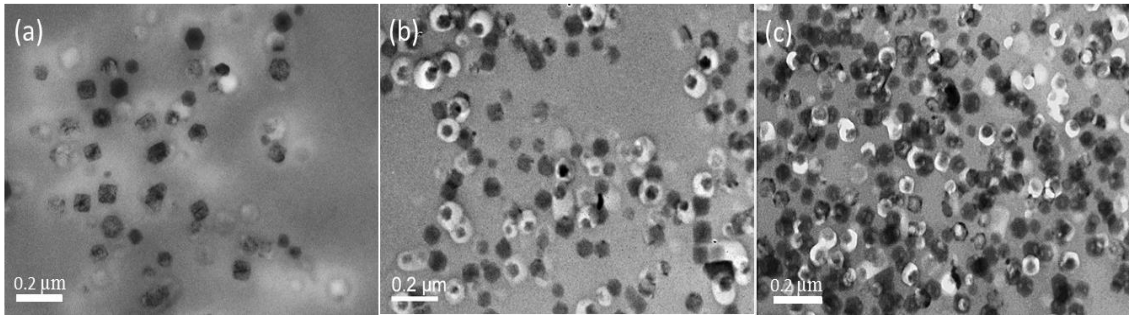

Figure 5-8. TEM images of cross-section of epoxy/ZIF-8 thin films at (a) 6 vol% loading, (b) 13 vol% loading, and (c) 25 vol% loading.

5.3.5. DMA Study

DMA was performed in tensile film geometry to determine the effect of adding ZIF-8 nanoparticles on dynamic mechanical behavior. Tan δ was taken as the ratio of *E''/E'*. The DMA results are shown in Figure 5-9, and the storage modulus and T_g values are summarized in Table 5-1.

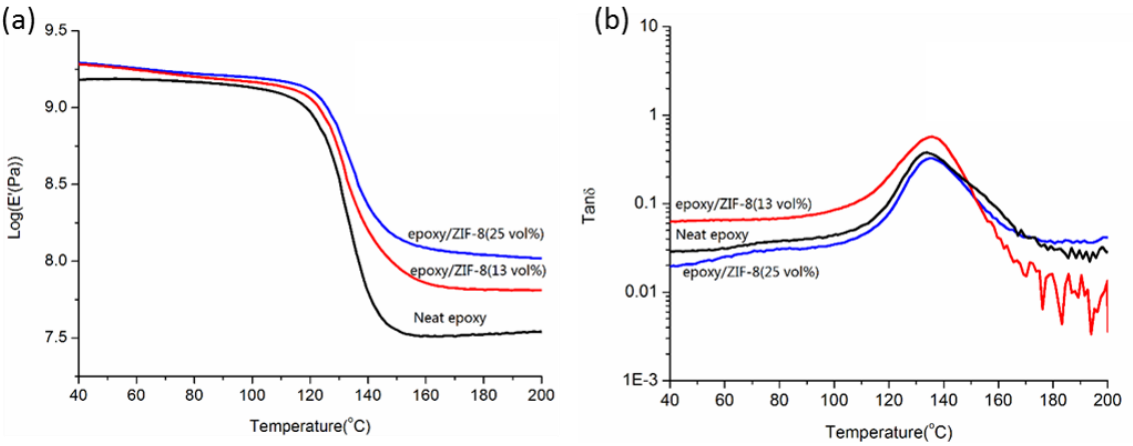

Figure 5-9. DMA plots of epoxy/ZIF-8 nanocomposites: (a) Storage modulus as a function of temperature and (b) Tan δ as a function of temperature.

E' as a function of the temperature for the neat epoxy and epoxy nanocomposites is shown in Figure 5-9a. The nanocomposite containing 25 vol% of ZIF-8 nanocrystals exhibits over 30% and 300% increase in *E'* against the neat epoxy at 40 °C and 160 °C, respectively. Note that the storage modulus is increased much more significantly at temperatures above T_g than at temperatures below T_g. This has been observed in other polymer nanocomposites.[56,159,172] This difference in modulus enhancement at above and below T_g has been postulated to be due to the molecular dynamics of epoxy chains at above

and below T_g are drastically different and shows more effective retardation of molecular motion at above T_g.[174,175] Moreover, it is noted that the nanocomposites exhibit similar T_g with neat epoxy cured with 2MI. This suggests that the introduction of ZIF-8 does not compromise the thermal properties of epoxy. Meanwhile, the nanocomposites should possess a similar crosslinking structure with neat epoxy cured by 2MI. Therefore, the significant increase in *E'* and invariant T_g demonstrate the effectiveness of ZIF-8 as a reinforcing agent and a curing agent as well.

Table 5-1. Storage modulus and T_g values of neat epoxy and epoxy/ZIF-8 nanocomposites.

Films	*E'* (GPa) at 40 °C	*E'* (MPa) at rubbery plateau	T_g (°C)
Neat epoxy	1.59	33.8	133 °C
epoxy/ZIF-8 (13 vol%)	1.95	72.4	135 °C
epoxy/ZIF-8 (25 vol%)	2.09	112.0	135 °C

5.3.6. Tensile behavior of neat epoxy and epoxy/ZIF-8 nanocomposites

The engineering tensile stress-strain curves of the neat epoxy and the nanocomposites are presented in Figure 5-10. The data of tensile strength, maximum elongation and Young's modulus with ZIF-8 loading is provided in Table C-3. As ZIF-8 loading increases to 13 and 25 vol%, the tensile strength of the nanocomposites maintains the comparable level with that of the neat epoxy, even though the elongation is decreased

by 35 and 40%, respectively. The decrease in elongation at break is possibly due to the low molecular mobility of the epoxy network structure caused by the existing of the immobile and rigid ZIF-8 nanoparticles, as evidenced by the DMA study.

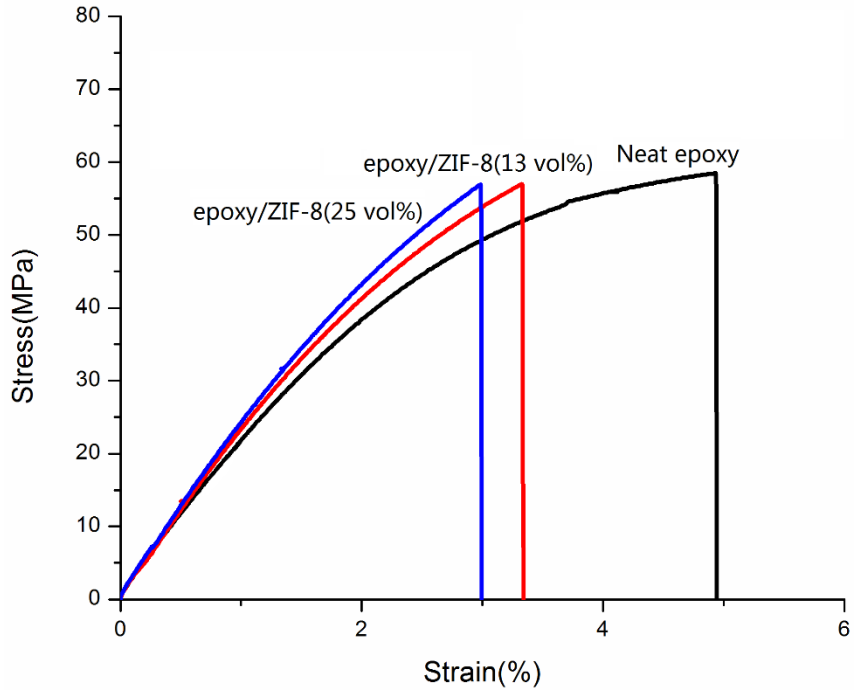

Figure 5-10. Tensile engineering stress–strain curves obtained at 25 °C for neat epoxy and nanocomposite thin films.

The Young's modulus of the nanocomposites increases from 2.33 to 2.82 GPa as the loading increases from 0 to 25 vol %. The change of elongation-to-break with the increasing loading of nanoparticles shows opposite trend as compared to the variation of Young's modulus. These results reveal the enhanced stiffness and decreased ductility of the nanocomposites. The stiffness/toughness balance can be observed in most epoxy nanocomposites.[157,176-180] We have also prepared the epoxy/2MI/ZIF-8 (25 vol%)

nanocomposites by adding additional 2MI as the curing agent. The amount of 2MI is 16 mol%. Considering the higher reactivity of free 2MI than the 2MI attached to ZIF-8, epoxy monomers will predominantly react with the free 2MI rather than ZIF-8 during curing reaction. As a result, covalent bonding cannot form between ZIF-8 and epoxy. Obvious aggregation was formed in the composite thin film and this sample exhibits reduced tensile strength than the epoxy/ZIF-8 nanocomposites. Also, the Young's modulus and elongation at break were decreased, which can be attributed to the aggregation of the nanoparticles (Figure C-8).

It is well-known that increases in porosity usually result in decreased mechanical properties for porous materials.[209] But the mechanical strength of epoxy/ZIF-8 nanocomposites is not compromised even when the particle loading is as high as 25 vol%. This can be due to the high rigidity of ZIF-8[210,211] which negates the effect of the presence of cavity inside the ZIF-8 crystal, as well as the strong bonding between the nanoparticles and polymer.

5.3.7. Dielectric properties of epoxy/ZIF-8 nanocomposites

The introduction of porous ZIF-8 nanocrystals can increase the porosity of the polymer matrix, resulting in a decreased dielectric constant for the nanocomposites. The dielectric properties of the pure epoxy cured with 2MI were compared with nanocomposite films with various loadings at room temperature. Figure 5-11 reveals that dielectric constants of the nanocomposites as a function of frequency. Neat epoxy has a relatively high dielectric constant of 3.9 at 100 kHz, while the dielectric constant of the nanocomposite samples gradually decreases with the increasing volume fracture of ZIF-8

nanoparticles. As the ZIF-8 loading is increased to 25 vol%, the dielectric constant decreases to 3.2 compared to the neat epoxy at 100 kHz. The dielectric loss of both samples also shows the same trend with dielectric constant (Figure C-9).

This reduction in dielectric constant of the nanocomposite arises from the considerably lower dielectric constant of ZIF-8 compared to the neat epoxy. As discussed above, imidazole groups on the surface of ZIF-8 facilitated good particle dispersion in the epoxy matrix.

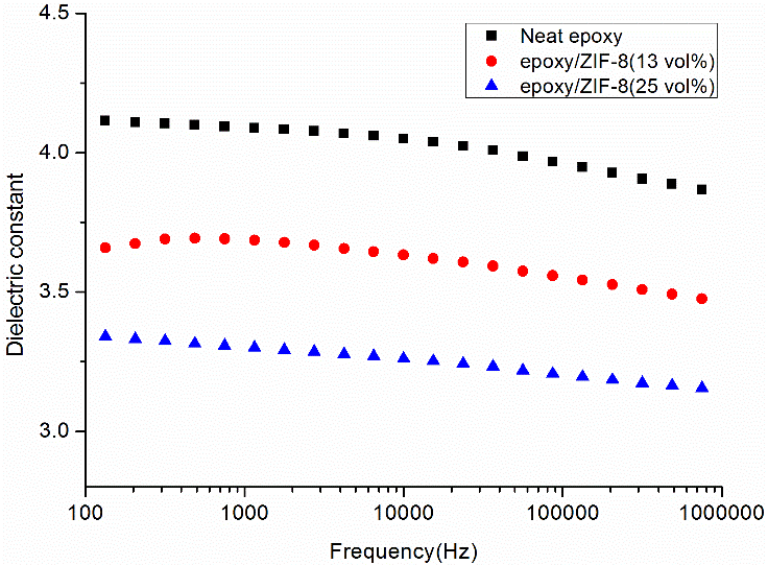

Figure 5-11. Dielectric constant of neat epoxy and epoxy/ZIF-8 nanocomposites as the function of frequency.

The dielectric behaviors of composite materials can be explained by many theoretical models.[212,213] One of the simplest models is the Maxwell-Garnett model, which is based on the linearity assumption between effective dielectric constant and volume

fraction.[214] This model is valid for a dielectric material containing a dilute conductive phase below the percolation threshold. Figure 5-12 reveals experimental and theoretical dielectric constants of the ZIF-8 and epoxy nanocomposites as a function of filler volume fraction at room temperature and 100 kHz. The theoretical values were predicted by the Maxwell–Garnett model:

$$\varepsilon_{eff} = \varepsilon_p \frac{2\varepsilon_p + \varepsilon_c + 2f(\varepsilon_c - \varepsilon_p)}{2\varepsilon_p + \varepsilon_c - f(\varepsilon_c - \varepsilon_p)} \quad (5\text{-}2)$$

where f is the volume fraction of fillers, and ε_{eff}, ε_p and ε_c donate the dielectric constants of the nanocomposites, epoxy and ZIF-8, respectively. It can be seen that the experimental dielectric constant is in agreement with those given by the Maxwell–Garnett model.[215] The volume fraction was calculated based on the densities of ZIF-8 and epoxy which can be found from the supporting information. When 36 vol% of ZIF-8 is incorporated in epoxy, aggregation of nanoparticles becomes evident, possibly due to the intimate contacts between ZIF-8 nanoparticles which leads to stronger van der Waals forces between the particles and causes aggregation (Figure C-7). Consequently, the result deviates slightly from the theory.

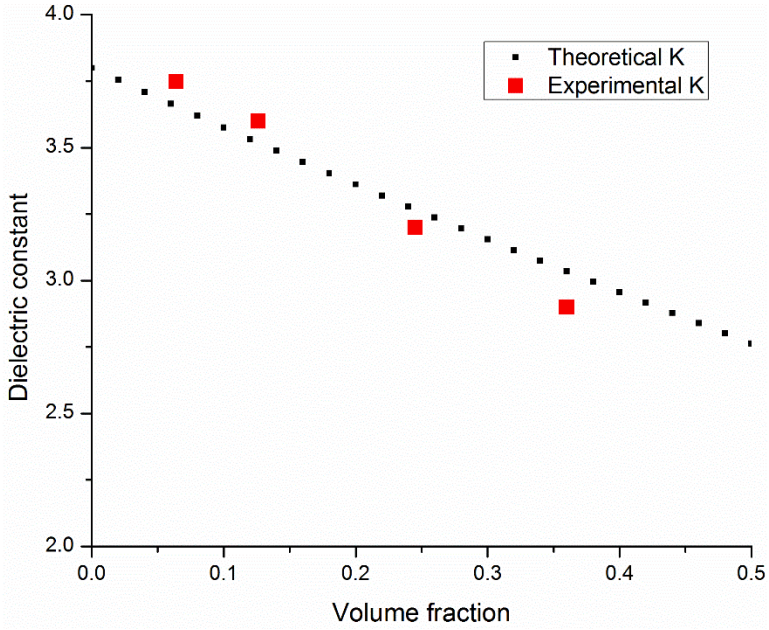

Figure 5-12. Dielectric constant of ZIF-8 and epoxy nanocomposites as a function of volume fraction.

5.3.8. Moisture absorption

Water, which has a k value of 80, can have significant deleterious effects on dielectric properties and reliability.[216] Figure 5-13 shows the water absorption of epoxy and epoxy/ZIF-8 nanocomposites. Saturation was reached for all epoxy samples after 8 days. The water absorption of epoxy at saturation (1.25 wt%) is higher than epoxy/ZIF-8 nanocomposites (0.95 wt%). Super-hydrophobicity of ZIF-8[217,218] with low polarity in epoxy matrix reduces the penetration and absorption of water in the nanocomposites. The hydrophobic nature of ZIF-8 in epoxy is attractive for application in low-k dielectrics.

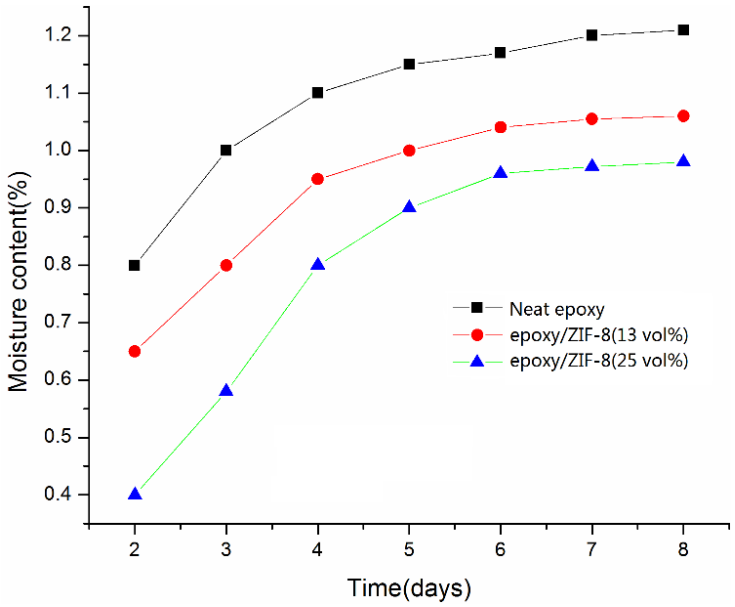

Figure 5-13. Water uptake for immersed epoxy, ZIF-8 and epoxy nanocomposite.

Herein, epoxy/ZIF-8 nanocomposites thin films were prepared to demonstrate the effectiveness of MOF as a curing agent as well as a low-k additive. It has been shown that the Epoxy/ZIP-8 nanocomposite thin films possess not only much lower dielectric constant than neat epoxy but also excellent tensile properties and lower moisture uptake. To the best of our knowledge, the present work is the first to utilize MOF to initiate crosslinking of epoxy resins. The covalent interface in epoxy/ZIF-8 nanocomposites improved the dispersion of ZIF-8 nanoparticles and also enhanced the tensile properties of the nanocomposites. In addition, as a result of low polarizability, high porosity and hydrophobicity of ZIF-8, ZIF-8 type of MOFs are good candidates as a modifier in preparation of polymer nanocomposites for low-k dielectrics applications. Moreover, compared with traditional porous materials (such as porous silica or porous carbon), the mechanical properties of MOF-polymer nanocomposites are not compromised even at a

high loading (25 vol%), which can be contributed to the high rigidity of MOFs materials and covalent bonding at the interface. Overall, the present study may provide a new perspective for the design of MOF and preparation of high-performance polymer nanocomposites in diverse applications.

5.4. Conclusion

Epoxy/ZIF-8 nanocomposites, with filler contents up to 25 vol%, can easily be processed. The imidazole groups in ZIF-8 frameworks serve to cure epoxy. As a result of the covalent bonds that form, the interfacial bonding between ZIF-8 and epoxy matrix is strong, which helps to increase the Young's modulus by 20%. Furthermore, because of the intrinsically porous and hydrophobic nature of ZIF-8, nanocomposites show lower dielectric constant and moisture uptake, which makes them excellent candidates as low-k dielectrics. ZIF-8 nanoparticles are well dispersed in the epoxy matrix without surface modification or addition of surfactant. The simple process can be easily scaled up to produce nanocomposites containing metal organic frameworks. This work can be readily extended to other MOF-containing polymer nanocomposites by functionalization of MOF to the chemical nature of the polymer matrix.

6. HIGH DIELECTRIC CONSTANT EPOXY NANOCOMPOSITES BASED ON METAL-ORGANIC FRAMEWORKS DECORATED MULTI-WALLED CARBON NANOTUBES[§]

6.1. Introduction

Polymers play an important role in energy harvesting and storage devices due to their excellent properties against ceramic and metallic materials, such as high breakdown strength, mechanical flexibility, low density, ease of processing and low cost.[219-221] Functional polymer nanocomposites are attracting interest in an increasing number of applications, including polymer-based dielectric capacitors[222,223] which are widely employed in the areas of artificial muscles,[224] film capacitors,[225] organic field-effect transistors,[87] invertors,[88] electro-optics,[89] sensors,[90] and energy storage devices.[92] Incorporation of electrically conductive materials, such as carbon nanotubes (CNTs), into polymers, is a promising approach to effectively increase the dielectric constant (k) of the polymer nanocomposites due to their high conductivity and surface area.[113,226,227] Two neighboring non-contact multi-walled CNTs (MWCNTs) in the polymer matrix can be considered as electrodes, and the polymers in between are nanodielectrics, which form the so-called "nanocapacitors".[228,229] In each nanocapacitor, charges are allowed to

[§] Adapted with permission from "High Dielectric Constant Epoxy Nanocomposites Based on Metal-Organic Frameworks Decorated Multi-Walled Carbon Nanotubes" by Liu, C., Zhang, T., Daneshvar, F., Feng, S., Zhu, Z., Kotaki, M., Mullins, M., & Sue, H. J., submitted for publication. Unpublished work copyright by 2020 Elsevier Ltd.

accumulate and polarize at CNT-polymer interfaces upon an applied external electric field, which refers to as the Maxwell-Wagner-Sillars interfacial polarization.[230]

However, the main problem caused by CNT-based dielectric nanocomposites is poor dispersion of CNT and lack of strong bonding between polymer matrix and CNTs.[231] Severely aggregated CNTs not only compromise the mechanical integrity of the hosting polymer but also create local conductive pathways, leading to high dielectric loss and/or premature electrical breakdown.[230] Decorating CNT surfaces with a functional electrical barrier layer through suitable modification strategies can be an effective approach to improve the dispersion of CNTs and manipulate the interfacial region between CNTs and polymer matrix.[24,75]

Wrapping or grafting of low molecular weight molecules having a similar chemical structure as the hosting polymer matrix onto CNT surfaces has been shown to be an effective way to improve CNT dispersion and interfacial strength.[110-112,230,232,233]. However, usually a large amount of such low molecular weight molecules will be needed to achieve good dispersion and may lead to compromises in thermal stability, glass transition temperature, and coefficient of thermal expansion (CTE), which are undesirable for dielectric applications. To avoid those drawbacks, some inorganic nanoparticles, such as silica and titania,[115,117] have been used to decorate CNT surfaces as an insulating layer. Unfortunately, these decorated CNTs cannot be well dispersed due to their inadequate compatibility with the hosting polymer matrix. In addition, weak adhesion at the interface between inorganic nanoparticles and the polymer matrix may cause significant interfacial relaxation, which leads to dielectric loss. Therefore, new interfacial design strategies that

can minimize the dielectric loss without compromising the mechanical properties and CTE are still needed.

Metal-organic frameworks (MOFs) are porous materials composed of metal ions and organic linkers.[234] MOFs have been used to functionalize nanomaterials through coordination bonding, such as MWCNT,[235] graphene,[236] and metal oxide nanoparticle,[237,238] to improve their electrical properties for electronic applications. In addition, MOFs can exhibit high compatibility with polymer matrices due to their exposed organic linkers on the surfaces.[239] Compared with conventional surface modifiers, such as small molecules and inorganic nanoparticles, MOF combines the advantages of its high porosity, rigidity, and good compatibility with a polymer matrix. Therefore, MOF is a good modifier for the preparation of high-performance polymer nanocomposites. Previously, it has been shown that Zeolitic imidazolate framework-8 (ZIF-8), prepared from zinc (II) salts and 2-methyl-imidazole (2MI), can be utilized as an epoxy curing agent to initiate anionic polymerization of epoxies.[173] ZIF-8 can also be in-situ grown onto the surface of MWCNTs and form nanohybrids with controlled morphological characteristics to possess optimal electric properties.[240-243]

Herein, ZIF-8 was utilized as a multi-functional modifier to decorate MWCNT surfaces and disperse them in the epoxy matrix for high-performance dielectric applications. The imidazole-based MOFs can initiate ring-opening polymerization of epoxy resins without a need for further addition of curing agent or catalyst,[205] which can not only achieve good dispersion and bonding of MWCNTs but also greatly enhance dielectric properties. The strong covalent bonding between ZIF-8 and the epoxy matrix is

expected to reduce dielectric loss and CTE, while enhancing the tensile properties of epoxy. The current study presents the first example of using MOF to modify the MWCNT interface for polymer nanocomposites with attractive dielectric properties. The role of MOF morphological structures on MWCNT for improvement of the dielectric and physical and mechanical properties of polymers is discussed.

6.2. Experimental section

6.2.1. Materials

MWCNTs were donated by Arkema with reported inner and outer diameters of 2–6 nm and 10–15 nm, respectively, and length of 0.1–10 μm. Zinc acetate dihydrate and potassium hydroxide (KOH) were purchased from Sigma-Aldrich. Acetone and methanol (MeOH) were purchased from Macron Fine Chemicals and Sigma-Aldrich and used as received. Zinc nitrate hexahydrate (Alfa Aesar) and 2-methylimidazole (2MI) (Sigma-Aldrich) were used for the synthesis of ZIF-8. Commercially available diglycidyl ether of bisphenol F (D.E.R.^{TM} 354) was donated by DOW Chemical. All chemicals were used as received without further purification.

6.2.2. Pretreatment of MWCNT

In a 30 mL mixture of sulfuric acid and nitric acid at a 3:1 v/v ratio, 100 mg of MWCNTs were added. Then, the solution was ultrasonicated for 2 h at room temperature and for another 1 h after the addition of 190 mL deionized water (DI-H_2O). The oxidized MWCNTs were collected by filtration, washed four times with DI-H_2O, and then washed an additional four times with MeOH. The oxidized MWCNTs were dispersed in MeOH at a concentration of ~1 mg/mL for further synthesis of ZnO decorated MWCNT.

6.2.3. Synthesis of MWCNT-ZIF-8-D

Pretreated 35 mg of oxidized MWCNTs and 210 mg of PVP were added in 30 mL of methanol. After the MWCNTs were uniformly dispersed with the assistance of ultrasonication for 0.5 h, the resultant suspension was mixed with 900 mg of $Zn(NO_3)_2$ $6H_2O$. Then, the mixture was stirred for 1 h at room temperature to form a black suspension A. Subsequently, 984 mg of 2-methylimidazole was dissolved in 10 mL of methanol to form a clear solution B, followed by slow addition to suspension A under stirring for 30 min. After it was kept unperturbed for 4 h, the obtained precipitate (i.e., MWCNT-ZIF-8-D) was collected by filtration and washed thoroughly with methanol 3 times to remove the surfactant and the residual ions.

6.2.4. Synthesis of MWCNT-ZnO

The preparation of ZnO-decorated MWCNT was conducted as described previously.[244] KOH (1 g) was added into oxidized MWCNTs (160 mg) suspension in methanol and sonicated for about 5 min. Next, zinc acetate dihydrate (1.96 g) solution in methanol (10 mL) was added. The system was heated to 60 °C and refluxed for 2 h. After the reaction, the MWCNT-ZnO was filtered and rinsed four times with MeOH and then resuspended in methanol for further preparation of polymer nanocomposites.

6.2.5. Synthesis of MWCNT-ZIF-8-C

MWCNT-ZnO suspension (~1 mg/mL) was sonicated for 15 min. Then, a suitable amount (molar ratio of Zn and 2MI = 1:4) of 2MI was dissolved in methanol and was slowly added into MWCNT-ZnO suspension within 2 min under stirring. The MWCNT-

ZIF-8-C products were stirred for another 4 h and then were filtered and washed at least three times with methanol.

6.2.6. Preparation of epoxy nanocomposites

The fabrication of epoxy nanocomposite thin films is described as follows. Initially, DGEBF was dissolved in acetone with the assistance of ultrasonication. MWCNT or MWCNT-ZIF-8 suspension in methanol was added subsequently and the mixture was then sonicated for 15 min. The excessive solvent was removed by rotary evaporation at 60 °C for 15 min. Afterward, the viscous mixture was degassed in vacuo at 80 °C for 2 h to ensure the complete evaporation of residue solvent. The mixture was then heated at 121 °C for 45 min to afford sufficient viscosity for thin film preparation. Subsequently, the Elcometer 4340 Motorised Film Applicator was used to cast the resin solution to a thin film with a thickness of ~100 μm. The film was then cured at 120 °C for 2 h and post-cured at 180 °C for 3 h, followed by 200 °C for 2 h. The MWCNT content in all the polymer nanocomposites is controlled at 1.5 wt%.

6.2.7. Characterization

Thermogravimetric analysis (TGA) was carried out on a TGA Q500 (TA Instruments) in an air atmosphere (40 mL/min) from ambient to 800 °C at a constant heating rate of 10 °C/min. X-ray diffraction (XRD) was performed on a Bruker-AXS D8 Advanced Bragg-Brentano X-ray Powder Diffractometer (Bruker AXS Inc, Madison, WI) with Cu-K_α incident radiation (λ = 1.5418 Å). Transmission electron microscopy (TEM) images were taken on a JEOL JEM-2010 TEM. Dielectric constant and loss tangents were measured on a Novocontrol broadband dielectric spectrometer with a frequency sweep of

1 Hz−10 MHz. Tensile tests and dynamic mechanical analysis were conducted using an RSA-G2 (TA Instruments) with a tensile fixture. Tensile tests were performed at 25 °C on rectangular samples (3 mm × 0.01 mm cross-section and 15 mm in length) with a crosshead speed of 10 mm/min. DMA was conducted in tensile mode at a strain amplitude of 0.05%, frequency of 1 Hz, and a heating rate of 3 °C /min from 40 °C to 180 °C. For CTE measurements, the gap between the fixtures was first zeroed at room temperature. After conditioning the fixture at 100 °C for 10 min, a 1 N force was applied. The small increase in spacing was used as a factor to correct for the CTE increase of the fixtures. Samples were then tested using a temperature ramp iso-force mode with a tensile stress of 50 mg mm^{-2}. The electrical conductivity of composite thin films was measured using a four-point-probe (Signatone, SP4-40045TBY) on a resistive stand (Signatone, Model 302).[86]

6.3. Results and discussion

6.3.1. Characterization of MWCNT-ZIF-8 hybrids

Two types of MWCNT-ZIF-8 hybrids have been designed for the present study, as shown in Figure 6-1. One hybrid was synthesized through the direct growth of ZIF-8 in MWCNT dispersion. The direct growth of ZIF-8 in MWCNT dispersion produces relatively large ZIF-8 particles at 500 nm as verified by XRD (Figure D-1) and TEM, which shows several MWCNTs in each ZIF-8 particle. It is likely that once ZIF-8 particles were nucleated on MWCNT surfaces, zinc ions and linkers would be adsorbed onto these nuclei and continuously grow into large MOF particles. The neighboring MWCNT were then encapsulated by the growing ZIF-8 to form the hybrid structure as seen in Figure

6-1a. This type of hybrid is named MWCNT-ZIF-8-D, where “D” represents a “Direct” synthesis of ZIF-8 on MWCNT.

Another kebab-like hybrid structure was synthesized by converting the decorated ZnO quantum dots on MWCNT to ZIF-8. The densely decorated ZnO quantum dots provide multiple, densely packed nucleation sites along the MWCNT surface. As a result, MWCNTs are decorated with 50 nm ZIF-8 nanoparticles throughout the length of MWCNT as seen in Figure 6-1b. This hybrid is named MWCNT-ZIF-8-C, where “C” represents “Conversion” from ZnO into ZIF-8.

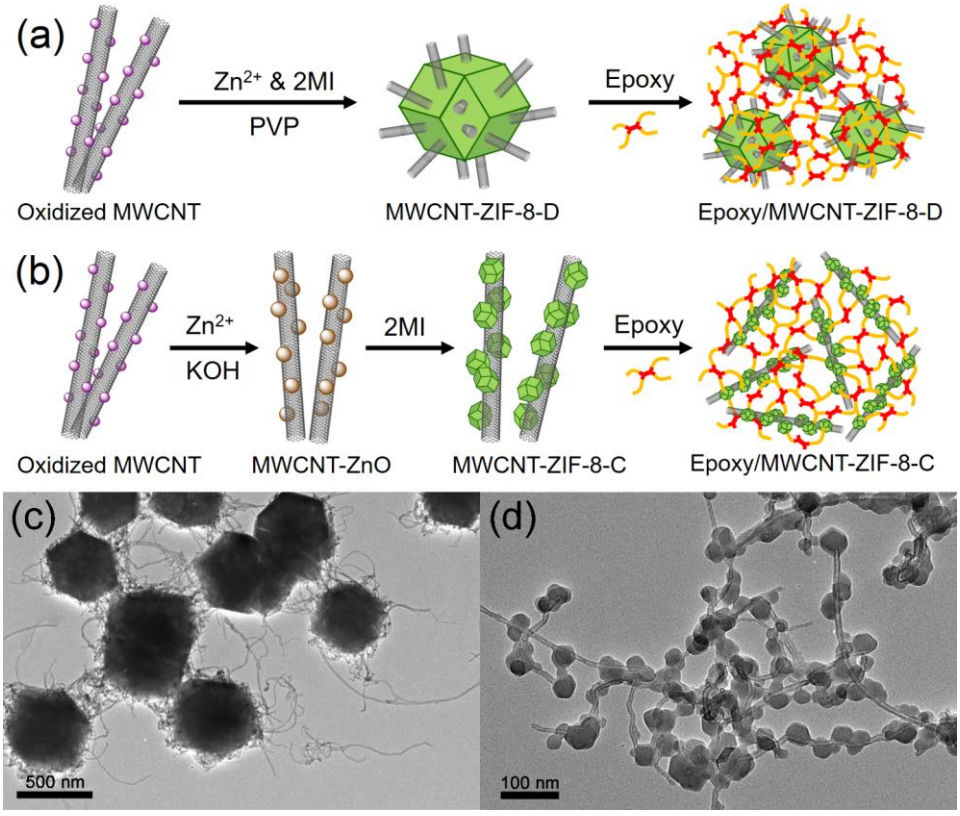

Figure 6-1. Schematic showing preparation of MWCNT-ZIF-8 hybrids with two different approaches: (a) MWCNT-ZIF-8-D, (b) MWCNT-ZIF-8-C, and TEM images of (c) MWCNT-ZIF-8-D and (d) MWCNT-ZIF-8-C.

The composition of the hybrids can be deduced from the TGA curves (Figure D-2). The mass fraction of MWCNT in MWCNT-ZIF-8-D and MWCNT-ZIF-8-C is 30% and 20%, respectively. MWCNT-ZIF-8-D and MWCNT-ZIF-8-C hybrids exhibit a two-step decomposition profile. It can be seen that the onset degradation temperature of MWCNT-ZIF-8-D is lower than that of MWCNT-ZIF-8-C, which is possibly due to the higher fraction of its exposed amorphous carbon on MWCNT than the latter.[86]

6.3.2. Curing process

One of the unique characteristics of the above approach is that MWCNT-ZIF-8 can cure epoxy resins without a need for further addition of curing agent or catalyst, which will minimize complexity in the nanocomposite composition as well as the fundamental understanding of their structure-property relationship. The effectiveness of the imidazole groups on the surface of ZIF-8 to initiate epoxy ring-opening polymerization was characterized using DSC. This mechanism has been well demonstrated in our previous study.[173] The 2-methyl imidazole on the surface of ZIF-8 can initiate anionic polymerization of epoxy resins. Figure D-3 shows the curing reactions of epoxy with MWCNT-ZIF-8-D and MWCNT-ZIF-8-C during a non-isothermal DSC scan at 10 °C/min, respectively. The amount of MWCNT is 1.5 wt% in both systems. The exothermic peak for epoxy/MWCNT-ZIF-8-C and MWCNT-ZIF-8-D appear at 240 °C and 280 °C, respectively, indicating a lower reactivity for MWCNT-ZIF-8-D. This is likely due to the large size of ZIF-8 crystals in MWCNT-ZIF-8-D, which possesses less surface area for imidazole to react with epoxy monomers.

DGEBF epoxy was chosen as the model epoxy resin. Epoxy thin films containing two kinds of MWCNT-ZIF-8 hybrids were prepared using a film applicator. The amount of MWCNT in both composite films is 1.5 wt%. Neat epoxy and epoxy/MWCNT (1.5 wt%) were also prepared by using DGEBF epoxy and cured using 2MI (5 wt%) for reference.

6.3.3. Morphology

The morphologies of the epoxy nanocomposite films are shown in Figure 6-2. The ZIF-8 nanoparticles appear dark in the images while the light background is the epoxy matrix. Figure 6-2a shows that ZIF-8-D particles are individually dispersed in the epoxy matrix, demonstrating the effectiveness of the 2MI functional group on ZIF-8 to help disperse the microparticles and form covalent bonding with epoxy. From the high magnification image, it is clearly shown that each ZIF-8 interacts and contains many MWCNTs. On the other hand, for the epoxy/MWCNT-ZIF-8-C nanocomposite (Figure 6-2d), MWCNT are disentangled and well-decorated by ZIF-8-C nanoparticles.

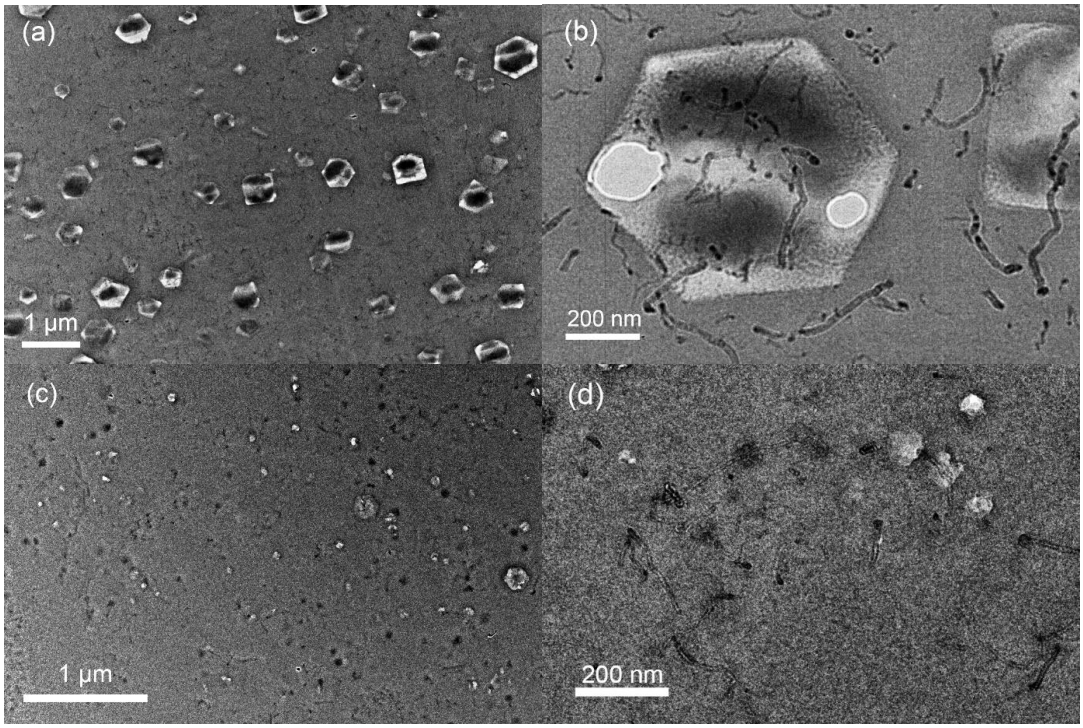

Figure 6-2. TEM of epoxy/MWCNT-ZIF-8-D at (a) low magnification and (b) high magnification and epoxy/MWCNT-ZIF-8-C nanocrystals at (c) low magnification and (d) high magnification.

6.3.4. DMA study

Dynamic mechanical analysis (DMA) was performed in a tensile mode to probe the effects of decorated MWCNT on dynamic mechanical behavior. Figure 6-3a shows storage modulus (*E'*) as a function of temperature for the neat epoxy and epoxy nanocomposites. The epoxy/MWCNT-ZIF-8-D and epoxy/MWCNT-ZIF-8-C nanocomposites exhibit over 15% and 33% increases in *E'*, respectively, compared to the neat epoxy at 35 °C. When the temperature increases to 180 °C, the nanocomposites containing MWCNT-ZIF-8-D and MWCNT-ZIF-8-C nanocrystals show over 100% increases in *E'* against the neat epoxy. The enhancement in the storage modulus of epoxy

nanocomposites with the decoration of MOF may be caused by the good dispersion of MWCNT and strong bonding between MWCNT and epoxy. A higher MWCNT/ZIF-8 interface area in epoxy/MWCNT-ZIF-8-C promotes a higher storage modulus increase.[57,60,159]

Moreover, it is noted that the nanocomposites exhibit slightly higher T_g than neat epoxy cured with 2MI and epoxy/MWCNT nanocomposites, which may be due to the strong covalent bonding of MWCNT-ZIF-8 with epoxy to restrict molecular scale motion around MWCNT-ZIF-8 nanoparticles. In addition, the large size of ZIF-8-D may lead to a heterogenous crosslinked network in epoxy nanocomposites containing MWCNT-ZIF-8-D. This fact is manifested by the broadening of the epoxy/MWCNT-ZIF-8-D T_g peak with respect to those of the next epoxy and epoxy/MWCNT-ZIF-8-C.

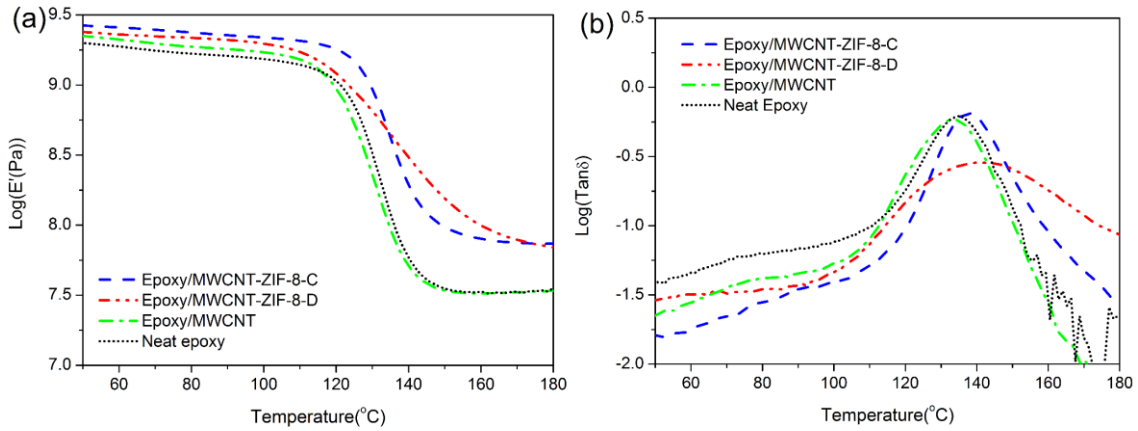

Figure 6-3. DMA plots of epoxy, epoxy/MWCNT, epoxy/MWCNT-ZIF-8 nanocomposites: (a) Storage modulus vs. temperature (b) Tan δ vs. temperature.

6.3.5. Dielectric behavior

Figure 6-4 shows the dependence of dielectric constant and dielectric loss on frequency for neat epoxy and various epoxy nanocomposites containing 1.5 wt% of MWCNT. It can be seen that the dielectric constant of the epoxy/MWCNT nanocomposite is strongly influenced by frequency. As frequency varies from 10 Hz to 1 MHz, the dielectric constant decreases from 234 to 7 and the dielectric loss decreases from 46 to 0.065. This phenomenon is characteristic to a typical percolative polymer composite due to the formation of conduction pathways as frequency increases in the frequency range investigated.[227,245] For a percolative system, the dielectric loss mainly consists of the conduction loss, which occurs at extremely low frequencies (below 10^2 Hz), and the polarization loss of space charges, which happens at 10^2–10^6 Hz. Generally, the former makes a greater contribution to the dielectric loss than the latter.[98] A large amount of charges induced by MWCNT cannot be stabilized under high-frequency conditions. Hence, the dielectric loss decreases significantly as the frequency increases because of the conduction relaxation.[246]

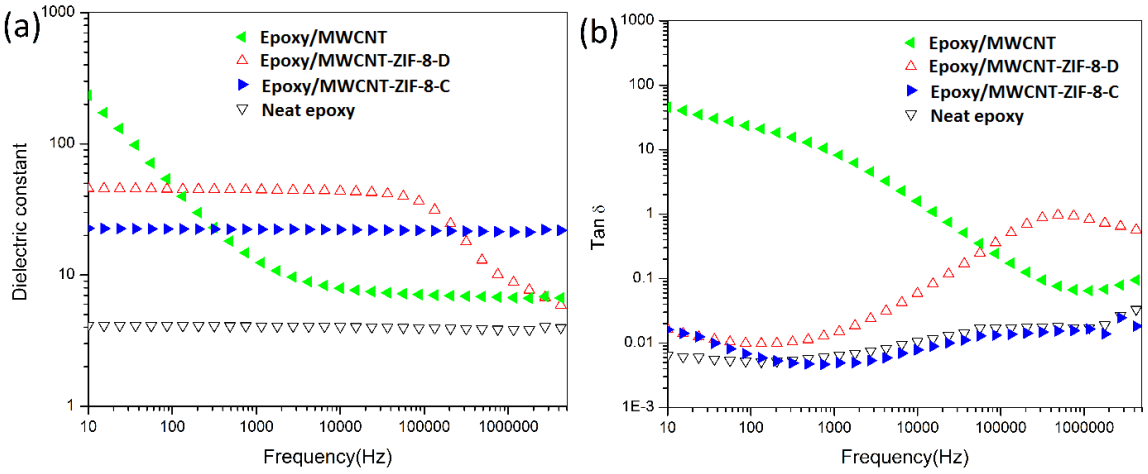

Figure 6-4. Dielectric behavior spectra of epoxy and epoxy nanocomposites: (a) Dielectric constant vs. frequency (b) Tan δ vs. frequency.

The above dielectric behavior was not observed for epoxy containing the MWCNT-ZIF-8 hybrids. The dielectric constant of the epoxy/MWCNT-ZIF-8-D nanocomposite is less sensitive to frequency than epoxy/MWCNT in the region below 10^4 Hz because the MWCNTs are contained in the large ZIF-8 particles and disperse well throughout the epoxy matrix. The conductive path is difficult to form at the same concentration of MWCNT compared with epoxy/MWCNT. Therefore, conduction relaxation is not observed. Since not all surfaces of MWCNTs are decorated by ZIF-8, the dielectric constant and dielectric loss still exhibit an obvious relaxation above 10^5 Hz, which corresponds to the interfacial polarization.[230] Interestingly, the dielectric behavior of epoxy/MWCNT-ZIF-8-C is not frequency-dependent up to 1 MHz of our machine limit. At 1 MHz, the dielectric constant is found to be 22, which is 7 times higher than a typical pristine epoxy, while the dielectric loss is as low as 0.01. Good dispersion of MWCNTs and the strong covalent bonding between MWCNT-ZIF-8-C and epoxy results

in a greatly reduced Maxwell-Wagner relaxation of the nanocomposite and reduced sensitivity to frequency. Compared with epoxy/MWCNT-ZIF-8-D, most surfaces of MWCNTs are decorated by ZIF-8-C in epoxy. Due to the coverage of the insulative small size ZIF-8-C on MWCNTs, the dielectric constant of epoxy/MWCNT-ZIF-8-C is lower than that of epoxy/MWCNT-ZIF-8-D. This is attributed to the better coverage of ZIF-8-C on MWCNT and the presence of strong bonding between ZIF-8-C and the epoxy matrix, the interfacial relaxation has been retarded. Consequently, the epoxy/MWCNT-ZIF-8-C nanocomposite can possess nearly frequency-independent high dielectric constant and low dielectric loss. The morphological differences between MWCNT-ZIF-8-C and MWCNT-ZIF-8-D are also reflected on their electrical conductivity behavior (Table D-1). The electrical conductivity of MWCNT-ZIF-8 is much lower than that of the MWCNT because ZIF-8 serves as a spacer to minimize direct contact between MWCNTs. The uniformity and density of ZIF-8 coverage on MWCNT surfaces in MWCNT-ZIF-8-C results in a much lower electrical conductivity than that in MWCNT-ZIF-8-D.

6.3.6. Mechanical properties and CTE

The engineering stress–strain curves of the neat epoxy and corresponding nanocomposites are presented in Figure 6-5. Compared to neat epoxy, Young's moduli of the epoxy/MWCNT-ZIF-8-D and epoxy/MWCNT-ZIF-8-C nanocomposites significantly increase from 2.8 to 3.6 and 4.1 GPa, respectively. MWCNT-ZIF-8-C shows a more pronounced enhancement in Young's modulus than MWCNT-ZIF-8-D, which should be due to the greater contact area between the nanoparticles and the epoxy. However, the epoxy/MWCNT-ZIF-8-C shows a lower elongation-at-break than epoxy/MWCNT-ZIF-

8-D. The decrease in elongation at break is possibly due to the low molecular mobility of the epoxy network structure caused by the presence of the immobile and nano-sized MWCNT-ZIF-8 hybrids. The above findings reveal the importance of the nanoparticle dispersion and interfacial adhesion in enhancing the modulus of the nanocomposites. It is evident that the tensile properties of MWCNT-based nanocomposites can be tailored by the MOF chemistry.

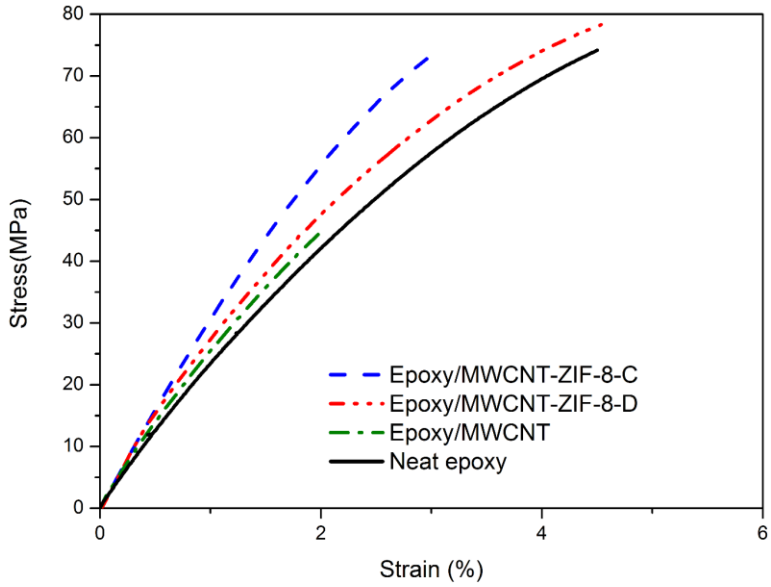

Figure 6-5. Engineering stress–strain curves obtained at 25 °C for neat epoxy, epoxy/MWCNT and epoxy/MWCNT-ZIF-8 nanocomposites.

Lowering the coefficient of thermal expansion (CTE) of polymeric encapsulation compounds to match those of the substrates, such as copper and silicon, is one of the main challenges facing the microelectronics industry. Because of the high modulus of MWCNT and strong covalent bonding between ZIF-8 and epoxy, the epoxy/MWCNT-ZIF-8

nanocomposites are expected to exhibit lower CTE values. Figure D-4 shows the dimensional change as a function of temperature on neat epoxy, epoxy/MWCNT-ZIF-8-D and epoxy/MWCNT- ZIF-8-C. Compared to neat epoxy, both epoxy nanocomposites show lower CTE values. The CTE is reduced by over 30% by adding MWCNT-ZIF-8-D, while a reduction of 50% was observed with the addition of MWCNT-ZIF-8-C. As MWCNT-ZIF-8-C has a larger surface contact area with the epoxy matrix than MWCNT-ZIF-8-D, the confinement effect due to the nanoparticles will be more pronounced. These results indicate that adding MWCNT-ZIF-8 hybrids in epoxy reduces CTE, which is most likely because of the presence of rigid nanoparticles inhibiting the mobility of polymeric chains.

Table 6-1. Young's modulus, tensile strength, elongation and CTE of neat epoxy, epoxy/MWCNT, and epoxy/MWCNT-ZIF-8 nanocomposites.

Sample	**Young's modulus (GPa)**	**Tensile strength (MPa)**	**Elongation (%)**	**CTE (ppm/K)**
Neat epoxy	2.8±0.3	70±5	4.2±0.5	73
Epoxy/MWCNT	3.0±0.2	45±4	2.4±0.7	62
Epoxy/MWCNT-ZIF-8-D	3.6±0.3	78±7	4.6±0.8	53
Epoxy/MWCNT-ZIF-8-C	4.1±0.2	75±4	3.1±0.9	38

From the experimental findings above, it is shown that filler-polymer interface plays an important role in controlling the dielectric and mechanical properties of high k

polymer nanocomposites. Compared with epoxy/MWCNT, the epoxy/MWCNT-ZIF-8 systems possess superior dielectric stability, higher Young's modulus and lower CTE. The good dispersion of MWCNT minimizes the formation of local conductive pathways, leading to a lower dielectric loss. Furthermore, a strong chemical bonding between MWCNT-ZIF-8 and epoxy helps to stabilize the charge distribution at the interface and enhances stress transfer between the phases. Compared to epoxy/MWCNT-ZIF-8-D, epoxy/MWCNT-ZIF-8-C exhibits a lower dielectric loss, higher Young's modulus, and lower CTE, due to their better MOF coverage on MWCNT and a higher surface area contact with the epoxy matrix. Therefore, a tailored design of filler-polymer interface utilizing MOF is an effective and promising approach to optimize dielectric and mechanical properties.

Compared with conventional surface modifiers, such as small molecules and inorganic nanoparticles, MOF combines the advantages of its high rigidity and strong bonding to polymer matrix for additional physical and mechanical properties improvements. Another attractive merit of the present approach is the broad choices of MOF available to decorate a variety of nanoparticles for dispersion in polymer matrices [247-249]. It should be noted that the present study is not limited to the dispersion of MOF-decorated nanoparticles in epoxy. MOF has the potential to initiate polymerization in many kinds of polymers, such as polymethylmethacrylate, polyolefins and polystyrene,[250] or form strong bonding with polymer matrices through suitable ligand selection and molecular design. Therefore, the strategy presented here is applicable in many

applications, such as microelectronics, catalysis, energy storage, structural components, for many years to come.

6.4. Conclusion

A set of novel self-curing MWCNT-based epoxy matrix nanocomposites possessing good dielectric properties, excellent mechanical properties and low CTE were prepared using ZIF-8 as a modifier to decorate MWCNT. ZIF-8 serves both as a curing agent of epoxy and as electrical barriers among MWCNTs in epoxy matrix. This strategy ensures the good dispersion and bonding of MWCNT with the matrix. With the modification of ZIF-8, epoxy nanocomposites form a stable network with high k (22 at 1 MHz) and low k loss (0.01 at 1 MHz). The dielectric and mechanical properties of epoxy/MWCNT-ZIF-8 can be altered by changing their morphology at interface. The high dielectric constant, low dielectric loss, low CTE, excellent mechanical properties and easy processability of epoxy/MWCNT-ZIF-8 nanocomposites are well-suited for microelectronics and energy storage applications.

7. CONCLUSIONS AND FUTURE DIRECTIONS

7.1. Conclusions

Polymer nanocomposites offer significant potential in the development of advanced materials for numerous applications. These novel materials benefit from the synergy between filler particles and polymer chains that are on similar length scales and the large quantity of interfacial area relative to the volume of the material. Although enhanced properties of these materials have been demonstrated by numerous researchers, our fundamental knowledge of the "interface" effect is not fully developed. Depending on the dispersion state of the nanofiller and the interface area, the resulting interfacial region can be a critical component in polymer nanocomposites. Therefore, the overall objective of my dissertation is to develop new approaches to manipulate the interface of the nanocomposites, study the role of the interface in influencing mechanical behavior of polymer nanocomposites, and fabricate high performance and multi-functional polymer nanocomposites.

The interfacial region between nanoparticles and polymer matrix plays a critical role in influencing the mechanical behavior of polymer nanocomposites. In this work, a set of model systems based on polymethylmethacrylate (PMMA) matrix containing polyalkylglycidylether brushes grafted on 50 nm metal-organic-framework (MOF) nanoparticles were synthesized and investigated. The nanoparticle surface has been manipulated by grafting different length and grafting density of polyalkylglycidylether brushes. It is found that polymer brushes grafted ZIF-8 nanoparticles greatly enhances the

fracture toughness of the PMMA matrix while maintaining the Young's modulus. Our results also reveal that the model systems toughened by nanoparticles with different polymer brush characteristics may lead to distinctly different toughening mechanisms from a few big crazes to massive crazing, and to nanoparticle voiding and matrix shear banding. High performance multifunctional polymer nanocomposites with high fracture toughness can be successfully designed and prepared.

Novel epoxy nanocomposites based on TBA-exfoliated α-ZrP nanoplatelets have been prepared. TBA serves as a surfactant and curing catalyst by forming a phosphate anion pair on α-ZrP surface to initiate the polymerization of epoxy resins, and the α-ZrP nanoplatelets act as a reinforcement to improve the mechanical properties of epoxy. The epoxy/α-ZrP-TBA nanocomposites exhibit greatly increased Young's modulus of 4.3 GPa due to the strong covalent bonding between the nanoplatelets and epoxy matrix. In addition, epoxy/α-ZrP-TBA nanocomposites are highly toughenable. With an addition of 3 vol% core-shell rubber particles, the K_{IC} value is improved from 0.55 to 1.55 MPa $m^{1/2}$. The main toughening mechanisms in epoxy/α-ZrP-TBA/CSR are rubber particle cavitation, followed by matrix shear banding. The hybrid epoxy/α-ZrP-TBA/CSR nanocomposites possess good potential as high-performance structural materials for aerospace and automotive applications.

A metal-organic-framework (MOF) based on zeolitic imidazole framework (ZIF-8) is utilized as a modifier to lower the dielectric constant and improve the mechanical properties of an epoxy matrix. The imidazole group on the surface of the ZIF-8 initiates epoxy curing, resulting in covalent bonding between the ZIF-8 crystals and epoxy matrix.

Epoxy/ZIF-8 nanocomposites, with filler contents up to 25 vol%, can easily be processed by hot press. The strong interfacial bonding between ZIF-8 and epoxy matrix helps to increase the Young's modulus by 20%. Furthermore, because of the intrinsically porous and hydrophobic nature of ZIF-8, nanocomposites show lower dielectric constant and moisture uptake, which makes them excellent candidates as low-k dielectrics. ZIF-8 nanoparticles are well dispersed in the epoxy matrix without surface modification or addition of surfactant. The simple process can be easily scaled up to produce nanocomposites containing metal organic frameworks. This work can be readily extended to other MOF-containing polymer nanocomposites by functionalization of MOF to the chemical nature of the polymer matrix.

A set of novel self-curing MWCNT-based epoxy matrix nanocomposites possessing good dielectric properties, excellent mechanical properties and low CTE were prepared using ZIF-8 as a modifier to decorate MWCNT. ZIF-8 serves both as a curing agent of epoxy and as electrical barriers among MWCNTs in epoxy matrix. This strategy ensures the good dispersion and bonding of MWCNT with the matrix. With the modification of ZIF-8, epoxy nanocomposites form a stable network with high k (22 at 1 MHz) and low k loss (0.01 at 1 MHz). The dielectric and mechanical properties of epoxy/MWCNT-ZIF-8 can be altered by changing their morphology at interfacial. The high dielectric constant, low dielectric loss, low CTE, excellent mechanical properties and easy processability of epoxy/MWCNT-ZIF-8 nanocomposites are well-suited for microelectronics and energy storage applications.

7.2. Future directions

7.2.1. Strain rate effect on mechanical properties of polymer nanocomposites

Due to the viscoelastic nature of polymers, a lower strain rate usually leads to higher fracture toughness. A possible reason for the strain rate sensitivity is an increased available time for molecular mobility, thus dissipating the applied mechanical energy more effectively. In rubber toughening systems, the fracture toughness improvements are highly constrained in a high strain rate as no extensive cavitation can take place around the crack tip to trigger massive plastic deformation of the polymer matrix. However, in the practical usage, materials with less rate dependence is preferred. One of our future is to study the strain rate dependence of the PMMA/ZIF-8-LC systems. The unusual interfaces modified by the polymer brushes and the unique structure of MOF may lead to an unprecedented fracture behavior in a higher test rate.

7.2.2. Other important factors in toughening

This dissertation addresses some critical issues in the effects of the interface on the fracture behavior of the polymer nanocomposites. However, a few other important questions remain unanswered. One of them is the concentration effect. The current research only studies the case with 3 wt% loading. The effectiveness of higher (or lower) concentrations would be of interest and worth to study. Another important factor is the size effect. Although we have revealed the effectiveness of 50-90 nm nanoparticles toughening, we have not compared that with other particle sizes.

7.2.3. Effect of the interface on the gas separation performance

Various polymers and MOFs have been employed to fabricate symmetric dense MOF mix matrix membranes (MMMs).[251] However, there are still some problems in fabricating MOF-based MMMs are: (1) the poor interaction between the MOF particles and polymer matrix resulting in non-selective defects; (2) the agglomeration of the particles within the polymer that decreases the selectivity properties of the membranes; (3) the plasticization effect of the polymer under high pressure.[252] The polymer brushes modification strategy may address these issues and enhance the gas separation performance. PMMA/ZIF-8-SC and PMMA/ZIF-8-LC are good modal systems to study the effect of the interfacial interactions between polymer brushes and the polymer matrix to the gas diffusion efficiency.

REFERENCES

1. Fu, S.; Sun, Z.; Huang, P.; Li, Y.; Hu, N., Some Basic Aspects of Polymer Nanocomposites: A Critical Review. *Nano Mater. Sci.* **2019,** *1* (1), 2-30.

2. Kumar, S. K.; Benicewicz, B. C.; Vaia, R. A.; Winey, K. I., 50th Anniversary Perspective: Are Polymer Nanocomposites Practical for Applications? *Macromolecules* **2017,** *50* (3), 714-731.

3. Tjong, S. C., Structural and Mechanical Properties of Polymer Nanocomposites. *Mater. Sci. Eng., R* **2006,** *53* (3-4), 73-197.

4. Ajayan, P. M.; Schadler, L. S.; Braun, P. V., *Nanocomposite Science and Technology*. John Wiley & Sons: 2006.

5. Hu, N.; Masuda, Z.; Yan, C.; Yamamoto, G.; Fukunaga, H.; Hashida, T., The Electrical Properties of Polymer Nanocomposites with Carbon Nanotube Fillers. *Nanotechnology* **2008,** *19* (21), 215701.

6. Schadler, L. S.; Kumar, S. K.; Benicewicz, B. C.; Lewis, S. L.; Harton, S. E., Designed Interfaces in Polymer Nanocomposites: A Fundamental Viewpoint. *MRS Bull.* **2007,** *32* (4), 335-340.

7. Li, Y.; Huang, Y.; Krentz, T.; Natarajan, B.; Neely, T.; Schadler, L. S., Polymer Nanocomposite Interfaces: The Hidden Lever for Optimizing Performance in Spherical Nanofilled Polymers. In *Interface/Interphase in Polymer Nanocomposites*, 2016; pp 1-69.

8. Zhang, X.; Li, B.-W.; Dong, L.; Liu, H.; Chen, W.; Shen, Y.; Nan, C.-W., Superior Energy Storage Performances of Polymer Nanocomposites Via Modification of Filler/Polymer Interfaces. *Advanced Materials Interfaces* **2018,** *5* (11), 1800096.

9. Zandinejad, A. A.; Atai, M.; Pahlevan, A., The Effect of Ceramic and Porous Fillers on the Mechanical Properties of Experimental Dental Composites. *Dent. Mater.* **2006,** *22* (4), 382-7.

10. Li, H.; Eddaoudi, M.; O'Keeffe, M.; Yaghi, O. M., Design and Synthesis of an Exceptionally Stable and Highly Porous Metal-Organic Framework. *Nature* **1999,** *402* (6759), 276-279.

11. Li, J. R.; Kuppler, R. J.; Zhou, H. C., Selective Gas Adsorption and Separation in Metal-Organic Frameworks. *Chem. Soc. Rev.* **2009,** *38* (5), 1477-504.

12. Howarth, A. J.; Liu, Y.; Li, P.; Li, Z.; Wang, T. C.; Hupp, J. T.; Farha, O. K., Chemical, Thermal and Mechanical Stabilities of Metal–Organic Frameworks. *Nat. Rev. Mater.* **2016,** *1* (3), 15018.

13. Khare, H.; Burris, D., A Quantitative Method for Measuring Nanocomposite Dispersion. *Polymer* **2010,** *51* (3), 719-729.

14. Kumar, S. K.; Krishnamoorti, R., Nanocomposites: Structure, Phase Behavior, and Properties. *Annu. Rev. Chem. Biomol. Eng.* **2010,** *1*, 37-58.

15. Hooper, J.; Schweizer, K. S.; Desai, T.; Koshy, R.; Keblinski, P., Structure, Surface Excess and Effective Interactions in Polymer Nanocomposite Melts and Concentrated Solutions. *J. Chem. Phys.* **2004,** *121* (14), 6986-6997.

16. Akcora, P.; Liu, H.; Kumar, S. K.; Moll, J.; Li, Y.; Benicewicz, B. C.; Schadler, L. S.; Acehan, D.; Panagiotopoulos, A. Z.; Pryamitsyn, V., Anisotropic Self-Assembly of Spherical Polymer-Grafted Nanoparticles. *Nat. Mater.* **2009,** *8* (4), 354-359.

17. Chevigny, C.; Dalmas, F.; Di Cola, E.; Gigmes, D.; Bertin, D.; Boué, F.; Jestin, J., Polymer-Grafted-Nanoparticles Nanocomposites: Dispersion, Grafted Chain Conformation, and Rheological Behavior. *Macromolecules* **2011,** *44* (1), 122-133.

18. Kumar, S. K.; Jouault, N.; Benicewicz, B.; Neely, T., Nanocomposites with Polymer Grafted Nanoparticles. *Macromolecules* **2013,** *46* (9), 3199-3214.

19. Hong, J.; Winberg, P.; Schadler, L.; Siegel, R., Dielectric Properties of Zinc Oxide/Low Density Polyethylene Nanocomposites. *Mater. Lett.* **2005,** *59* (4), 473-476.

20. Natarajan, B.; Li, Y.; Deng, H.; Brinson, L. C.; Schadler, L. S., Effect of Interfacial Energetics on Dispersion and Glass Transition Temperature in Polymer Nanocomposites. *Macromolecules* **2013,** *46* (7), 2833-2841.

21. Ieda, M., Dielectric Breakdown Process of Polymers. *IEEE Trans. Electr. Insul.* **1980,** *EI-15* (3), 206-224.

22. Siddabattuni, S.; Schuman, T. P.; Dogan, F., Dielectric Properties of Polymer–Particle Nanocomposites Influenced by Electronic Nature of Filler Surfaces. *ACS Appl. Mater. Interfaces* **2013,** *5* (6), 1917-1927.

23. Wei, J.; Zhang, Z.; Tseng, J.-K.; Treufeld, I.; Liu, X.; Litt, M. H.; Zhu, L., Achieving High Dielectric Constant and Low Loss Property in a Dipolar Glass Polymer Containing Strongly Dipolar and Small-Sized Sulfone Groups. *ACS Appl. Mater. Interfaces* **2015,** *7* (9), 5248-5257.

24. Luo, H.; Zhou, X.; Ellingford, C.; Zhang, Y.; Chen, S.; Zhou, K.; Zhang, D.; Bowen, C. R.; Wan, C., Interface Design for High Energy Density Polymer Nanocomposites. *Chem. Soc. Rev.* **2019,** *48* (16), 4424-4465.

25. Tao, P.; Viswanath, A.; Schadler, L. S.; Benicewicz, B. C.; Siegel, R. W., Preparation and Optical Properties of Indium Tin Oxide/Epoxy Nanocomposites with Polyglycidyl Methacrylate Grafted Nanoparticles. *ACS Appl. Mater. Interfaces* **2011,** *3* (9), 3638-3645.

26. Tao, P.; Li, Y.; Rungta, A.; Viswanath, A.; Gao, J.; Benicewicz, B. C.; Siegel, R. W.; Schadler, L. S., Tio 2 Nanocomposites with High Refractive Index and Transparency. *J. Mater. Chem.* **2011,** *21* (46), 18623-18629.

27. Achilleos, D. S.; Vamvakaki, M., End-Grafted Polymer Chains onto Inorganic Nano-Objects. *Materials* **2010,** *3* (3), 1981-2026.

28. Tchoul, M. N.; Fillery, S. P.; Koerner, H.; Drummy, L. F.; Oyerokun, F. T.; Mirau, P. A.; Durstock, M. F.; Vaia, R. A., Assemblies of Titanium Dioxide-Polystyrene Hybrid Nanoparticles for Dielectric Applications. *Chem. Mater.* **2010,** *22* (5), 1749-1759.

29. Hojjati, B.; Charpentier, P. A., Synthesis and Kinetics of Graft Polymerization of Methyl Methacrylate from the Raft Coordinated Surface of Nano-TiO_2. *J. Polym. Sci., Part A: Polym. Chem.* **2008,** *46* (12), 3926-3937.

30. Hojjati, B.; Sui, R.; Charpentier, P. A., Synthesis of TiO_2/Paa Nanocomposite by Raft Polymerization. *Polymer* **2007,** *48* (20), 5850-5858.

31. Roy, M.; Nelson, J.; MacCrone, R.; Schadler, L. S.; Reed, C.; Keefe, R., Polymer Nanocomposite Dielectrics-the Role of the Interface. *IEEE Trans. Dielectr. Electr. Insul.* **2005,** *12* (4), 629-643.

32. Crosby, A. J.; Lee, J. Y., Polymer Nanocomposites: The "Nano" Effect on Mechanical Properties. *Polym. Rev.* **2007,** *47* (2), 217-229.

33. Putz, K. W.; Palmeri, M. J.; Cohn, R. B.; Andrews, R.; Brinson, L. C., Effect of Cross-Link Density on Interphase Creation in Polymer Nanocomposites. *Macromolecules* **2008,** *41* (18), 6752-6756.

34. Shojaei, A.; Faghihi, M., Physico-Mechanical Properties and Thermal Stability of Thermoset Nanocomposites Based on Styrene-Butadiene Rubber/Phenolic Resin Blend. *Mater. Sci. Eng., A* **2010,** *527* (4-5), 917-926.

35. Liu, S.; Zhang, H.; Zhang, Z.; Sprenger, S., Epoxy Resin Filled with High Volume Content Nano-SiO_2 Particles. *J. Nanosci. Nanotechnol.* **2009,** *9* (2), 1412-1417.

36. Natarajan, B.; Neely, T.; Rungta, A.; Benicewicz, B. C.; Schadler, L. S., Thermomechanical Properties of Bimodal Brush Modified Nanoparticle Composites. *Macromolecules* **2013,** *46* (12), 4909-4918.

37. Starr, F. W.; Schrøder, T. B.; Glotzer, S. C., Effects of a Nanoscopic Filler on the Structure and Dynamics of a Simulated Polymer Melt and the Relationship to Ultrathin Films. *Phys. Rev. E* **2001,** *64* (2), 021802.

38. Pissis, P.; Fragiadakis, D.; Kanapitsas, A.; Delides, K., Broadband Dielectric Relaxation Spectroscopy in Polymer Nanocomposites. *Macromol. Symp.* **2008,** *265* (1), 12-20.

39. Priestley, R. D.; Ellison, C. J.; Broadbelt, L. J.; Torkelson, J. M., Structural Relaxation of Polymer Glasses at Surfaces, Interfaces, and in Between. *Science* **2005,** *309* (5733), 456-459.

40. Berriot, J.; Montes, H.; Lequeux, F.; Long, D.; Sotta, P., Evidence for the Shift of the Glass Transition near the Particles in Silica-Filled Elastomers. *Macromolecules* **2002,** *35* (26), 9756-9762.

41. Forrest, J. A.; Dalnoki-Veress, K.; Stevens, J. R.; Dutcher, J. R., Effect of Free Surfaces on the Glass Transition Temperature of Thin Polymer Films. *Phys Rev Lett* **1996,** *77* (10), 2002-2005.

42. Bansal, A.; Yang, H.; Li, C.; Cho, K.; Benicewicz, B. C.; Kumar, S. K.; Schadler, L. S., Quantitative Equivalence between Polymer Nanocomposites and Thin Polymer Films. *Nat. Mater.* **2005,** *4* (9), 693-698.

43. Rittigstein, P.; Priestley, R. D.; Broadbelt, L. J.; Torkelson, J. M., Model Polymer Nanocomposites Provide an Understanding of Confinement Effects in Real Nanocomposites. *Nat. Mater.* **2007,** *6* (4), 278-282.

44. Lan, T.; Torkelson, J. M., Substantial Spatial Heterogeneity and Tunability of Glass Transition Temperature Observed with Dense Polymer Brushes Prepared by Arget Atrp. *Polymer* **2015,** *64*, 183-192.

45. Gao, J.; Li, J.; Benicewicz, B. C.; Zhao, S.; Hillborg, H.; Schadler, L. S., The Mechanical Properties of Epoxy Composites Filled with Rubbery Copolymer Grafted SiO_2. *Polymers* **2012,** *4* (1), 187-210.

46. Tadiello, L.; D'Arienzo, M.; Di Credico, B.; Hanel, T.; Matejka, L.; Mauri, M.; Morazzoni, F.; Simonutti, R.; Spirkova, M.; Scotti, R., The Filler–Rubber Interface in Styrene Butadiene Nanocomposites with Anisotropic Silica Particles: Morphology and Dynamic Properties. *Soft Matter* **2015,** *11* (20), 4022-4033.

47. Holt, A. P.; Griffin, P. J.; Bocharova, V.; Agapov, A. L.; Imel, A. E.; Dadmun, M. D.; Sangoro, J. R.; Sokolov, A. P., Dynamics at the Polymer/Nanoparticle Interface in Poly (2-Vinylpyridine)/Silica Nanocomposites. *Macromolecules* **2014,** *47* (5), 1837-1843.

48. Mazurin, O., Problems of Compatibility of the Values of Glass Transition Temperatures Published in the World Literature. *Glass Phys. Chem* **2007,** *33* (1), 22-36.

49. Miyagawa, H.; Misra, M.; Mohanty, A. K., Mechanical Properties of Carbon Nanotubes and Their Polymer Nanocomposites. *J. Nanosci. Nanotechnol.* **2005,** *5* (10), 1593-1615.

50. Podsiadlo, P.; Kaushik, A. K.; Arruda, E. M.; Waas, A. M.; Shim, B. S.; Xu, J.; Nandivada, H.; Pumplin, B. G.; Lahann, J.; Ramamoorthy, A., Ultrastrong and Stiff Layered Polymer Nanocomposites. *Science* **2007,** *318* (5847), 80-83.

51. Kausch - Blecken von Schmeling, H.; Williams, J., Polymer Fracture. *Encyclopedia of Polymer Science and Technology* **2002**, 1-65.

52. Cotterell, B.; Chia, J.; Hbaieb, K., Fracture Mechanisms and Fracture Toughness in Semicrystalline Polymer Nanocomposites. *Eng. Fract. Mech.* **2007,** *74* (7), 1054-1078.

53. Sue, H.-J.; Gam, K.; Bestaoui, N.; Clearfield, A.; Miyamoto, M.; Miyatake, N., Fracture Behavior of A-Zirconium Phosphate-Based Epoxy Nanocomposites. *Acta Mater.* **2004,** *52* (8), 2239-2250.

54. Sue, H.-J., Study of Rubber-Modified Brittle Epoxy Systems. Part Ii: Toughening Mechanisms under Mode-I Fracture. *Polym. Eng. Sci.* **1991,** *31* (4), 275-288.

55. Parker, D. S.; Sue, H. J.; Huang, J.; Yee, A. F., Toughening Mechanisms in Core-Shell Rubber Modified Polycarbonate. *Polymer* **1990,** *31* (12), 2267-2277.

56. Sue, H. J.; Gam, K. T.; Bestaoui, N.; Clearfield, A.; Miyamoto, M.; Miyatake, N., Fracture Behavior of A-Zirconium Phosphate-Based Epoxy Nanocomposites. *Acta Mater.* **2004,** *52* (8), 2239-2250.

57. Gam, K. T.; Miyamoto, M.; Nishimura, R.; Sue, H. J., Fracture Behavior of Core-Shell Rubber–Modified Clay-Epoxy Nanocomposites. *Polym. Eng. Sci.* **2003,** *43* (10), 1635-1645.

58. Chen, J.; Kinloch, A. J.; Sprenger, S.; Taylor, A. C., The Mechanical Properties and Toughening Mechanisms of an Epoxy Polymer Modified with Polysiloxane-Based Core-Shell Particles. *Polymer* **2013**, *54* (16), 4276-4289.

59. Sue, H.-J.; Bertram, J.; Garcia-Meitin, E.; Wilchester, J.; Walker, L., Fracture Behavior of Core-Shell Rubber-Modified Crosslinkable Epoxy Thermoplastics. *Colloid. Polym. Sci.* **1994,** *272* (4), 456-466.

60. Liu, C.; Zhu, Z.; Molero, G.; Chen, Q.; Kotaki, M.; Mullins, M.; Sue, H.-J., Mechanical Behavior of Self-Curing Epoxy Nanocomposites. *Polymer* **2019,** *179*, 121631.

61. Usuki, A.; Kojima, Y.; Kawasumi, M.; Okada, A.; Fukushima, Y.; Kurauchi, T.; Kamigaito, O., Synthesis of Nylon 6-Clay Hybrid. *J. Mater. Res.* **1993,** *8* (5), 1179-1184.

62. Kojima, Y.; Usuki, A.; Kawasumi, M.; Okada, A.; Fukushima, Y.; Kurauchi, T.; Kamigaito, O., Mechanical Properties of Nylon 6-Clay Hybrid. *J. Mater. Res.* **1993,** *8* (5), 1185-1189.

63. Pearson, R. A.; Yee, A. F., Influence of Particle Size and Particle Size Distribution on Toughening Mechanisms in Rubber-Modified Epoxies. *J. Mater. Sci.* **1991,** *26* (14), 3828-3844.

64. Gilbert, D.; Donald, A., Toughening Mechanisms in High Impact Polystyrene. *J. Mater. Sci.* **1986,** *21* (5), 1819-1823.

65. Eiras, D.; Pessan, L. A., Mechanical Properties of Polypropylene/Calcium Carbonate Nanocomposites. *Materials Research* **2009,** *12* (4), 517-522.

66. Fu, S.-Y.; Feng, X.-Q.; Lauke, B.; Mai, Y.-W., Effects of Particle Size, Particle/Matrix Interface Adhesion and Particle Loading on Mechanical Properties of Particulate–Polymer Composites. *Composites Part B* **2008,** *39* (6), 933-961.

67. Bazhenov, S., Fillers: Their Effect on the Failure Modes of Plastics. In *Plastics Additives*, Springer: 1998; pp 252-259.

68. Tochin, V.; Shchupak, E.; Tumanov, V.; Kulachinskaya, O.; Gai, M., Concentration Dependence of the Deformation Characteristics of High-Density Polyethylene Compositions with Dispersed Fillers. *Mech. Compos. Mater.* **1985,** *20* (4), 440-443.

69. Njuguna, J.; Pielichowski, K.; Desai, S., Nanofiller - Reinforced Polymer Nanocomposites. *Polym. Adv. Technol.* **2008,** *19* (8), 947-959.

70. Gao, J.; Li, J.; Zhao, S.; Benicewicz, B. C.; Hillborg, H.; Schadler, L. S., Effect of Graft Density and Molecular Weight on Mechanical Properties of Rubbery Block Copolymer Grafted SiO_2 Nanoparticle Toughened Epoxy. *Polymer* **2013,** *54* (15), 3961-3973.

71. Kutvonen, A.; Rossi, G.; Puisto, S. R.; Rostedt, N. K.; Ala-Nissila, T., Influence of Nanoparticle Size, Loading, and Shape on the Mechanical Properties of Polymer Nanocomposites. *J. Chem. Phys.* **2012,** *137* (21), 214901.

72. Maillard, D.; Kumar, S. K.; Fragneaud, B.; Kysar, J. W.; Rungta, A.; Benicewicz, B. C.; Deng, H.; Brinson, L. C.; Douglas, J. F., Mechanical Properties of Thin Glassy Polymer Films Filled with Spherical Polymer-Grafted Nanoparticles. *Nano Lett.* **2012,** *12* (8), 3909-3914.

73. Giovino, M.; Pribyl, J.; Benicewicz, B.; Bucinell, R.; Schadler, L., Mechanical Properties of Polymer Grafted Nanoparticle Composites. *Nanocomposites* **2018,** *4* (4), 244-252.

74. Nalwa, H. S., *Handbook of Low and High Dielectric Constant Materials and Their Applications, Two-Volume Set*. Elsevier: 1999.

75. Huang, X.; Jiang, P., Core–Shell Structured High‐K Polymer Nanocomposites for Energy Storage and Dielectric Applications. *Adv. Mater.* **2015,** *27* (3), 546-554.

76. Rao, Y.; Yue, J.; Wong, C., Material Characterization of High Dielectric Constant Polymer–Ceramic Composite for Embedded Capacitor to Rf Application. *Act. Passive Electron. Compon.* **2002,** *25* (1), 123-129.

77. Dang, Z. M.; Yuan, J. K.; Yao, S. H.; Liao, R. J., Flexible Nanodielectric Materials with High Permittivity for Power Energy Storage. *Adv. Mater.* **2013,** *25* (44), 6334-6365.

78. Neese, B.; Chu, B.; Lu, S.-G.; Wang, Y.; Furman, E.; Zhang, Q., Large Electrocaloric Effect in Ferroelectric Polymers near Room Temperature. *Science* **2008,** *321* (5890), 821-823.

79. Zhang, G.; Li, Q.; Gu, H.; Jiang, S.; Han, K.; Gadinski, M. R.; Haque, M. A.; Zhang, Q.; Wang, Q., Ferroelectric Polymer Nanocomposites for Room‐Temperature Electrocaloric Refrigeration. *Adv. Mater.* **2015,** *27* (8), 1450-1454.

80. Zhang, Q.; Li, H.; Poh, M.; Xia, F.; Cheng, Z.-Y.; Xu, H.; Huang, C., An All-Organic Composite Actuator Material with a High Dielectric Constant. *Nature* **2002,** *419* (6904), 284-287.

81. Brochu, P.; Pei, Q., Advances in Dielectric Elastomers for Actuators and Artificial Muscles. *Macromol. Rapid Commun.* **2010,** *31* (1), 10-36.

82. Maier, G., Low Dielectric Constant Polymers for Microelectronics. *Prog. Polym. Sci.* **2001,** *26* (1), 3-65.

83. Niinistö, L.; Nieminen, M.; Päiväsaari, J.; Niinistö, J.; Putkonen, M.; Nieminen, M., Advanced Electronic and Optoelectronic Materials by Atomic Layer Deposition: An Overview with Special Emphasis on Recent Progress in Processing of High-K Dielectrics and Other Oxide Materials. *Phys. Status Solidi A* **2004,** *201* (7), 1443-1452.

84. Chu, B.; Zhou, X.; Ren, K.; Neese, B.; Lin, M.; Wang, Q.; Bauer, F.; Zhang, Q., A Dielectric Polymer with High Electric Energy Density and Fast Discharge Speed. *Science* **2006,** *313* (5785), 334-336.

85. Chou, Y. H.; Chiu, Y. C.; Chen, W. C., High-K Polymer-Graphene Oxide Dielectrics for Low-Voltage Flexible Nonvolatile Transistor Memory Devices. *Chem. Commun.* **2014,** *50* (24), 3217-3219.

86. Hawkins, S. A.; Yao, H.; Wang, H.; Sue, H.-J., Tensile Properties and Electrical Conductivity of Epoxy Composite Thin Films Containing Zinc Oxide Quantum Dots and Multi-Walled Carbon Nanotubes. *Carbon* **2017,** *115*, 18-27.

87. Ortiz, R. P.; Facchetti, A.; Marks, T. J., High-K Organic, Inorganic, and Hybrid Dielectrics for Low-Voltage Organic Field-Effect Transistors. *Chem. Rev.* **2010,** *110* (1), 205-239.

88. Baeg, K. J.; Khim, D.; Jung, S. W.; Kang, M.; You, I. K.; Kim, D. Y.; Facchetti, A.; Noh, Y. Y., Remarkable Enhancement of Hole Transport in Top-Gated N-Type Polymer Field-Effect Transistors by a High-K Dielectric for Ambipolar Electronic Circuits. *Adv. Mater.* **2012,** *24* (40), 5433-5439.

89. Zhu, M.; Zhou, Z.; Gao, D., Silicon Electro-Optic Modulator with High-Permittivity Gate Dielectric Layer. *Chin. Opt. Lett.* **2009,** *7* (10), 924-925.

90. Zirkl, M.; Haase, A.; Fian, A.; Schön, H.; Sommer, C.; Jakopic, G.; Leising, G.; Stadlober, B.; Graz, I.; Gaar, N.; Schwödiauer, R.; Bauer-Gogonea, S.; Bauer, S., Low-Voltage Organic Thin-Film Transistors with High-K Nanocomposite Gate Dielectrics for Flexible Electronics and Optothermal Sensors. *Adv. Mater.* **2007,** *19* (17), 2241-2245.

91. Wu, C.; Huang, X. Y.; Wu, X. F.; Xie, L. Y.; Yang, K.; Jiang, P. K., Graphene Oxide-Encapsulated Carbon Nanotube Hybrids for High Dielectric Performance Nanocomposites with Enhanced Energy Storage Density. *Nanoscale* **2013,** *5* (9), 3847-3855.

92. Wu, Z.-S.; Sun, Y.; Tan, Y.-Z.; Yang, S.; Feng, X.; Müllen, K., Three-Dimensional Graphene-Based Macro- and Mesoporous Frameworks for High-Performance Electrochemical Capacitive Energy Storage. *J. Am. Chem. Soc.* **2012,** *134* (48), 19532-19535.

93. Rao, Y.; Ogitani, S.; Kohl, P.; Wong, C., Novel Polymer–Ceramic Nanocomposite Based on High Dielectric Constant Epoxy Formula for Embedded Capacitor Application. *J. Appl. Polym. Sci.* **2002,** *83* (5), 1084-1090.

94. Dang, Z. M.; Lin, Y. H.; Nan, C. W., Novel Ferroelectric Polymer Composites with High Dielectric Constants. *Adv. Mater.* **2003,** *15* (19), 1625-1629.

95. Huang, X.; Jiang, P.; Xie, L., Ferroelectric Polymer/Silver Nanocomposites with High Dielectric Constant and High Thermal Conductivity. *Appl. Phys. Lett.* **2009,** *95* (24), 242901.

96. He, F.; Lau, S.; Chan, H. L.; Fan, J., High Dielectric Permittivity and Low Percolation Threshold in Nanocomposites Based on Poly (Vinylidene Fluoride) and Exfoliated Graphite Nanoplates. *Adv. Mater.* **2009,** *21* (6), 710-715.

97. Arbatti, M.; Shan, X.; Cheng, Z. Y., Ceramic–Polymer Composites with High Dielectric Constant. *Adv. Mater.* **2007,** *19* (10), 1369-1372.

98. Arbatti, M.; Shan, X.; Cheng, Z.-Y., Ceramic–Polymer Composites with High Dielectric Constant. *Adv. Mater.* **2007,** *19* (10), 1369-1372.

99. Dang, Z.-M.; Yuan, J.-K.; Zha, J.-W.; Zhou, T.; Li, S.-T.; Hu, G.-H., Fundamentals, Processes and Applications of High-Permittivity Polymer–Matrix Composites. *Prog. Mater Sci.* **2012,** *57* (4), 660-723.

100. Dang, Z. M.; Wang, L.; Yin, Y.; Zhang, Q.; Lei, Q. Q., Giant Dielectric Permittivities in Functionalized Carbon - Nanotube/Electroactive - Polymer Nanocomposites. *Adv. Mater.* **2007,** *19* (6), 852-857.

101. Hirata, T.; Li, P.; Lei, F.; Hawkins, S.; Mullins, M. J.; Sue, H. J., Epoxy Nanocomposites with Reduced Coefficient of Thermal Expansion. *J. Appl. Polym. Sci.* **2019,** *136* (26), 47703.

102. Kim, H.; Miura, Y.; Macosko, C. W., Graphene/Polyurethane Nanocomposites for Improved Gas Barrier and Electrical Conductivity. *Chem. Mater.* **2010,** *22* (11), 3441-3450.

103. Jiao, Y.; Yuan, L.; Liang, G.; Gu, A., Facile Preparation and Origin of High-K Carbon Nanotube/Poly (Ether Imide)/Bismaleimide Composites through Controlling the Location and Distribution of Carbon Nanotubes. *J. Phys. Chem. C* **2014,** *118* (41), 24091-24101.

104. Wang, B.; Liang, G.; Jiao, Y.; Gu, A.; Liu, L.; Yuan, L.; Zhang, W., Two-Layer Materials of Polyethylene and a Carbon Nanotube/Cyanate Ester Composite with High Dielectric Constant and Extremely Low Dielectric Loss. *Carbon* **2013,** *54*, 224-233.

105. Baughman, R. H.; Zakhidov, A. A.; de Heer, W. A., Carbon Nanotubes--the Route toward Applications. *Science* **2002,** *297* (5582), 787-792.

106. Francis, E.; Ko, H. U.; Kim, J. W.; Kim, H. C.; Kalarikkal, N.; Varughese, K.; Kim, J.; Thomas, S., High-K Dielectric Percolative Nanocomposites Based on Multiwalled Carbon Nanotubes and Polyvinyl Chloride. *J. Mater. Chem. C* **2018,** *6* (30), 8152-8159.

107. Bauhofer, W.; Kovacs, J. Z., A Review and Analysis of Electrical Percolation in Carbon Nanotube Polymer Composites. *Compos. Sci. Technol.* **2009,** *69* (10), 1486-1498.

108. Fan, Z.; Luo, G.; Zhang, Z.; Zhou, L.; Wei, F., Electromagnetic and Microwave Absorbing Properties of Multi-Walled Carbon Nanotubes/Polymer Composites. *Mater. Sci. Eng., B* **2006,** *132* (1), 85-89.

109. Li, M.; Huang, X.; Wu, C.; Xu, H.; Jiang, P.; Tanaka, T., Fabrication of Two-Dimensional Hybrid Sheets by Decorating Insulating Pani on Reduced Graphene Oxide for Polymer Nanocomposites with Low Dielectric Loss and High Dielectric Constant. *J. Mater. Chem.* **2012,** *22* (44), 23477-23484.

110. Ago, H.; Petritsch, K.; Shaffer, M. S. P.; Windle, A. H.; Friend, R. H., Composites of Carbon Nanotubes and Conjugated Polymers for Photovoltaic Devices. *Adv. Mater.* **1999,** *11* (15), 1281-1285.

111. Zhang, Z.; Yuan, L.; Qiang, Z.; Liang, G.; Gu, A., Flame Retarding High-K Composites with Low Dielectric Loss Based on Unique Multifunctional Coated Multiwalled Carbon Nanotubes and Cyanate Ester. *Ind. Eng. Chem. Res.* **2015,** *54* (3), 938-948.

112. Qiang, Z.; Liang, G.; Gu, A.; Yuan, L., The Dielectric Behavior and Origin of High-K Composites with Very Low Percolation Threshold Based on Unique Multi-Branched Polyaniline/Carbon Nanotube Hybrids and Epoxy Resin. *Composites Part A* **2014,** *64*, 1-10.

113. Liu, H.; Shen, Y.; Song, Y.; Nan, C. W.; Lin, Y.; Yang, X., Carbon Nanotube Array/Polymer Core/Shell Structured Composites with High Dielectric Permittivity, Low Dielectric Loss, and Large Energy Density. *Adv. Mater.* **2011,** *23* (43), 5104-5108.

114. Lin, W.; Moon, K. S.; Wong, C., A Combined Process of in Situ Functionalization and Microwave Treatment to Achieve Ultrasmall Thermal Expansion of Aligned Carbon Nanotube–Polymer Nanocomposites: Toward Applications as Thermal Interface Materials. *Adv. Mater.* **2009,** *21* (23), 2421-2424.

115. Wu, Z.; Gao, S.; Chen, L.; Jiang, D.; Shao, Q.; Zhang, B.; Zhai, Z.; Wang, C.; Zhao, M.; Ma, Y.; Zhang, X.; Weng, L.; Zhang, M.; Guo, Z., Electrically Insulated

Epoxy Nanocomposites Reinforced with Synergistic Core–Shell SiO_2@MWCNTs and Montmorillonite Bifillers. *Macromol. Chem. Phys.* **2017,** *218* (23), 1700357.

116. Farhad, D.; Atif, A.; Amr, M. A.; Tan, Z.; Hung-Jue, S.; Mark, E. W., Porous SnO_2 –Cu_xO Nanocomposite Thin Film on Carbon Nanotubes as Electrodes for High Performance Supercapacitors. *Nanotechnology* **2019,** *30* (1), 015401.

117. Xu, N.; Zhang, Q.; Yang, H.; Xia, Y.; Jiang, Y., In-Situ Preparation of Hierarchical Flower-Like Tio2/Carbon Nanostructures as Fillers for Polymer Composites with Enhanced Dielectric Properties. *Sci. Rep.* **2017,** *7*, 43970.

118. Kausch‐Blecken von Schmeling, H. H.; Williams, J. G., Polymer Fracture. In *Encyclopedia of Polymer Science and Technology*, 2015; pp 1-65.

119. Ciprari, D.; Jacob, K.; Tannenbaum, R., Characterization of Polymer Nanocomposite Interphase and Its Impact on Mechanical Properties. *Macromolecules* **2006,** *39* (19), 6565-6573.

120. Ash, B. J.; Rogers, D. F.; Wiegand, C. J.; Schadler, L. S.; Siegel, R. W.; Benicewicz, B. C.; Apple, T., Mechanical Properties of Al_2O_3/Polymethylmethacrylate Nanocomposites. *Polym. Compos.* **2002,** *23* (6), 1014-1025.

121. Nguyen, H. K.; Sugimoto, S.; Konomi, A.; Inutsuka, M.; Kawaguchi, D.; Tanaka, K., Dynamics Gradient of Polymer Chains near a Solid Interface. *ACS Macro Lett.* **2019,** *8* (8), 1006-1011.

122. Kim, Y.-G.; Wagner, M.; Thérien-Aubin, H. l., Dynamics of Soft and Hairy Polymer Nanoparticles in a Suspension by Nmr Relaxation. *Macromolecules* **2020,** *53* (3), 844-851.

123. Hore, M. J., Polymers on Nanoparticles: Structure & Dynamics. *Soft Matter* **2019,** *15* (6), 1120-1134.

124. Abboud, M.; Turner, M.; Duguet, E.; Fontanille, M., Pmma-Based Composite Materials with Reactive Ceramic Fillers. Part 1.—Chemical Modification and Characterisation of Ceramic Particles. *J. Mater. Chem.* **1997,** *7* (8), 1527-1532.

125. Wang, S.; Wang, M.; Lei, Y.; Zhang, L., "Anchor Effect" in Poly (Styrene Maleic Anhydride)/TiO_2 Nanocomposites. *J. Mater. Sci. Lett.* **1999,** *18* (24), 2009-2012.

126. Caris, C. H.; Van Elven, L. P.; Van Herk, A. M.; German, A. L., Polymerization of Mma at the Surface of Inorganic Submicron Particles. *Br. Polym. J.* **1989,** *21* (2), 133-140.

127. von Werne, T.; Patten, T. E., Atom Transfer Radical Polymerization from Nanoparticles: A Tool for the Preparation of Well-Defined Hybrid Nanostructures and for Understanding the Chemistry of Controlled/"Living" Radical Polymerizations from Surfaces. *J. Am. Chem. Soc.* **2001,** *123* (31), 7497-7505.

128. Weimer, M. W.; Chen, H.; Giannelis, E. P.; Sogah, D. Y., Direct Synthesis of Dispersed Nanocomposites by in Situ Living Free Radical Polymerization Using a Silicate-Anchored Initiator. *J. Am. Chem. Soc.* **1999,** *121* (7), 1615-1616.

129. Tsubokawa, N.; Kogure, A.; Maruyama, K.; Sone, Y.; Shimomura, M., Graft Polymerization of Vinyl Monomers from Inorganic Ultrafine Particles Initiated by Azo Groups Introduced onto the Surface. *Polym. J.* **1990,** *22* (9), 827-833.

130. Chao, H.; Riggleman, R. A., Effect of Particle Size and Grafting Density on the Mechanical Properties of Polymer Nanocomposites. *Polymer* **2013,** *54* (19), 5222-5229.

131. Weon, J. I.; Gam, K. T.; Boo, W. J.; Sue, H. J.; Chan, C. M., Impact-Toughening Mechanisms of Calcium Carbonate-Reinforced Polypropylene Nanocomposite. *J. Appl. Polym. Sci.* **2006,** *99* (6), 3070-3076.

132. Lee, J.-Y.; Zhang, Q.; Emrick, T.; Crosby, A. J., Nanoparticle Alignment and Repulsion During Failure of Glassy Polymer Nanocomposites. *Macromolecules* **2006,** *39* (21), 7392-7396.

133. Balazs, A. C.; Emrick, T.; Russell, T. P., Nanoparticle Polymer Composites: Where Two Small Worlds Meet. *Science* **2006,** *314* (5802), 1107-1110.

134. Sue, H. J., Study of Rubber-Modified Brittle Epoxy Systems. Part I: Fracture Toughness Measurements Using the Double-Notch Four-Point-Bend Method. *Polym. Eng. Sci.* **1991,** *31* (4), 270-274.

135. Sue, H.-J.; Yee, A. F., Study of Fracture Mechanisms of Multiphase Polymers Using the Double-Notch Four-Point-Bending Method. *J. Mater. Sci.* **1993,** *28* (11), 2975-2980.

136. Song, Q.; Nataraj, S.; Roussenova, M. V.; Tan, J. C.; Hughes, D. J.; Li, W.; Bourgoin, P.; Alam, M. A.; Cheetham, A. K.; Al-Muhtaseb, S. A., Zeolitic Imidazolate Framework (ZIF-8) Based Polymer Nanocomposite Membranes for Gas Separation. *Energy Environ. Sci.* **2012,** *5* (8), 8359-8369.

137. Butkus, L. M.; Mathern, P. D.; Johnson, W. S., Tensile Properties and Plane-Stress Fracture Toughness of Thin Film Aerospace Adhesives. *J. Adhes.* **1998,** *66* (1-4), 251-273.

138. Sue, H.-J., Study of Rubber-Modified Brittle Epoxy Systems. Part I: Fracture Toughness Measurements Using the Double-Notch Four-Point-Bend Method. *Polym. Eng. Sci.* **1991,** *31* (4), 270-274.

139. Shimomura, O.; Maeno, K.; Ohtaka, A.; Yamaguchi, S.; Ichihara, J.; Sakamoto, K.; Nomura, R., Alkylamines-Intercalated A-Zirconium Phosphate as Latent Thermal Anionic Initiators. *J. Polym. Sci., Part A: Polym. Chem.* **2014,** *52* (13), 1854-1861.

140. Prentice, P., Influence of Molecular Weight on the Fracture of Poly (Methyl Methacrylate)(Pmma). *Polymer* **1983,** *24* (3), 344-350.

141. Andreozzi, L.; Faetti, M.; Giordano, M.; Zulli, F., Molecular-Weight Dependence of Enthalpy Relaxation of Pmma. *Macromolecules* **2005,** *38* (14), 6056-6067.

142. Du, F.; Fischer, J. E.; Winey, K. I., Effect of Nanotube Alignment on Percolation Conductivity in Carbon Nanotube/Polymer Composites. *Phys. Rev. B* **2005,** *72* (12), 121404.

143. Zhao, S.; Schadler, L. S.; Hillborg, H.; Auletta, T., Improvements and Mechanisms of Fracture and Fatigue Properties of Well-Dispersed Alumina/Epoxy Nanocomposites. *Compos. Sci. Technol.* **2008,** *68* (14), 2976-2982.

144. Aliha, M.; Bahmani, A.; Akhondi, S., Mixed Mode Fracture Toughness Testing of Pmma with Different Three-Point Bend Type Specimens. *Eur. J. Mech. A. Solids* **2016,** *58*, 148-162.

145. Ishikawa, M.; Ogawa, H.; Narisawa, I., Brittle Fracture in Glassy Polymers. *J. Macromol. Sci. Part B Phys.* **1981,** *19* (3), 421-443.

146. Choi, J.; Hui, C. M.; Pietrasik, J.; Dong, H.; Matyjaszewski, K.; Bockstaller, M. R., Toughening Fragile Matter: Mechanical Properties of Particle Solids Assembled from Polymer-Grafted Hybrid Particles Synthesized by Atrp. *Soft Matter* **2012,** *8* (15), 4072-4082.

147. Salehi Vaziri, H.; Abadyan, M.; Nouri, M.; Omaraei, I. A.; Sadredini, Z.; Ebrahimnia, M., Investigation of the Fracture Mechanism and Mechanical Properties of Polystyrene/Silica Nanocomposite in Various Silica Contents. *J. Mater. Sci.* **2011,** *46* (17), 5628-5638.

148. Donald, A. M.; Kramer, E. J., Craze Initiation and Growth in High-Impact Polystyrene. *J. Appl. Polym. Sci.* **1982,** *27* (10), 3729-3741.

149. Liu, J.; Sue, H.-J.; Thompson, Z. J.; Bates, F. S.; Dettloff, M.; Jacob, G.; Verghese, N.; Pham, H., Nanocavitation in Self-Assembled Amphiphilic Block Copolymer-Modified Epoxy. *Macromolecules* **2008,** *41* (20), 7616-7624.

150. Müller, K.; Bugnicourt, E.; Latorre, M.; Jorda, M.; Echegoyen Sanz, Y.; Lagaron, J. M.; Miesbauer, O.; Bianchin, A.; Hankin, S.; Bölz, U.; Pérez, G.; Jesdinszki, M.; Lindner, M.; Scheuerer, Z.; Castelló, S.; Schmid, M., Review on the Processing and Properties of Polymer Nanocomposites and Nanocoatings and Their Applications in the Packaging, Automotive and Solar Energy Fields. *Nanomaterials* **2017,** *7* (4), 74.

151. Ray, S. S.; Okamoto, M., Polymer/Layered Silicate Nanocomposites: A Review from Preparation to Processing. *Prog. Polym. Sci.* **2003,** *28* (11), 1539-1641.

152. Jordan, J.; Jacob, K. I.; Tannenbaum, R.; Sharaf, M. A.; Jasiuk, I., Experimental Trends in Polymer Nanocomposites—a Review. *Mater. Sci. Eng., A* **2005,** *393* (1-2), 1-11.

153. Huang, Z.-M.; Zhang, Y.-Z.; Kotaki, M.; Ramakrishna, S., A Review on Polymer Nanofibers by Electrospinning and Their Applications in Nanocomposites. *Compos. Sci. Technol.* **2003,** *63* (15), 2223-2253.

154. Beall, G. W.; Powell, C. E., *Fundamentals of Polymer-Clay Nanocomposites*. Cambridge University Press: 2011.

155. Okada, A.; Usuki, A., Twenty Years of Polymer-Clay Nanocomposites. *Macromol. Mater. Eng.* **2006,** *291* (12), 1449-1476.

156. Clearfield, A.; Stynes, J., The Preparation of Crystalline Zirconium Phosphate and Some Observations on Its Ion Exchange Behaviour. *J. Inorg. Nucl. Chem.* **1964,** *26* (1), 117-129.

157. Sue, H. J.; Gam, K. T.; Bestaoui, N.; Spurr, N.; Clearfield, A., Epoxy Nanocomposites Based on the Synthetic A-Zirconium Phosphate Layer Structure. *Chem. Mater.* **2004,** *16* (2), 242-249.

158. Boo, W. J.; Sun, L. Y.; Liu, J.; Clearfield, A.; Sue, H. J.; Mullins, M. J.; Pham, H., Morphology and Mechanical Behavior of Exfoliated Epoxy/A-Zirconium Phosphate Nanocomposites. *Compos. Sci. Technol.* **2007,** *67* (2), 262-269.

159. Sun, L.; Boo, W. J.; Sun, D.; Clearfield, A.; Sue, H.-J., Preparation of Exfoliated Epoxy/A-Zirconium Phosphate Nanocomposites Containing High Aspect Ratio Nanoplatelets. *Chem. Mater.* **2007,** *19* (7), 1749-1754.

160. Sun, L.; Boo, W. J.; Sue, H.-J.; Clearfield, A., Preparation of A-Zirconium Phosphate Nanoplatelets with Wide Variations in Aspect Ratios. *New J. Chem.* **2007,** *31* (1), 39-43.

161. Li, P.; White, K. L.; Lin, C.-H.; Kim, D.; Muliana, A.; Krishnamoorti, R.; Nishimura, R.; Sue, H.-J., Mechanical Reinforcement of Epoxy with Self-Assembled Synthetic Clay in Smectic Order. *ACS Appl. Mater. Interfaces* **2014,** *6* (13), 10188-10195.

162. Lei, F.; Hamdi, M.; Liu, P.; Li, P.; Mullins, M.; Wang, H.; Li, J.; Krishnamoorti, R.; Guo, S.; Sue, H.-J., Scratch Behavior of Epoxy Coating Containing Self-Assembled Zirconium Phosphate Smectic Layers. *Polymer* **2017,** *112*, 252-263.

163. Ooi, S.; Cook, W.; Simon, G.; Such, C., Dsc Studies of the Curing Mechanisms and Kinetics of Dgeba Using Imidazole Curing Agents. *Polymer* **2000,** *41* (10), 3639-3649.

164. Wong, F. F.; Lin, C. M.; Chen, K.-L.; Shen, Y.-H.; Huang, J.-J., Improvement of the Thermal Latency for Epoxy-Phenolic Resins by Novel Amphiphatic Imidazole Catalysts. *Macromol. Res.* **2010,** *18* (4), 324-330.

165. Shimomura, O.; Maeno, K.; Ohtaka, A.; Yamaguchi, S.; Ichihara, J.; Sakamoto, K.; Nomura, R., Alkylamines-Intercalated A-Zirconium Phosphate as Latent Thermal Anionic Initiators. *J. Polym. Sci., Part A: Polym. Chem.* **2014,** *52* (13), 1854-1861.

166. Shimomura, O.; Tokizane, K.; Nishisako, T.; Yamaguchi, S.; Ichihara, J.; Kirino, M.; Ohtaka, A.; Nomura, R., Imidazoles-Intercalated A-Zirconium Phosphate as Latent Thermal Initiators in the Reaction of Glycidyl Phenyl Ether (Gpe) and Hexahydro-4-Methylphthalic Anhydride (Mhhpa). *Catalysts* **2017,** *7* (6), 172.

167. Kisch, H.; Millini, R.; Wang, I.-J., Bifunktionelle Katalysatoren Zur Synthese Cyclischer Carbonate Aus Oxiranen Und Kohlendioxid. *Chem. Ber.* **1986,** *119* (3), 1090-1094.

168. Nishikubo, T.; Kameyama, A.; Yamashita, J.; Tomoi, M.; Fukuda, W., Insoluble Polystyrene-Bound Quaternary Onium Salt Catalysts for the Synthesis of Cyclic Carbonates by the Reaction of Oxiranes with Carbon Dioxide. *J. Polym. Sci., Part A: Polym. Chem.* **1993,** *31* (4), 939-947.

169. Kissinger, H. E., Reaction Kinetics in Differential Thermal Analysis. *Anal. Chem.* **1957,** *29* (11), 1702-1706.

170. Mosby, B. M.; Díaz, A.; Clearfield, A., Surface Modification of Layered Zirconium Phosphates: A Novel Pathway to Multifunctional Materials. *Dalton Trans.* **2014,** *43* (27), 10328-10339.

171. Mosby, B. M.; Díaz, A.; Bakhmutov, V.; Clearfield, A., Surface Functionalization of Zirconium Phosphate Nanoplatelets for the Design of Polymer Fillers. *ACS Appl. Mater. Interfaces* **2014,** *6* (1), 585-592.

172. Boo, W.; Sun, L.; Liu, J.; Clearfield, A.; Sue, H.-J.; Mullins, M.; Pham, H., Morphology and Mechanical Behavior of Exfoliated Epoxy/A-Zirconium Phosphate Nanocomposites. *Compos. Sci. Technol.* **2007,** *67* (2), 262-269.

173. Liu, C.; Mullins, M.; Hawkins, S.; Kotaki, M.; Sue, H.-J., Epoxy Nanocomposites Containing Zeolitic Imidazolate Framework-8. *ACS Appl. Mater. Interfaces* **2018,** *10* (1), 1250-1257.

174. Han, J.; Gee, R. H.; Boyd, R. H., Glass Transition Temperatures of Polymers from Molecular Dynamics Simulations. *Macromolecules* **1994,** *27* (26), 7781-7784.

175. Brown, D.; Mele, P.; Marceau, S.; Alberola, N., A Molecular Dynamics Study of a Model Nanoparticle Embedded in a Polymer Matrix. *Macromolecules* **2003,** *36* (4), 1395-1406.

176. Lai, M.; Friedrich, K.; Botsis, J.; Burkhart, T., Evaluation of Residual Strains in Epoxy with Different Nano/Micro-Fillers Using Embedded Fiber Bragg Grating Sensor. *Compos. Sci. Technol.* **2010,** *70* (15), 2168-2175.

177. Zilg, C.; Mülhaupt, R.; Finter, J., Morphology and Toughness/Stiffness Balance of Nanocomposites Based Upon Anhydride-Cured Epoxy Resins and Layered Silicates. *Macromol. Chem. Phys.* **1999,** *200* (3), 661-670.

178. Rotzinger, B. P.; Chanzy, H. D.; Smith, P., High Strength/High Modulus Polyethylene: Synthesis and Processing of Ultra-High Molecular Weight Virgin Powders. *Polymer* **1989,** *30* (10), 1814-1819.

179. Zilg, C.; Dietsche, F.; Hoffmann, B.; Dietrich, C.; Mühlhaupt, R. In *Nanofillers Based Upon Organophilic Layered Silicates*, Macromol. Symp., Wiley Online Library: 2001; pp 65-77.

180. Kim, G. M.; Michler, G.; Rösch, J.; Mülhaupt, R., Micromechanical Deformation Processes in Toughened Pp/Pa/Sebs-G-Ma Blends Prepared by Reactive Processing. *Acta Polym.* **1998,** *49* (2-3), 88-95.

181. Hashemi, S.; Williams, J. G., Size and Loading Mode Effects in Fracture Toughness Testing of Polymers. *J. Mater. Sci.* **1984,** *19* (11), 3746-3759.

182. Sue, H.-J.; Yee, A. F., Micromechanical Modeling of Crack-Tip Rubber Particle Cavitational Process in Polymer Toughening. *Polym. Eng. Sci.* **1996,** *36* (18), 2320-2326.

183. Pearson, R. A.; Yee, A. F., Toughening Mechanisms in Elastomer-Modified Epoxies. *J. Mater. Sci.* **1989,** *24* (7), 2571-2580.

184. Liu, J.; Sue, H.-J.; Thompson, Z. J.; Bates, F. S.; Dettloff, M.; Jacob, G.; Verghese, N.; Pham, H., Effect of Crosslink Density on Fracture Behavior of Model Epoxies Containing Block Copolymer Nanoparticles. *Polymer* **2009,** *50* (19), 4683-4689.

185. Yee, A. F.; Pearson, R. A., Toughening Mechanisms in Elastomer-Modified Epoxies. *J. Mater. Sci.* **1986,** *21* (7), 2462-2474.

186. Farha, O. K.; Yazaydın, A. Ö.; Eryazici, I.; Malliakas, C. D.; Hauser, B. G.; Kanatzidis, M. G.; Nguyen, S. T.; Snurr, R. Q.; Hupp, J. T., De Novo Synthesis of a Metal–Organic Framework Material Featuring Ultrahigh Surface Area and Gas Storage Capacities. *Nat. Chem.* **2010,** *2* (11), 944-948.

187. Bae, T. H.; Lee, J. S.; Qiu, W.; Koros, W. J.; Jones, C. W.; Nair, S., A High - Performance Gas - Separation Membrane Containing Submicrometer - Sized Metal – Organic Framework Crystals. *Angew. Chem., Int. Ed.* **2010,** *49* (51), 9863-9866.

188. García-García, P.; Müller, M.; Corma, A., MOF Catalysis in Relation to Their Homogeneous Counterparts and Conventional Solid Catalysts. *Chem. Sci.* **2014,** *5* (8), 2979-3007.

189. Horcajada, P.; Chalati, T.; Serre, C.; Gillet, B.; Sebrie, C.; Baati, T.; Eubank, J. F.; Heurtaux, D.; Clayette, P.; Kreuz, C., Porous Metal-Organic-Framework Nanoscale Carriers as a Potential Platform for Drug Delivery and Imaging. *Nat. Mater.* **2010,** *9* (2), 172-178.

190. Ma, D.; Li, B.; Zhou, X.; Zhou, Q.; Liu, K.; Zeng, G.; Li, G.; Shi, Z.; Feng, S., A Dual Functional MOF as a Luminescent Sensor for Quantitatively Detecting the Concentration of Nitrobenzene and Temperature. *Chem. Commun.* **2013,** *49* (79), 8964-8966.

191. Sadakiyo, M.; Yamada, T.; Kitagawa, H., Rational Designs for Highly Proton-Conductive Metal− Organic Frameworks. *J. Am. Chem. Soc.* **2009,** *131* (29), 9906-9907.

192. Tien-Binh, N.; Vinh-Thang, H.; Chen, X. Y.; Rodrigue, D.; Kaliaguine, S., Crosslinked MOF-Polymer to Enhance Gas Separation of Mixed Matrix Membranes. *J. Membr. Sci.* **2016,** *520* (Supplement C), 941-950.

193. Yu, S.; Li, S.; Huang, S.; Zeng, Z.; Cui, S.; Liu, Y., Covalently Bonded Zeolitic Imidazolate Frameworks and Polymers with Enhanced Compatibility in Thin Film Nanocomposite Membranes for Gas Separation. *J. Membr. Sci.* **2017,** *540* (Supplement C), 155-164.

194. Yaghi, O. M. *Metal-Organic and Zeolite Imidazolate Frameworks (MOFs and Zifs) for Highly Selective Separations*; University of California-Los Angeles: 2012.

195. Park, K. S.; Ni, Z.; Côté, A. P.; Choi, J. Y.; Huang, R.; Uribe-Romo, F. J.; Chae, H. K.; O'Keeffe, M.; Yaghi, O. M., Exceptional Chemical and Thermal Stability of Zeolitic Imidazolate Frameworks. *Proc. Natl. Acad. Sci. U. S. A.* **2006,** *103* (27), 10186-10191.

196. Kwon, H. T.; Jeong, H.-K., In Situ Synthesis of Thin Zeolitic–Imidazolate Framework ZIF-8 Membranes Exhibiting Exceptionally High Propylene/Propane Separation. *J. Am. Chem. Soc.* **2013,** *135* (29), 10763-10768.

197. Eslava, S.; Zhang, L.; Esconjauregui, S.; Yang, J.; Vanstreels, K.; Baklanov, M. R.; Saiz, E., Metal-Organic Framework ZIF-8 Films as Low-K Dielectrics in Microelectronics. *Chem. Mater.* **2012,** *25* (1), 27-33.

198. Mahdi, E.; Tan, J.-C., Mixed-Matrix Membranes of Zeolitic Imidazolate Framework (ZIF-8)/Matrimid Nanocomposite: Thermo-Mechanical Stability and Viscoelasticity Underpinning Membrane Separation Performance. *J. Membr. Sci.* **2016,** *498*, 276-290.

199. Pan, Y.; Liu, Y.; Zeng, G.; Zhao, L.; Lai, Z., Rapid Synthesis of Zeolitic Imidazolate Framework-8 (ZIF-8) Nanocrystals in an Aqueous System. *Chem. Commun.* **2011,** *47* (7), 2071-2073.

200. Heise, M.; Martin, G., Curing Mechanism and Thermal Properties of Epoxy-Imidazole Systems. *Macromolecules* **1989,** *22* (1), 99-104.

201. Manju; Roy, P. K.; Ramanan, A., Toughening of Epoxy Resin Using Zn4o (1,4-Benzenedicarboxylate)3 Metal-Organic Frameworks. *RSC Adv.* **2014,** *4* (94), 52338-52345.

202. Wang, N.; Zhang, Y.; Chen, J.; Zhang, J.; Fang, Q., Dopamine Modified Metal-Organic Frameworks on Anti-Corrosion Properties of Waterborne Epoxy Coatings. *Prog. Org. Coat.* **2017,** *109*, 126-134.

203. Venna, S. R.; Carreon, M. A., Highly Permeable Zeolite Imidazolate Framework-8 Membranes for CO_2/CH_4 Separation. *J. Am. Chem. Soc.* **2009,** *132* (1), 76-78.

204. Liu, C.; Zhang, G.; Zhao, C.; Li, X.; Li, M.; Na, H., MOFs Synthesized by the Ionothermal Method Addressing the Leaching Problem of Il-Polymer Composite Membranes. *Chem. Commun.* **2014,** *50* (91), 14121-14124.

205. Farkas, A.; Strohm, P. F., Imidazole Catalysis in the Curing of Epoxy Resins. *J. Appl. Polym. Sci.* **1968,** *12* (1), 159-168.

206. He, F.; Chen, G.; Zhou, Y.; Yu, Y.; Li, L.; Hao, S.; Liu, B., ZIF-8 Derived Carbon (C-ZIF) as a Bifunctional Electron Acceptor and Her Cocatalyst for G-C3n4:

Construction of a Metal-Free, All Carbon-Based Photocatalytic System for Efficient Hydrogen Evolution. *J. Mater. Chem. A* **2016,** *4* (10), 3822-3827.

207. Paul, D.; Robeson, L., Polymer Nanotechnology: Nanocomposites. *Polymer* **2008,** *49* (15), 3187-3204.

208. Jia, Q.; Zheng, M.; Zhu, Y.; Li, J.; Xu, C., Effects of Organophilic Montmorillonite on Hydrogen Bonding, Free Volume and Glass Transition Temperature of Epoxy Resin/Polyurethane Interpenetrating Polymer Networks. *Eur. Polym. J.* **2007,** *43* (1), 35-42.

209. Oh, I.-H.; Nomura, N.; Masahashi, N.; Hanada, S., Mechanical Properties of Porous Titanium Compacts Prepared by Powder Sintering. *Scr. Mater.* **2003,** *49* (12), 1197-1202.

210. Madsen, B.; Lilholt, H., Physical and Mechanical Properties of Unidirectional Plant Fibre Composites—an Evaluation of the Influence of Porosity. *Compos. Sci. Technol.* **2003,** *63* (9), 1265-1272.

211. Tan, J. C.; Bennett, T. D.; Cheetham, A. K., Chemical Structure, Network Topology, and Porosity Effects on the Mechanical Properties of Zeolitic Imidazolate Frameworks. *Proc. Natl. Acad. Sci. U. S. A.* **2010,** *107* (22), 9938-9943.

212. Rao, Y.; Qu, J.; Marinis, T.; Wong, C., A Precise Numerical Prediction of Effective Dielectric Constant for Polymer-Ceramic Composite Based on Effective-Medium Theory. *IEEE Trans. Compon. Packag. Technol.* **2000,** *23* (4), 680-683.

213. Yoon, D.-H.; Zhang, J.; Lee, B. I., Dielectric Constant and Mixing Model of Batio 3 Composite Thick Films. *Mater. Res. Bull.* **2003,** *38* (5), 765-772.

214. Koledintseva, M. Y.; DuBroff, R. E.; Schwartz, R. W., A Maxwell Garnett Model for Dielectric Mixtures Containing Conducting Particles at Optical Frequencies. *Prog. Electromagn. Res.* **2006,** *63*, 223-242.

215. Karkkainen, K.; Sihvola, A.; Nikoskinen, K., Analysis of a Three-Dimensional Dielectric Mixture with Finite Difference Method. *IEEE Trans. Geosci. Remote Sens.* **2001,** *39* (5), 1013-1018.

216. Uematsu, M.; Frank, E., Static Dielectric Constant of Water and Steam. *J. Phys. Chem. Ref. Data* **1980,** *9* (4), 1291-1306.

217. Zhang, K.; Lively, R. P.; Zhang, C.; Chance, R. R.; Koros, W. J.; Sholl, D. S.; Nair, S., Exploring the Framework Hydrophobicity and Flexibility of ZIF-8: From Biofuel Recovery to Hydrocarbon Separations. *J. Phys. Chem. Lett.* **2013,** *4* (21), 3618-3622.

218. Zhang, C.; Dai, Y.; Johnson, J. R.; Karvan, O.; Koros, W. J., High Performance ZIF-8/6fda-Dam Mixed Matrix Membrane for Propylene/Propane Separations. *J. Membr. Sci.* **2012,** *389*, 34-42.

219. Li, Q.; Chen, L.; Gadinski, M. R.; Zhang, S.; Zhang, G.; Li, H. U.; Iagodkine, E.; Haque, A.; Chen, L.-Q.; Jackson, T. N.; Wang, Q., Flexible High-Temperature Dielectric Materials from Polymer Nanocomposites. *Nature* **2015,** *523*, 576.

220. Chu, B.; Zhou, X.; Ren, K.; Neese, B.; Lin, M.; Wang, Q.; Bauer, F.; Zhang, Q. M., A Dielectric Polymer with High Electric Energy Density and Fast Discharge Speed. *Science* **2006,** *313* (5785), 334-336.

221. Zhang, Z.; Liao, M.; Lou, H.; Hu, Y.; Sun, X.; Peng, H., Conjugated Polymers for Flexible Energy Harvesting and Storage. *Adv. Mater.* **2018,** *30* (13), 1704261.

222. Zhang, D.; Liu, W.; Tang, L.; Zhou, K.; Luo, H., High Performance Capacitors Via Aligned TiO_2 Nanowire Array. *Appl. Phys. Lett.* **2017,** *110* (13), 133902.

223. Dang, Z.-M.; Yuan, J.-K.; Yao, S.-H.; Liao, R.-J., Flexible Nanodielectric Materials with High Permittivity for Power Energy Storage. *Adv. Mater.* **2013,** *25* (44), 6334-6365.

224. Brochu, P.; Pei, Q. B., Advances in Dielectric Elastomers for Actuators and Artificial Muscles. *Macromol. Rapid Commun.* **2010,** *31* (1), 10-36.

225. Zhu, L.; Wang, Q., Novel Ferroelectric Polymers for High Energy Density and Low Loss Dielectrics. *Macromolecules* **2012,** *45* (7), 2937-2954.

226. Yang, C.; Lin, Y.; Nan, C. W., Modified Carbon Nanotube Composites with High Dielectric Constant, Low Dielectric Loss and Large Energy Density. *Carbon* **2009,** *47* (4), 1096-1101.

227. Chang, J.; Liang, G.; Gu, A.; Cai, S.; Yuan, L., The Production of Carbon Nanotube/Epoxy Composites with a Very High Dielectric Constant and Low Dielectric Loss by Microwave Curing. *Carbon* **2012,** *50* (2), 689-698.

228. Zeraati, A. S.; Mirkhani, S. A.; Sundararaj, U., Enhanced Dielectric Performance of Polymer Nanocomposites Based on CNT/MnO_2 Nanowire Hybrid Nanostructure. *J. Phys. Chem. C* **2017,** *121* (15), 8327-8334.

229. Yousefi, N.; Sun, X. Y.; Lin, X. Y.; Shen, X.; Jia, J. J.; Zhang, B.; Tang, B. Z.; Chan, M. S.; Kim, J. K., Highly Aligned Graphene/Polymer Nanocomposites with Excellent Dielectric Properties for High-Performance Electromagnetic Interference Shielding. *Adv. Mater.* **2014,** *26* (31), 5480-5487.

230. Zhu, L., Exploring Strategies for High Dielectric Constant and Low Loss Polymer Dielectrics. *J. Phys. Chem. Lett.* **2014,** *5* (21), 3677-3687.

231. Sandler, J.; Kirk, J.; Kinloch, I.; Shaffer, M.; Windle, A., Ultra-Low Electrical Percolation Threshold in Carbon-Nanotube-Epoxy Composites. *Polymer* **2003,** *44* (19), 5893-5899.

232. Liu, J.; Xiao, T.; Liao, K.; Wu, P., Interfacial Design of Carbon Nanotube Polymer Composites: A Hybrid System of Noncovalent and Covalent Functionalizations. *Nanotechnology* **2007,** *18* (16), 165701.

233. Gorga, R. E.; Lau, K. K.; Gleason, K. K.; Cohen, R. E., The Importance of Interfacial Design at the Carbon Nanotube/Polymer Composite Interface. *J. Appl. Polym. Sci.* **2006,** *102* (2), 1413-1418.

234. James, S. L., Metal-Organic Frameworks. *Chem. Soc. Rev.* **2003,** *32* (5), 276-288.

235. Huang, G.; Zhang, F.; Du, X.; Qin, Y.; Yin, D.; Wang, L., Metal Organic Frameworks Route to in Situ Insertion of Multiwalled Carbon Nanotubes in Co3o4 Polyhedra as Anode Materials for Lithium-Ion Batteries. *ACS Nano* **2015,** *9* (2), 1592-1599.

236. Petit, C.; Bandosz, T. J., MOF–Graphite Oxide Composites: Combining the Uniqueness of Graphene Layers and Metal–Organic Frameworks. *Adv. Mater.* **2009,** *21* (46), 4753-4757.

237. Bristow, J. K.; Butler, K. T.; Svane, K. L.; Gale, J. D.; Walsh, A., Chemical Bonding at the Metal-Organic Framework/Metal Oxide Interface: Simulated Epitaxial Growth of MOF-5 on Rutile TiO_2. *J. Mater. Chem. A* **2017,** *5* (13), 6226-6232.

238. Dadfarnia, S.; Haji Shabani, A. M.; Moradi, S. E.; Emami, S., Methyl Red Removal from Water by Iron Based Metal-Organic Frameworks Loaded onto Iron Oxide Nanoparticle Adsorbent. *Appl. Surf. Sci.* **2015,** *330*, 85-93.

239. Sanchez, C.; Julián, B.; Belleville, P.; Popall, M., Applications of Hybrid Organic–Inorganic Nanocomposites. *J. Mater. Chem.* **2005,** *15* (35-36), 3559-3592.

240. Li, X.; Hao, C.; Tang, B.; Wang, Y.; Liu, M.; Wang, Y.; Zhu, Y.; Lu, C.; Tang, Z., Supercapacitor Electrode Materials with Hierarchically Structured Pores from Carbonization of MWCNTs and ZIF-8 Composites. *Nanoscale* **2017,** *9* (6), 2178-2187.

241. Wang, Y.; Chen, B.; Zhang, Y.; Fu, L.; Zhu, Y.; Zhang, L.; Wu, Y., ZIF-8@ MWCNT-Derived Carbon Composite as Electrode of High Performance for Supercapacitor. *Electrochim. Acta* **2016,** *213*, 260-269.

242. Abdi, J.; Vossoughi, M.; Mahmoodi, N. M.; Alemzadeh, I., Synthesis of Metal-Organic Framework Hybrid Nanocomposites Based on Go and CNT with High Adsorption Capacity for Dye Removal. *Chem. Eng. J.* **2017,** *326*, 1145-1158.

243. Ellis, J. E.; Zeng, Z.; Hwang, S. I.; Li, S.; Luo, T.-Y.; Burkert, S. C.; White, David L.; Rosi, N. L.; Gassensmith, J. J.; Star, A., Growth of ZIF-8 on Molecularly Ordered 2-Methylimidazole/Single-Walled Carbon Nanotubes to Form Highly Porous, Electrically Conductive Composites. *Chem. Sci.* **2019,** *10* (3), 737-742.

244. Sun, D.; Wong, M.; Sun, L.; Li, Y.; Miyatake, N.; Sue, H.-J., Purification and Stabilization of Colloidal Zno Nanoparticles in Methanol. *J. Sol-Gel Sci. Technol.* **2007,** *43* (2), 237-243.

245. Monti, M.; Armentano, I.; Faiella, G.; Antonucci, V.; Kenny, J. M.; Torre, L.; Giordano, M., Toward the Microstructure–Properties Relationship in MWCNT/Epoxy Composites: Percolation Behavior and Dielectric Spectroscopy. *Compos. Sci. Technol.* **2014,** *96*, 38-46.

246. Vo, L. T.; Anastasiadis, S. H.; Giannelis, E. P., Dielectric Study of Poly(Styrene-Co-Butadiene) Composites with Carbon Black, Silica, and Nanoclay. *Macromolecules* **2011,** *44* (15), 6162-6171.

247. Liu, Y. L.; Tang, Z. Y., Multifunctional Nanoparticle@MOF Core-Shell Nanostructures. *Adv. Mater.* **2013,** *25* (40), 5819-5825.

248. Kan, Y. W.; Clearfield, A., Zirconium Phosphate Supported MOF Nanoplatelets. *Inorg. Chem.* **2016,** *55* (11), 5634-5639.

249. Liu, J.; Wang, Z.; Zhao, Y.; Cheng, H. H.; Hu, C. G.; Jiang, L.; Qu, L. T., Three-Dimensional Graphene-Polypyrrole Hybrid Electrochemical Actuator. *Nanoscale* **2012,** *4* (23), 7563-7568.

250. Hou, L. M.; Wang, L.; Zhang, N.; Xie, Z. G.; Dong, D. W., Polymer Brushes on Metal-Organic Frameworks by Uv-Induced Photopolymerization. *Polym. Chem.* **2016,** *7* (37), 5828-5834.

251. Campbell, J.; Székely, G.; Davies, R.; Braddock, D. C.; Livingston, A. G., Fabrication of Hybrid Polymer/Metal Organic Framework Membranes: Mixed Matrix Membranes Versus in Situ Growth. *J. Mater. Chem. A* **2014,** *2* (24), 9260-9271.

252. Zhang, Y.; Feng, X.; Yuan, S.; Zhou, J.; Wang, B., Challenges and Recent Advances in MOF–Polymer Composite Membranes for Gas Separation. *Inorg. Chem. Front.* **2016,** *3* (7), 896-909.

APPENDIX A

SUPPLEMENTARY MATERIAL FOR SECTION 3

Determination of ligand exchange yield on the surface

A ZIF-8 particle is simplified as a cube, and the exposed surfaces are terminated with 2-methylimidazole (IMI) molecules. The side length of a unit cell is 1.6993 nm based on the literature. The average particle facet length of ZIF-8 was roughly 50 nm as determined by SEM and TEM.

The volume of the unit cell is calculated by

$$(1.6993\ \text{nm})^3 = 4.91\ nm^3/unit\ cell$$

The volume of each particle was calculated by (volume of a cube):

$$(50\ \text{nm})^3 = 1.25 \times 10^5\ nm^3/particle$$

Therefore, the number of IMI in each particle is calculated by

$$\frac{1.25 \times 10^5\ nm^3/particle \times 6\ IMI/unit\ cell}{4.91\ nm^3/unit\ cell} = 1.53 \times 10^5\ IMI/particle$$

The mole ratio of 2-methylimidazole (IMI) to 1,2-dimethylimidazole (DMI) in ZIF-8 is 1:49 as determined by NMR (Figure A-1). The number of DMI is calculated by

$$1.53 \times 10^5\ IMI/particle \div 49 = 3.12 \times 10^3\ DMI/particle$$

The surface area of each particle is given by:

$$(50\ \text{nm})^2 \times 6 = 1.5 \times 10^4\ nm^2/particle$$

The surface area of one face of unit cell is given by:

$$(1.6993\ \text{nm})^2 = 2.89\ nm^2/unit\ cell$$

Therefore, surface exposed 2-methylimidazole is calculated by:

$$\frac{1.5 \times 10^4\ nm^2/particle \times\ IMI/surface}{2.89\ nm^2/unit\ cell} = 5.19 \times 10^3\ IMI/particle\ surface$$

Considering that DMI is located on the surface, the mole ratio of IMI on the surface to DMI on the surface is calculated by;

$$\frac{3.12 \times 10^3\ DMI/particle\ surface}{5.19 \times 10^4\ IMI/particle\ surface} \times 100 = 60\%$$

Therefore, the conversion of DMI on the particle surface is around 60 %.

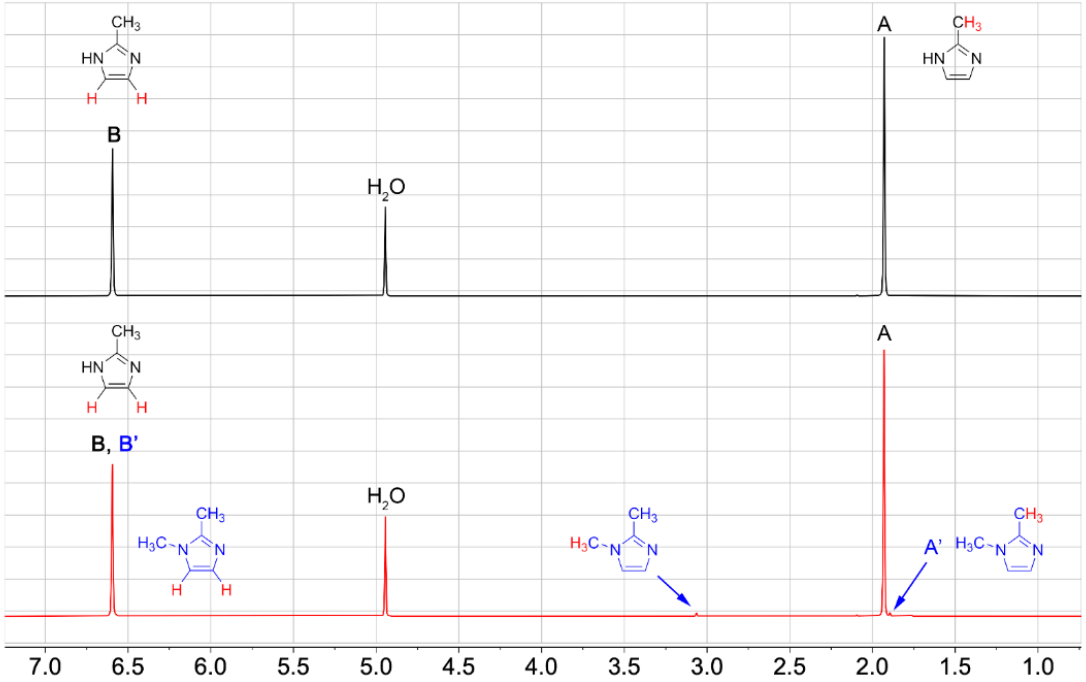

Figure A-1. NMR spectra of ZIF-8 (top) and ZIF-8-DMI (bottom) after digestion.

The areal density of IMI on the surface is calculated by;

$$\frac{5.19 \times 10^3\ IMI/particle\ surface}{1.5 \times 10^4\ nm^2/particle} = 0.35\ IMI/nm^2$$

The areal density of available IMI on ZIF-8-DMI surface is determined to be:

$$\frac{2.07 \times 10^3\ DMI/particle\ surface}{1.5 \times 10^4\ nm^2/particle} = 0.14\ IMI/nm^2$$

The conversion of DMI in the ZIF-8-DMI was calculated based on the peak area of 3.06 ppm from the hydrogen peak of N-methyl group in DMI and peak area of 1.94 ppm of hydrogen peak of 2-methyl in IMI and DMI. DMI conversion was calculated via the equation below:

$$\frac{H_{DMI}}{H_{DMI} + H_{IMI}} = \frac{H_{3.06}}{H_{1.94}} = \frac{1}{50}; \qquad \therefore \frac{H_{DMI}}{H_{DMI}} = \frac{1}{49}$$

Polymer mass fraction from TGA

The molar mass of ZIF-8 is 227.6 g/mol. Avogadro constant is denoted as N_A.

The mass of a ZIF-8 particle is calculated by:

$$\frac{227.6\ \text{g/mol} \times 0.5 \times 6.11 \times 10^5\ IMI/particle}{N_A} = 1.155 \times 10^{-16} g/particle$$

The mass of a grafting polymer is given by:

ZIF-8-SC-HGD:

$$\frac{0.3/0.7 \times 1.155 \times 10^{-16} g/particle}{5.19 \times 10^3\ polymer/particle} = 9.54 \times 10^{-21} g/polymer$$

ZIF-8-LC-LGD:

$$\frac{0.5/0.5 \times 1.155 \times 10^{-16} g/particle}{2.07 \times 10^3\ polymer/particle} = 5.58 \times 10^{-20} g/polymer$$

ZIF-8-LC-HGD:

$$\frac{0.72/0.25 \times 1.155 \times 10^{-16} g/particle}{5.19 \times 10^{3}\ polymer/particle} = 6.68 \times 10^{-20} g/polymer$$

The molar mass of a grafting polymer is given by:

$9.54 \times 10^{-21} g/polymer \times N_A = 5.74 \times 10^{3} g/mol$ ZIF-8-SC-HGD

$5.58 \times 10^{-20} g/polymer \times N_A = 3.36 \times 10^{4} g/mol$ ZIF-8-LC-LGD

$6.68 \times 10^{-20} g/polymer \times N_A = 4 \times 10^{4} g/mol$ ZIF-8-LC-HGD

APPENDIX B

SUPPLEMENTARY MATERIAL FOR SECTION 4

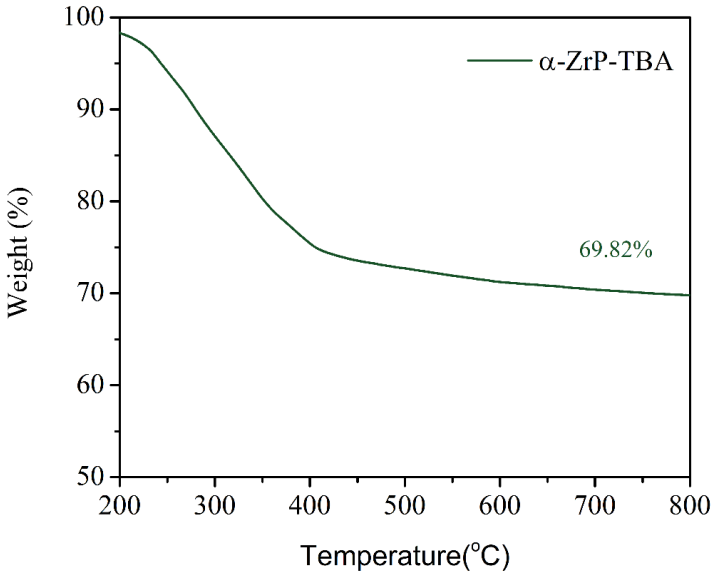

Figure B-1. TGA curve of α-ZrP-TBA nanoplatelets.

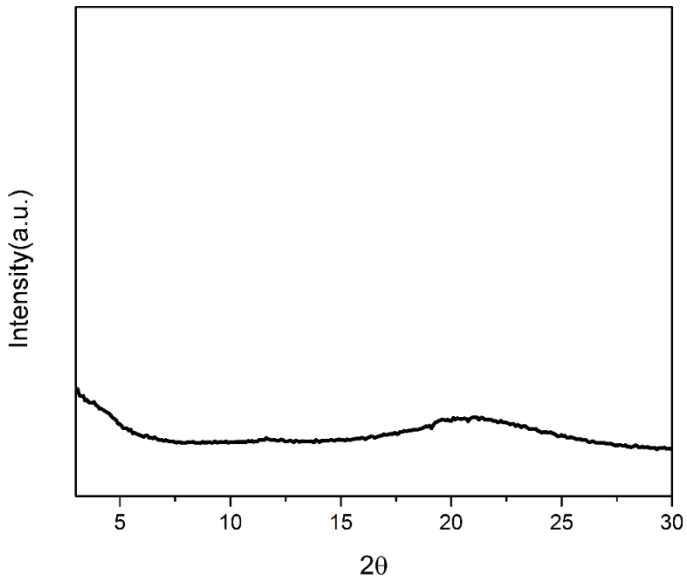

Figure B-2. XRD pattern of epoxy/α-ZrP-TBA nanocomposite.

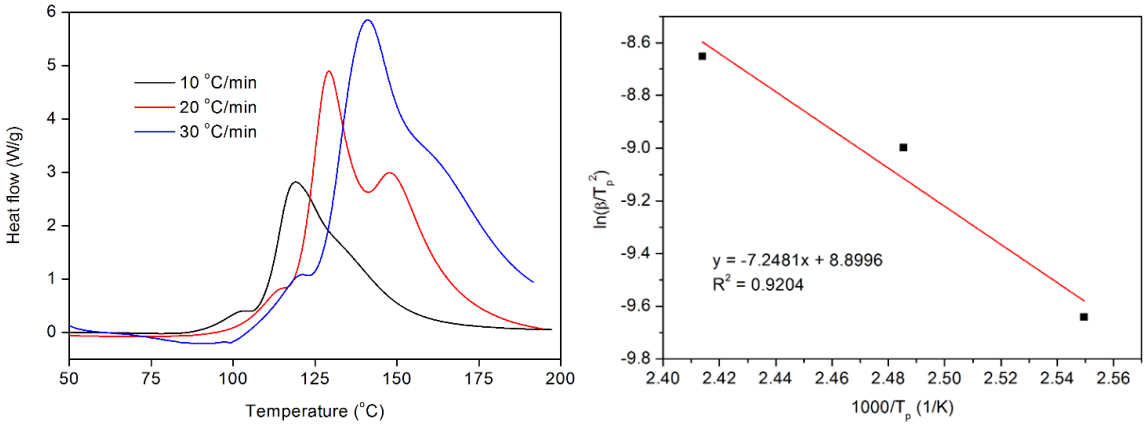

Figure B-3. DSC curves of epoxy/2MI at various scanning rates (top) and the fitted linear function $ln(\beta/T_p^2)$ vs. $1/T_p$ (bottom).

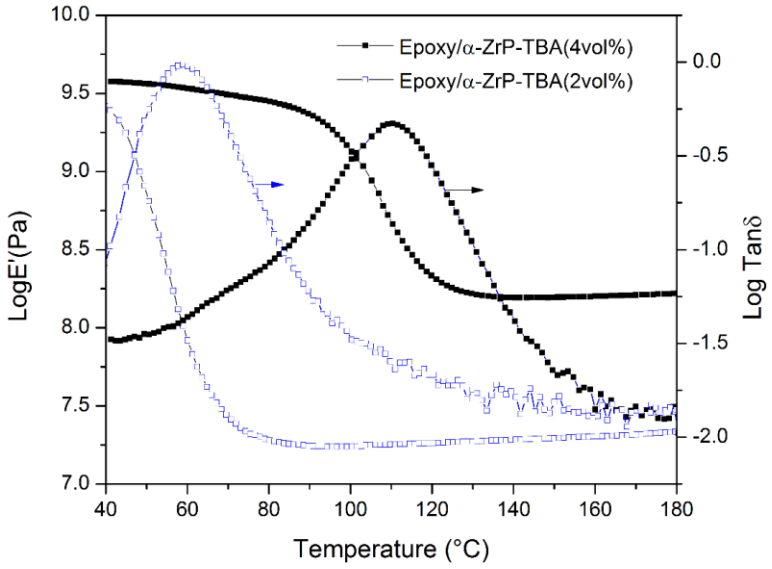

Figure B-4. DMA plots of epoxy/α-ZrP-TBA(4 vol%) and epoxy/α-ZrP-TBA(2 vol%) nanocomposites.

Table B-1. Young's Modulus and T_g of epoxy/α-ZrP-M1000 (4 vol%) and epoxy/α-ZrP-TBA (4 vol%) nanocomposites.[1]

Samples	**Young's Modulus (GPa)**	**T_g (°C)**
Epoxy/α-ZrP-M1000	3.2±0.5	79
Epoxy/α-ZrP-TBA	4.3±0.1	110

[1]. F. Lei, M. Hamdi, P. Liu, P. Li, M. Mullins, H. Wang, J. Li, R. Krishnamoorti, S. Guo, H.-J. Sue, Scratch behavior of epoxy coating containing self-assembled zirconium phosphate smectic layers, Polymer 112 (2017) 252-263.

APPENDIX C

SUPPLEMENTARY MATERIAL FOR SECTION 5

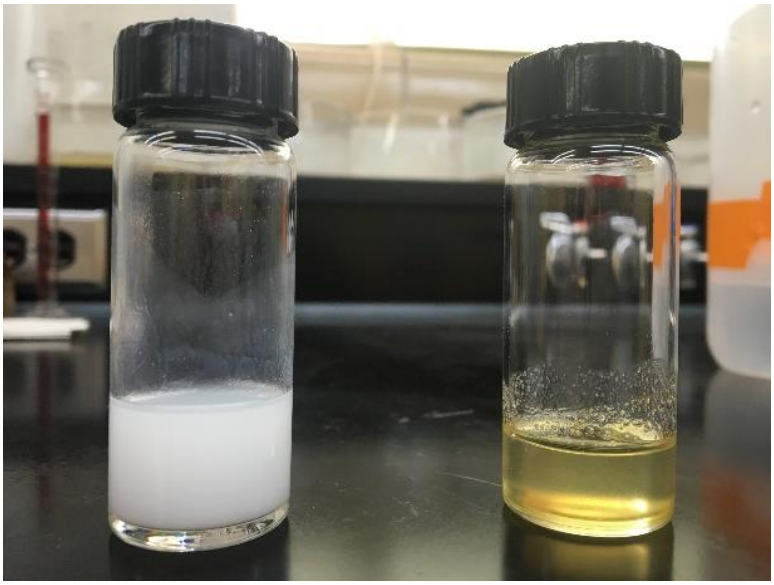

Figure C-1. Photographs of mixture of ZIF-8 and epoxy resins before (left) and after (right) curing at 100 °C for 1 h.

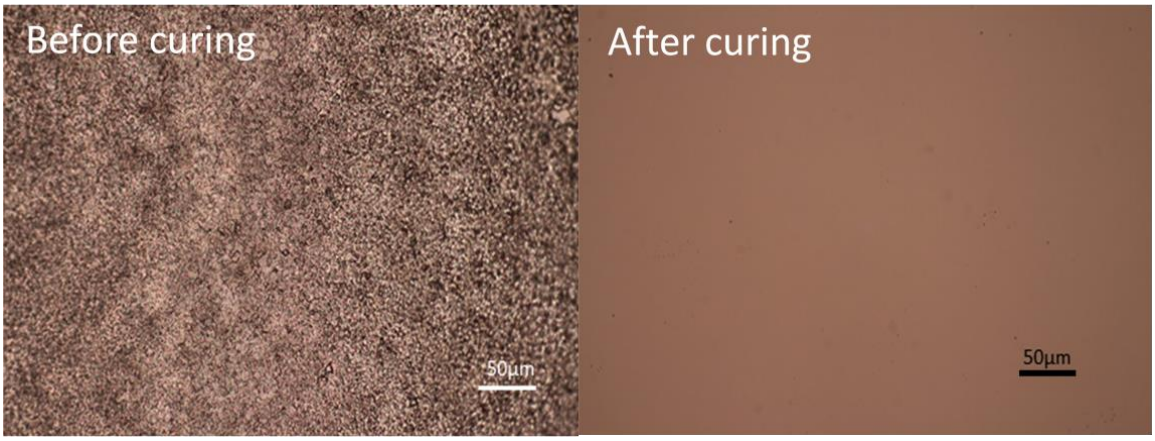

Figure C-2. OM images of mixture of ZIF-8 and epoxy resins before (left) and after (right) pre-cure at 100 °C for 1 h.

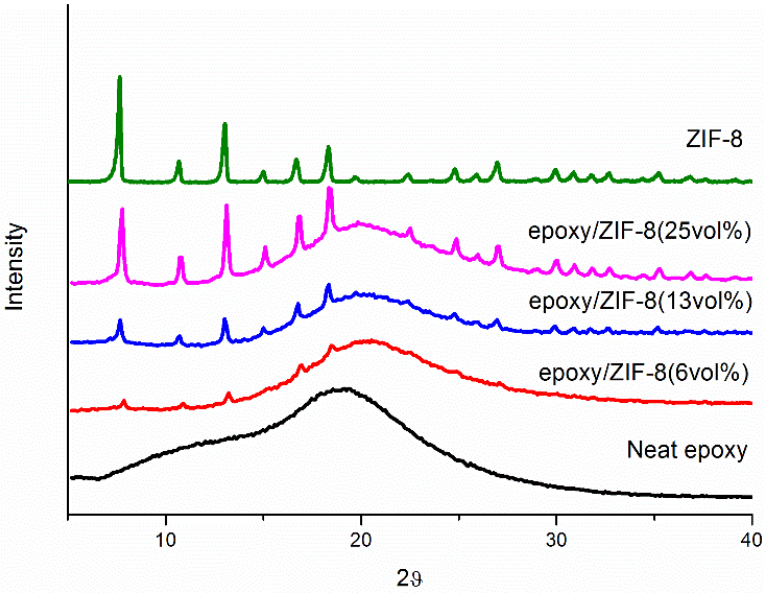

Figure C-3. XRD patterns of epoxy/ZIF-8 nanocomposites.

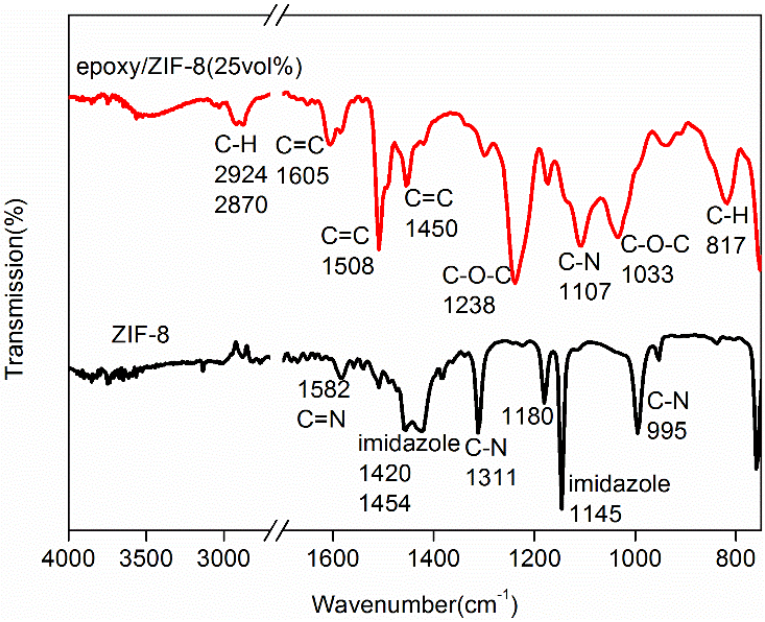

Figure C-4. FTIR curves of epoxy/ZIF-8 nanocomposites.

FTIR analysis of ZIF-8:

Peak at 1582 cm^{-1} could be assigned as C=N stretching vibration. Peaks located at 1420-1454 cm^{-1} are related to the stretching of imidazole ring. Peaks at 1145 and 1180 cm^{-1} are associated with the in-plane bending of imidazole. Peaks at 1311 cm^{-1} represents C-N stretching vibration in imidazole ring.

FTIR analysis of Epoxy/ZIF-8 (25vol %) nanocomposite:

The peaks at 2924 and 2870 cm^{-1} are assigned to the bending vibration of C-H in methylene group. The peaks at 1605, 1508 and 1450 cm^{-1} are the characteristic absorption of the C=C bond in benzene ring. The peaks at 1238 and 1033 cm^{-1} correspond to ether bond (C-O-C) stretching vibration. The peak at 817 cm^{-1} is C–H bending vibration of the phenyl ring. The intensity of the peak at 1311 cm^{-1} was weakened as N on the imidazole reacted with epoxy group and formed new C-N bond at 1107 cm^{-1}.

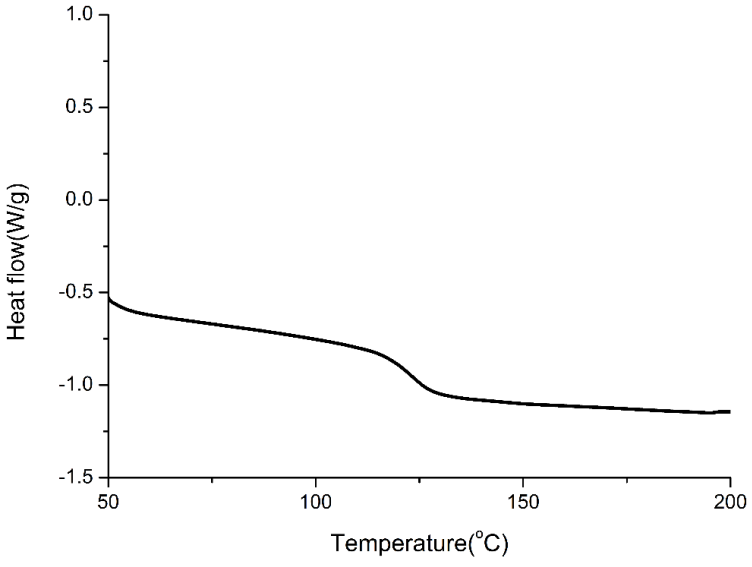

Figure C-5. Non-isothermal (10 °C/min) DSC scans of epoxy/ZIF-8 (13 vol%) nanocomposite.

Density Measurements

Table C-1. The density of the pure epoxy and nanocomposites.

Sample	Density(g/cm^3)	Volume fraction
Neat epoxy	1.31	0
5 wt% ZIF-8 epoxy	1.29	0.064
10 wt% ZIF-8 epoxy	1.27	0.126
20 wt% ZIF-8 epoxy	1.22	0.245

The density of the pure epoxy and nanocomposites is measured following the American Society for Testing and Materials (ASTM, 2008, standard D 792-08) standard. The physical density of ZIF-8 from literature report is about $0.98 g/cm^3$ through theoretical calculation.[1] With this data, theoretical density of nanocomposites are calculated and shown in Figure C-6. It is found that the experimental data is in a harmonious agreement with those given by theoretical calculation. The volume fraction of epoxy/ZIF-8 nanocomposites is calculated based on the measured density.

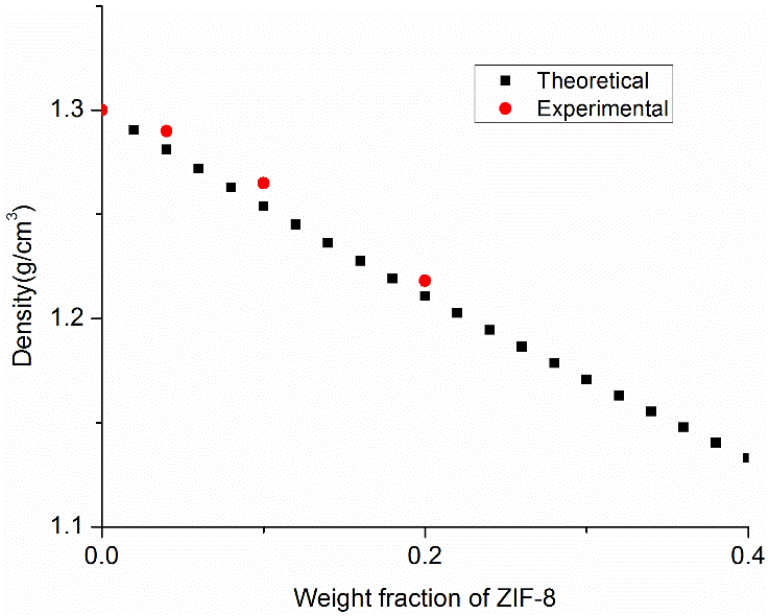

Figure C-6. Theoretical and experimental density as the function of weight fraction.

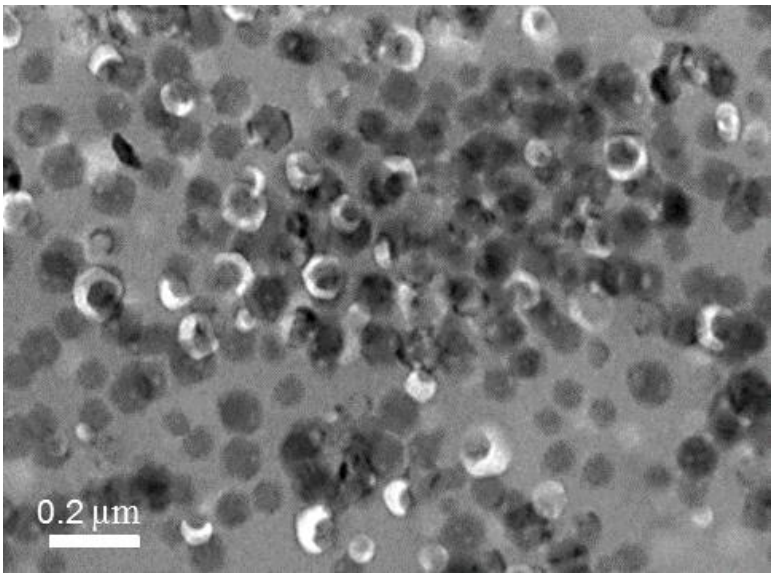

Figure C-7. TEM image of epoxy/ ZIF-8 (36 vol%) in cross-section.

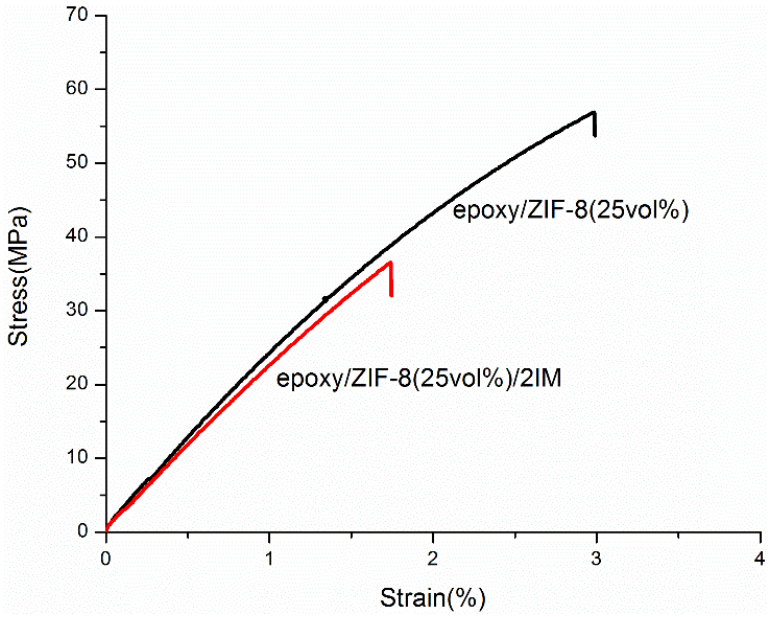

Figure C-8. Tensile engineering stress–strain curves obtained at 25 °C for epoxy/ZIF-8 (25 vol %) and epoxy/ZIF-8 (25 vol %) /2IM nanocomposite thin films.

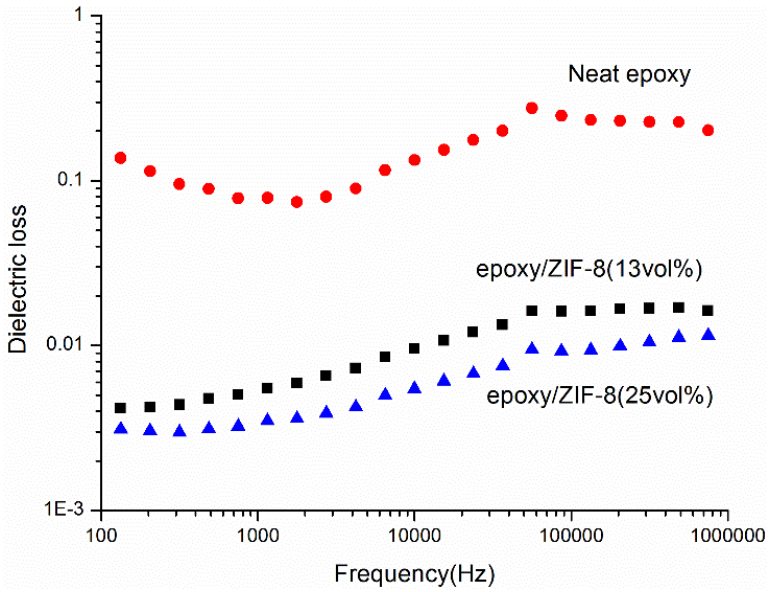

Figure C-9. Dielectric loss of neat epoxy and epoxy/ZIF-8 nanocomposites as the function of frequency.

Table C-2. The first (T_{d1}) and second (T_{d2}) onset decomposition temperature and the 5% weight loss temperature (T5%) of neat epoxy and nanocomposites.

Films	**T_{d1}(°C)**	**T_{d2}(°C)**	**$T_{5\%}$(°C)**
Neat epoxy	282	446	342
epoxy/ ZIF-8(13 vol%)	287	449	350
epoxy/ ZIF-8(25 vol%)	290	449	361

T_{d1} and T_{d2} indicate the onset degradation temperature of first and second stages, respectively. $T_{5\%}$ represents the temperature of degradation at which the weight loss is 5%.

Table C-3. Tensile strength, elongation at break and tensile modulus of epoxy and nanocomposites.

Films	**Tensile Modulus (GPa)**	**Tensile strength (MPa)**	**Maximum elongation (%)**
Neat epoxy	2.33 (±0.10)	58.3(±4.4)	4.91(±0.14)
epoxy/ZIF-8 (13 vol%)	2.70(±0.13)	57.1(±5.5)	3.23(±0.15)
epoxy/ZIF-8 (25 vol%)	2.82(±0.18)	57.8(±5.8)	2.97(±0.39)

[1]. Tan, J. C.; Bennett, T. D.; Cheetham, A. K., Chemical structure, network topology, and porosity effects on the mechanical properties of Zeolitic Imidazolate Frameworks. *Proc. Natl. Acad. Sci. U. S. A.* **2010,** 107, (22), 9938-9943.

APPENDIX D

SUPPLEMENTARY MATERIAL FOR SECTION 6

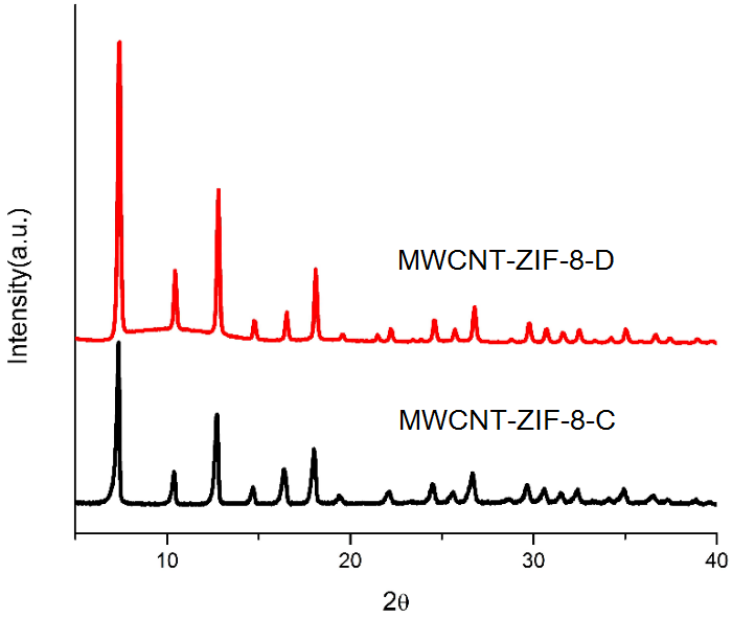

Figure D-1. XRD patterns of MWCNT-ZIF-8-D and MWCNT-ZIF-8-C.

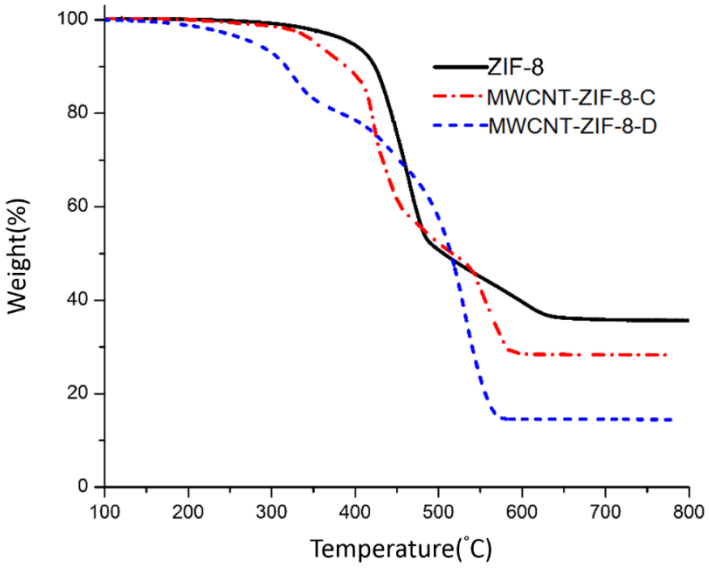

Figure D-2. TGA curves of ZIF-8, MWCNT-ZIF-8-D and MWCNT-ZIF-8-C.

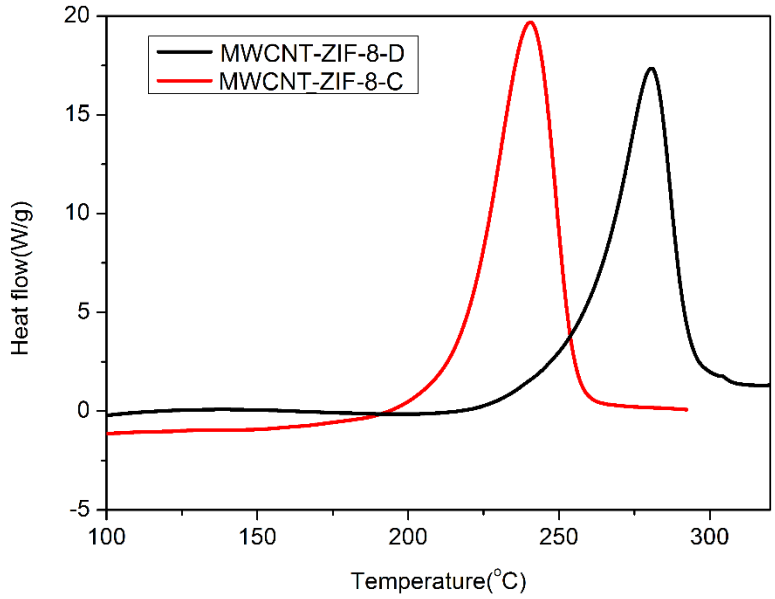

Figure D-3. DSC curves for the mixture of epoxy and MWCNT-ZIF-8-D, and mixture of epoxy and MWCNT-ZIF-8-C.

Electrical conductivity Measurements

The four-point-probe conductivity measurements were performed on free-standing films of MWCNT and MWCNT-ZIF-8 prepared by vacuum filtration. The electrical conductivity values of MWCNT and MWCNT-ZIF-8 are listed in the table below.

Table D-1. Electrical conductivity of MWCNT and MWCNT-ZIF-8.

Samples	Electrical Conductivity (S/m)
MWCNT	958
MWCNT-ZIF-8-D	20
MWCNT-ZIF-8-C	0.0001

CTE Measurements

CTE can be calculated as:

$$\alpha = \frac{(L - L_0)}{L_0 * (T - T_0)}$$

Where L is the length of the film at temperature *T*, L_0 is the initial film length, and T_0 is the initial temperature. CTE was calculated from the slope of linear segment (40–80 °C) of each curve. Figure D-4 shows the film length change (ΔL which is $L - L_0$) rate as a function of temperature for neat epoxy, epoxy/MWCNT and epoxy/MWCNT-ZIF-8 nanocomposites, respectively.

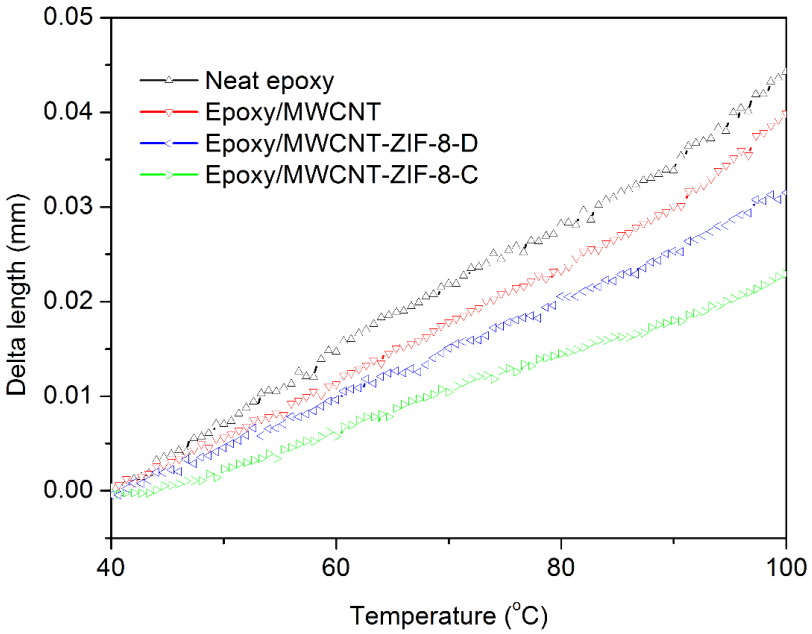

Figure D-4. Film deformation as a function of temperature for neat epoxy, epoxy/MWCNT and epoxy/MWCNT-ZIF-8 nanocomposites.